Developing Modeling, Optimization, and Advanced Process Control Frameworks for Improving the Performance of Transient Energy–Intensive Applications

Seyed Mostafa Safdarnejad

A dissertation submitted to the faculty of
Brigham Young University
in partial fulfillment of the requirements for the degree of

Doctor of Philosophy

John D. Hedengren, Chair
Larry L. Baxter
Thomas H. Fletcher
Matthew J. Memmott
Thomas A. Knotts

Department of Chemical Engineering

Brigham Young University

May 2016

ABSTRACT

Developing Modeling, Optimization, and Advanced Process Control Frameworks for Improving the Performance of Transient Energy–Intensive Applications

Seyed Mostafa Safdarnejad
Department of Chemical Engineering, BYU
Doctor of Philosophy

The increasing trend of world-wide energy consumption emphasizes the importance of ongoing optimization of new and existing technologies. In this dissertation, two energy–intensive systems are simulated and optimized. Advanced estimation, optimization, and control techniques such as a moving horizon estimator and a model predictive controller are developed to enhance the profitability, product quality, and reliability of the systems. An enabling development is presented for the solution of complex dynamic optimization problems. The strategy involves an initialization approach to large–scale system models that both enhance the computational performance as well as the ability of the solver to converge to an optimal solution. One particular application of this approach is the modeling and optimization of a batch distillation column. For estimation of unknown parameters, an ℓ_1-norm method is utilized that is less sensitive to outliers than a squared error objective. The results obtained from the simple model match the experimental data and model prediction for a more rigorous model. A nonlinear statistical analysis and a sensitivity analysis are also implemented to verify the reliability of the estimated parameters. The reduced–order model developed for the batch distillation column is computationally fast and reasonably accurate and is applicable for real time control and online optimization purposes. Similar to estimation, an ℓ_1-norm objective function is applied for optimization of the column operation. Application of an ℓ_1-norm permits explicit prioritization of the multi–objective problems and adds only linear terms to the problem. Dynamic optimization of the column results in a 14% increase in the methanol product obtained from the column with 99% purity. In a second application of the methodology, the results obtained from optimization of the hybrid system of a cryogenic carbon capture (CCC) and power generation units are presented. Cryogenic carbon capture is a novel technology for CO_2 removal from power generation units and has superior features such as low energy consumption, large–scale energy storage, and fast response to fluctuations in electricity demand. Grid–level energy storage of the CCC process enables 100% utilization of renewable power sources while 99% of the CO_2 produced from fossil–fueled power plants is captured. In addition, energy demand of the CCC process is effectively managed by deploying the energy storage capability of this process. By exploiting time–of–day pricing, the profit obtained from dynamic optimization of this hybrid energy system offsets a significant fraction of the cost of construction of the cryogenic carbon capture plant.

Keywords: dynamic optimization, initialization, batch distillation column, cryogenic carbon capture, power generation, energy storage

ACKNOWLEDGMENTS

I would like to express appreciation for the financial support and technical cooperation from Sustainable Energy Solutions (SES), without which this work could not have been undertaken. I am also grateful of the on–demand support, responsiveness, and insightful comments from my PhD advisor, Prof. John Hedengren. I also appreciate the involvement of Prof. Larry Baxter for invaluable direction and advice. I also wish to thank the other members of my committee, Prof. Fletcher, Prof. Knotts, and Prof. Memmot for their comments and guidance. Jonathan Gallacher, James Richards, Jeffrey Griffiths, Colin Muir, and many others at Brigham Young University contributed to this work and I am thankful for their hard work and dedication to the research.

I am also very grateful for the continuous encouragement of my parents and siblings. Lastly, I wish to recognize my wife, Shima, for her enabling support, encouragement, and company throughout my graduate school. I would like to dedicate this dissertation to Shima, who deserves this degree as much as I do.

CONTENTS

LIST OF TABLES

LIST OF FIGURES

NOMENCLATURE

C	Mass flow rate of the coal combustion
CCC	Cryogenic carbon capture
$CCCECL$	Cryogenic carbon capture with an external cooling loop
CCS	Carbon capture and storage
CHP	Combined heat and power unit
D	Distillate mole flow rate
D^{CCC}	Total electricity demand for the CCC facility
D^{LNG}	Total electricity demand of the LNG production facility
D^{MR}	Work of compression of the mixed refrigerant compressor
D^{NG}	Work of compression of the natural gas compressor
D^{NG}	Work of compression of the pipeline compressor
D^{plant}	Combined electricity demand of the CCC and LNG production facilities
$D^{plant,max}$	Maximum fraction of the combined electricity demand of the LNG and CCC plants
D^{Res}	Electricity demand of the residential users
D^{Tot}	Total electricity demand
E_{MV}	Murphree efficiency
EGS	Enhanced geothermal system
EPA	Environmental Protection Agency
f_{cond}	Fraction of the initial reboiler charge in the condenser
f_{tray}	Fraction of the initial reboiler charge on each tray
FG^{C}	Mass flow rate of the flue gas produced from coal combustion
FG^{NG}	Mass flow rate of the flue gas produced from natural gas combustion
$FG^{NG,max}$	Maximum mass flow rate of the flue gas produced from natural gas combustion
FOM^{CT}	Fixed operating and maintenance costs of the coal–fired power generation unit
FOM^{GT}	Fixed operating and maintenance costs of the gas–fired power generation unit
GP^{CC}_{max}	Maximum permitted power production in the combined cycle
GT^{cap}	Capacity of the gas turbine
h_{dot}	Heat input from the reboiler
h_f	Heating efficiency
h_L	Liquid Enthalpy
h_V	Vapor Enthalpy
H_{vap}	Heat of vaporization for the mixture
HHV	Higher heating value
IEA	International Energy Agency
$IGCC$	Integrated Gasification Combined Cycle
K^{NG}	Gain for the natural gas intake
K^{ST}	Gain for power production in the steam boiler
L	Liquid mole flow rate
$LCOE$	Levelized Cost of Electricity
LNG	Liquefied natural gas
LNG^{BYP}	Mass flow rate of the LNG bypassing the tank
$LNG^{From\ Tank}$	Mass flow rate of the LNG from the tank
LNG^{Prod}	Mass flow rate of the LNG production

LNG^{Tank}	Mass of the LNG in the tank
$LNG^{To\ Tank}$	Mass flow rate of the LNG directed to the tank
LNG^{R}	Total mass flow rate of the LNG demand
MR	Mass flow rate of the mixed refrigerant
n	Number of trays
N_{cond}	Number of moles in the condenser
n_p	Number of product moles
N_{reb}	Number of moles in the reboiler
$N_{reb,init}$	Initial number of moles in the reboiler
N_{tray}	Number of liquid moles on each tray
NG	Natural gas
NG^{CCC}	Mass flow rate of the natural gas coming from the natural gas compressor
NG^{Conv}	Mass flow rate of the natural gas combustion in the gas turbine
$NG^{Conv,max}$	Maximum mass flow rate of the combusted natural gas
NG^{EXPT}	Mass flow rate of the natural gas exported to the pipeline
$NG^{Onephase}$	Mass flow rate of the natural gas coming from the LNG/mixed refrigerant recuperator
NG^{PL}	Mass flow rate of the natural gas imported from the pipeline
$NG^{PL,SP}$	Set point of the natural gas imported from the pipeline
NG^{Tot}	Total mass flow rate of the natural gas for liquefaction
$NG^{Twophase}$	Mass flow rate of the two phase natural gas coming from the CCC plant
$NGCC$	Natural gas combined cycle
OCR	Organic Rankine cycle
P	Pressure
P^{C}	Coal price
P^{CT}	Power generated from the coal–generated flue gas
P^{E}	Energy price
P^{Ex}	Excess power production
P^{GT}	Power production in the gas turbine
P^{N}	Natural gas price
P^{NGCC}	Power generated from the natural gas flue gas
P^{SP}	Set point of the power output in the steam boiler
$P^{SP,Max}$	Upper bound for the set point of the power output from the coal-fired steam boiler
P^{ST}	Total power production in the steam boiler
P^{Tot}	Total power generation
P^{W}	Power generated from the wind
P_i^{sat}	Saturated pressure of tray i
PC	Pulverized Coal
Q^{g}	Total heat gain in the recuperator
Q^{l}	Total heat loss in the recuperator
Q_{cond}	Condenser cooling load
Q_{reb}	Reboiler heating rate
R	Reflux ratio
$SAPG$	Solar Aided Power Generation
t	Time

T_i	Temperature of tray i
V	Vapor mole flow rate
VOM^{CT}	Variable operating and maintenance costs of the coal–fired power generation unit
VOM^{GT}	Variable operating and maintenance costs of the gas–fired power generation unit
x_{cond}	Composition in the condenser
x_p	Product composition
x_{reb}	Composition in the reboiler
x_n	Liquid mole fraction
y_n	Actual mole fraction
y_n^*	Equilibrium vapor mole fraction
δP	Pressure drop
ΔH^1	Enthalpy difference of the cold natural gas across the recuperator
ΔH^2	Enthalpy difference of the cold mixed refrigerant across the recuperator
ΔH^3	Enthalpy difference of the warm natural gas across the recuperator
ΔH^4	Enthalpy difference of the warm mixed refrigerant across the recuperator
ΔH_{FG}^C	Specific enthalpy change of the flue gas from combustion of coal
ΔH_g	Enthalpy of combustion of natural gas
ΔH_{FG}^{NG}	Specific enthalpy change of the flue gas from combustion of natural gas
ε_g	Efficiency of power production in the gas turbine
ε^{SB}	Efficiency of the heat exchange in steam reboiler
η^{ST}	Efficiency of the steam turbine
γ_i	Activity coefficient
τ^{NG}	Time constant for the natural gas intake
τ^{ST}	Time constant for power production in the steam boiler

CHAPTER 1. INTRODUCTION

The economic and environmental desires to reduce industrial energy consumption drives ongoing optimization of the new and existing technologies important in engineering. For example, large-scale continuous distillation columns have been the focus of optimization since the first column was built. However, the transient nature of batch columns has caused many to remain unoptimized which results in more energy consumption than is likely needed and an opportunity for improvement. This emphasizes the continuous need for optimization of the existing units including continuous and batch distillation columns. Another important area that would benefit from optimization is energy generation. While new technologies for power production, such as fuel cells, and new energy sources such as renewable energy, show promise, they cannot yet replace a grid–scale thermal power unit. Therefore, fossil–fueled power plants will continue to play a major role in power sector. Optimizing the operation of fossil–fueled power plants typically means increasing the efficiency of the system which also results in lower CO_2 emission. Although efficiency improvement reduces the CO_2 emission from these power plants, it is not adequate to achieve the target CO_2 emission level of the Clean Power Plan enforced by the environmental protection agency (EPA). Thus, optimization of the existing units should accompany the technology development in finding ways to reduce CO_2 emission from fossil power plants.

Developing modeling frameworks for estimation, optimization, and control of these two key industrial applications (batch distillation and power plant carbon reduction) is a focus of this dissertation. These two application areas are complex and require large–scale differential and algebraic equation models to describe their dynamic behavior. A fundamental contribution of this work is to not only optimize these two particular applications, but also to develop methods to initialize and efficiently solve large–scale and complex system models. Developing initialization strategies for large–scale nonlinear systems is described in Chapter 2. In Chapter 3, a mathematical modeling framework is developed for a batch distillation column. In this case, the purpose is to de-

velop a simple model that takes advantage of a moving horizon estimator for parameter estimation and a model predictive controller for maximization of the column product while staying within the product quality limits. Chapters 4-6 develop a mathematical model for the integrated system of a cryogenic carbon capture and power generation units. This work includes power production from fossil-fueled and renewable power plants with consideration of the energy–storing version of cryogenic carbon capture. The goal of this application is to maximize the profitability of the hybrid system such that it can meet the overall electricity demand and capture 90% of the CO_2 emissions from the fossil-fueled power plants. A model predictive control framework is utilized in this application to optimize the operation of the hybrid system.

While this study considers two specific applications in the energy industry, they are presented in a modular basis. The estimation and control frameworks developed in this dissertation are applicable to similar systems of batch distillation or energy production, but are also applicable more generally to optimize complex dynamic systems.

1.1 Initialization Strategies and Objective Functions for Estimation and Optimization of Dynamic Systems

The large-scale dynamic applications considered in this study are non-convex and nonlinear, i.e. there are local optimal points and the solution cannot be found from a single matrix inversion. Consequently, the solver may not be able to find a successful solution. In addition, many variables and equations define these systems and their time–dependence. Thus, a good initialization strategy is necessary to find a successful solution with a reasonable computational time. Several techniques have been utilized to initialize these nonlinear systems. These techniques include initialization from a steady–state or a linear solution of the problem, structural decomposition of the differential and algebraic equations (DAEs), and initialization from the sequential and simultaneous simulation of the problem. Developing initialization strategies for these nonlinear systems is the foundation of further analysis of the two industrial applications considered in this dissertation. Chapter 2 details these initialization strategies.

In two applications, new techniques for estimation, optimization, and control are used to develop the modeling frameworks. These techniques include moving horizon estimation (MHE) and model predictive control (MPC) that benefit from an objective function in the form of an ℓ_1-

-norm. An ℓ_1- norm objective function has superior performance to the conventional least square techniques. The details of an ℓ_1- norm objective function for estimation and optimization purposes are discussed in details in Chapter 2.

1.2 Batch Distillation Columns

Many specialty and smaller-use items are often processed in batch distillation columns. The transient nature of batch columns has caused many to remain unoptimized. Work on batch columns has increased in the last 30 years as computers have become more sophisticated, and several studies have considered both advanced solving techniques and advanced column configurations. The models developed for batch column optimization generally fall into two categories: first-principles models and shortcut or simple models. First-principles models are those with governing mass and energy balance equations, detailed thermodynamics, tray dynamics, system non-idealities and variable flow rates. While these models are more accurate, the use of these models has been limited due to high computational costs. The second class of models, shortcut models, has received far greater attention. These models contain less physics and are generally used for estimates and comparative studies. The primary purpose of these models is to create an accurate, computationally fast simulation for use in design and control of batch columns. While these models achieve the reduction in computational load, the lack of experimental data makes it difficult to determine the accuracy of these models. The assumptions made in these models also limit their use to ideal systems.

The gap between first-principles models and shortcut models is large. First-principles models can provide predictions for many systems but require thermodynamic and physical property models as inputs, while the assumptions in shortcut models make them applicable only to a small class of relatively ideal systems. In this dissertation, a method is proposed for developing shortcut models with relaxed assumptions. The method is based on fitting parameters in place of simplifying assumptions to include system non-idealities without solving the first-principles equations. Empirical model regression requires extensive experimental data whereas first-principles models typically need less data to determine unknown parameters, being based on fundamental correlations. Dynamic parameter estimation can be used to reduce the experimental load. The case study presented in this dissertation required only one experiment to determine model parameters. As

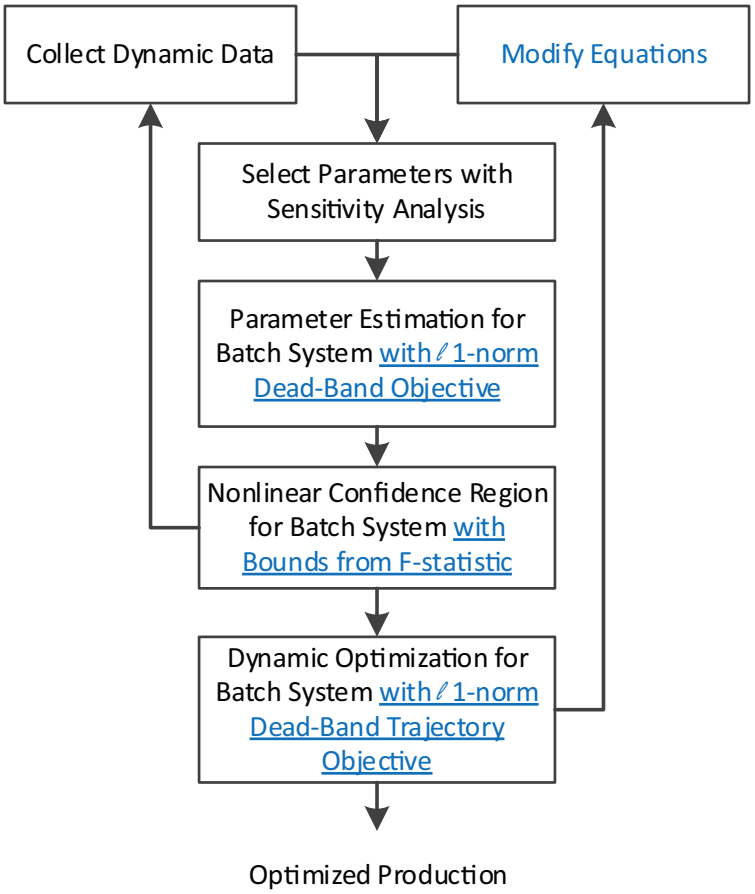

Figure 1.1: Overview of methodology for batch column optimization with novel contributions underlined

with any model containing fitting parameters, there is concern over the accuracy of the parameters. By using nonlinear statistics and a model sensitivity analysis, it is possible to determine how many parameters can be estimated from the collected data and the acceptable range for those parameters. These steps are shown in Figure 1.1 and form the heart of the method. Underlined elements of the methodology indicate the new approach to batch separation systems.

The well-known methodology shown in Figure 1.1 is applied to an experimental case study. The methodology includes the use of ℓ_1-norm dynamic parameter estimation, nonlinear statistics, and a model parameter sensitivity analysis. These techniques are applied together to a batch distillation column in a holistic approach to dynamic optimization. Models developed using this method account for system non-idealities not seen in typical shortcut models without sacrificing computational speed. The fast solution time of the models developed in this study allows for their

utilization in real–time control and online optimization applications. The novel contributions of this study are:

- Development of a reduced–order model that is suitable for real–time control
- Application of an ℓ_1-norm objective function for estimation and optimization
- Nonlinear statistical analysis with approximate multivariate confidence regions
- Model validation for both estimation and optimization

1.3 Hybrid System of Power Generation and Cryogenic Carbon Capture

The second application considers a hybrid system of power generation units and cryogenic carbon capture^{TM} (CCC). The key to achieve target levels of CO_2 emissions in the power sector is to integrate fossil-fueled power generation plants with a carbon capture system. Although various methods have been developed for CO_2 capture, a major drawback of most CO_2 removal systems is the parasitic energy load. Cryogenic carbon capture^{TM} is a novel technology for CO_2 separation from power plant flue gas and is less energy intensive compared to the conventional capture systems. The CCC process cools flue gas from power generation units to the point that CO_2 desublimates. The process then separates solid CO_2 from the remaining gas and melts it. Both the remaining flue gas and pressurized solid CO_2 warm back to higher temperatures.

The CCC process captures CO_2 in the flue gas through desublimation. The CCC process requires two refrigeration loops that consume most of the energy. The CCC process, however, has some configurations that store energy in the form of a refrigerant. In the energy–storing version, CCC generates refrigerant during non–peak hours and stores it in insulated vessels for peak hour usage, thereby replacing the compressor energy with the stored refrigerant. This causes the refrigerant production rate to decrease during peak hours, which decreases the energy demand required by the CCC process for as long as the stored refrigerant is available. With the decreased demand, more power is available during peak hours relative to the baseline coal boiler rated capacity. In this dissertation, storage of only one of the refrigerants is considered as it provides more energy during the recovery mode. Although other refrigerants could be selected, the refrigerant considered for this purpose is LNG. In addition, during the energy recovery mode of the CCC, a gas turbine can

provide more power through the combustion of a fraction of the LNG after it goes through the CCC process and is converted to natural gas.

Additionally, the LNG generation and storage cycle primarily involves compressors and heat exchangers; therefore, the storage/recovery or load changing response time is fast (seconds) compared to that of the steam boilers (hours). The faster energy storage response time is well matched to intermittent sources like wind turbines and enables the conventional power generation systems to follow rapidly changing loads. This results in an easier integration of thermal power generation systems with renewable intermittent power supplies. As renewable energy sources become a larger portion of the energy market, the significance of rapidly responding to large fluctuations with energy storage becomes critical to maintaining a reliable and cost–effective electric grid. Storage capacity of LNG vessels also allows scaling from the proposed energy storage to large–scale systems.

Sustainable Energy Solutions developed the CCC process and energy–storing capabilities and the detailed models that determine system energy demand and response time. The novel contributions of this study include developing grid–level models and optimizing CCC in the context of grid performance. Some of the novel contributions of this work are:

- Dynamic integration of the CCC process with baseline and load–following power generation units
- Application of the grid–level energy storage facilities for load management
- Full utilization of wind power and optimizing the contribution to the grid
- Enhanced operational flexibility of the integrated energy system
- Reduction in cycling costs of power generation units by using energy storage
- Quantification of impact of energy storage in meeting the demand in combined and simple cycles power generation units

1.4 Outline

This dissertation is divided into 5 chapters. Chapter 2 describes the initialization strategies developed to achieve a successful solution and to decrease the simulation time for estimation and control of dynamic applications. These initialization strategies are first demonstrated on simple problems and they build the foundation for more complex systems such as the applications used in this dissertation. In addition, the standard frameworks for modeling, estimation, and control of the applications used in this dissertation are discussed in Chapter 2. These frameworks benefit from an ℓ_1-norm objective function in which has a superior performance over the conventional least square techniques.

Chapter 3 describes a systematic approach to develop a simple model for optimization of a batch distillation column. The details of the simple model developed for a batch distillation column and the experimental procedures taken to verify the model are discussed in this chapter. The results from the simple model are also compared to a more rigorous model. A nonlinear statistics analysis, a parameter ranking, and a sensitivity analysis are also described in verifying the accuracy of the model. The last section of this chapter describes the optimization of the column with the simplified model and the validation of the optimization results.

Chapter 4 investigates the dynamic integration of cryogenic carbon capture with power generation units. This chapter includes a mathematical model developed for the non-energy-storing version of the hybrid system. First, application of the model in summer and winter conditions is discussed. Then, the impact of increasing the contribution of wind power in meeting the electricity demand on profitability of a hybrid system without energy storage is reported. A key result is that there is a maximum wind energy adoption fraction beyond which the intermittent power source is not fully utilized.

Chapter 5 considers the performance of a hybrid system of power generation units and an energy storing version of cryogenic carbon capture. The model developed in Chapter 4 is modified in this chapter to account for energy storage and export of natural gas to a pipeline. The coal–fired power generation unit considered in this chapter is able to load follow without excess energy production.

Chapter 6 considers the performance of a hybrid system of a CCC process and power generation unit in which the coal–fired plant operates as a baseline unit. In addition, the impact of

energy storage on reduction of the cycling cost of a power plant in following the electricity load is presented in this chapter. This chapter continues with a comparison between a typical power plant that has a CO_2 capture process, a simple cycle peaking unit, and a combined cycle unit.

Chapter 7 presents the main highlights of this dissertation followed by a discussion for future research directions.

1.5 Main Contributions

The main contributions of this dissertation are summarized as following:

- Initialization strategies for optimization of dynamic systems, Chapter 2.
- Reduced–order models and validation of dynamic parameter estimation and optimization for batch distillation, Chapter 3.
- Modeling hybrid systems of cryogenic carbon capture and baseline power generators and investigating the impact of cryogenic carbon capture on the performance of power plants, Chapter 4.
- Grid–level dynamic optimization of cryogenic carbon capture with energy storage, load–following conventional, and renewable power sources, Chapter 5.
- Hybrid system of cryogenic carbon capture and baseline power generators including both peaking and combined cycle units, Chapter 6.

CHAPTER 2. INITIALIZATION STRATEGIES FOR OPTIMIZATION OF DYNAMIC SYSTEMS

2.1 Introduction

Differential and algebraic equations (DAEs) are natural expressions of many physical systems found in business, mathematics, systems biology, engineering, and science. In business, the supply chain can be optimized by modeling the storage, production, and consumption throughout a network [1]. In mathematics, ordinary (ODEs) or partial differential equations (PDEs) are used to describe certain classes of boundary value problems. In engineering, these equations result from material, energy, momentum, and force balances [2]. In science, laws of motion are naturally described by differential equations that relate position, velocity, and acceleration [3, 4].

Just as differential equations naturally describe many systems, these same equations can also be used to optimize among many potential designs or feasible solutions. One difference between static or steady-state models and dynamic models is that optimal solutions must not only observe constraints at one time point, but also along a future time window. Part of what makes a dynamic solution challenging is that design variables at one time instant affect both current and future objective values and constraints in the time horizon. This is generally challenging from an optimization standpoint because of many degrees of freedom that are adjustable at each time step, strong nonlinear relationships, and a wide range of sensitivities between the adjustable parameters and multiple objectives.

2.1.1 Simulation and Optimization of DAE Systems

There are many solution approaches for sets of ODEs or DAEs and a review of all possible methods is beyond the scope of this work. Dynamic systems can be solved as ODEs or DAEs through the simultaneous approach [5–11] to dynamic optimization as opposed to a semi-sequential [12] or sequential approach [13–17]. The sequential method is where the model equa-

tions and objective function are calculated in successive evaluations. In a sequential approach, the DAEs are solved independently of the objective function. Each evaluation of the objective function involves fixing the independent variables at current iteration values and solving the dynamic equations forward in time with a shooting approach. It is referred to as a shooting method because trial solutions are propagated forward in time and the resulting dynamic trajectory is used to calculate the objective function. Successive evaluations of the objective function are used to compute gradients of the objective with respect to the decision variables and drive towards an optimal solution. Terminating the optimization progress before convergence typically produces a feasible yet sub-optimal result. Sequential or shooting methods use forward integrating solvers for differential equations with variable time steps to maintain the integration accuracy. A number of solvers or modeling platforms exist for solving ODE or DAE problems with either sequential or simultaneous methods [18, 19] such as DASSL [20], SUNDIALS [21], and many others [22–27].

Dynamic models can be translated into sets of algebraic constraints that can be solved with standard gradient-based optimization techniques. The differential terms can be translated into algebraic equations through orthogonal collocation on finite elements. Orthogonal collocation on finite elements allows a simultaneous solution where objective function and equations are solved together instead of sequentially. Orthogonal collocation is simply a technique that relates differential terms to state values in a discretized time horizon. This translation of DAEs into a set of algebraic equations also allows capable Linear Programming (LP), Quadratic Programming (QP), Nonlinear Programming (NLP), or Mixed-Integer Nonlinear Programming (MINLP) solvers to optimize these dynamic systems with a simultaneous approach instead of shooting methods that rely on forward integrating simulators. Similar approaches are used for ODEs, DAEs, PDEs, and Partial DAEs. Large-scale problems such as PDEs or PDAEs with few decision variables may be best suited for analysis by a sequential or shooting method. Small or medium scale problems with many decision variables or unstable systems are best suited for analysis with the simultaneous approach [28]. Dynamic problems can include continuous or discrete variables that can be solved with MINLP solvers, have multiple competing objectives, and require robust or stochastic optimization methods to deal with uncertainty. Unlike sequential approaches, terminating the optimization progress does not give a feasible sub-optimal result. It is only at final convergence that the equations are satisfied with the objective function at an optimal value. The solvers and modeling

platform used in this study are embedded in the APMonitor Modeling Language and Optimization Suite [29].

2.1.2 Standard DAE Form

Dynamic modeling of physical systems involves several phases starting with the selection of a model form. Dynamic model forms may be empirical where the form of the model is determined from data, fundamental where the model parameters and equations are derived from first principles, or hybrid with a mix of empirical and fundamental relationships. One advantage of using empirical models is that only inputs and outputs must be collected for the model development and less information about the process is required to develop a model. Fundamental models are often difficult to develop because particular relationships can either be unknown or impossible to isolate. In each case, the differential equations relate certain process inputs (u) to differential states (x) or algebraic states (y).

The method taken in this work is to solve hybrid dynamic process models in open-equation form with either differential or algebraic equations while minimizing an objective function. Differential equations are simply those that contain at least one differential term and algebraic equations are those that do not. While different objective functions can be used in Equation 2.1a, an ℓ_1-norm formulation is adopted in this dissertation and is discussed in Section 2.2. Equations may also consist of equality ($=$) or inequality ($<$ or $\leq$) constraints as shown in Equation 2.1:

$$\min_{u} h\left(x, y, u, \theta, d\right) \tag{2.1a}$$

$$0 = f\left(\frac{dx}{dt}, x, y, u, \theta, d\right) \tag{2.1b}$$

$$0 \leq g\left(\frac{dx}{dt}, x, y, u, \theta, d\right) \tag{2.1c}$$

where Equation 2.1b is the set of DAE equality constraints and Equation 2.1c is the set of DAE inequality constraints. For solvers that require only equality constraints and simple inequality bounds on variables, the inequality constraints are converted to an equality constraint with the addition of a slack variable [30]. Equations need not contain differential states, states variables,

inputs, and outputs. However, each equation must contain at least one differential or algebraic state or output variable.

The inputs may consist of parameters (θ) that are either known from fundamental relationships or measured directly. There may also be unknown parameters that can either be inferred from other measurements or unknown parameters that are unobservable given the available measurements. Other types of inputs may be disturbances (d) that affect the system that are either measured or unmeasured. Finally, inputs also include those that can be changed to optimize or control the system (u). These are referred to as design variables or manipulated variables depending on whether it is a design or control application. These parameters, disturbances, or manipulated variables constitute the set of exogenous inputs that change independently of the system dynamics and act on the system to change the dynamic response.

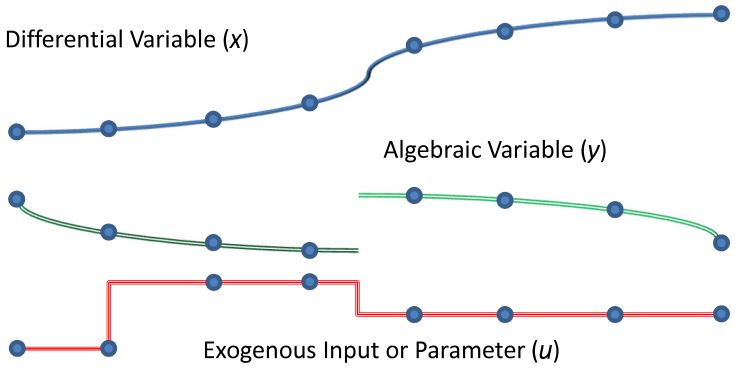

Figure 2.1: DAE model equations are discretized and solved over a time horizon.

Differential states are those variables that are calculated based on differential equations while algebraic states are those variables that do not appear as differential terms. Algebraic states may be either continuous or discontinuous while differential states are typically considered as continuous as shown in Figure 2.1. For dynamic simulation models there must be a unique equality constraint or binding inequality constraint for each model state. If there are more variables than equations $\left(n_{var} \geq n_{eqn}\right)$, the system has degrees of freedom that can be arbitrarily adjusted to best meet one or more objectives. If there are more equations than variables $\left(n_{eqn} \geq n_{var}\right)$, the system

may be over-specified and there is likely no set of variables that can simultaneously satisfy all constraints.

2.1.3 DAE Models with Higher Order Derivatives

Equations that contain higher order derivatives can also be fit into the standard form as shown in Equation 2.1 by creating additional variables for every higher order derivative. For example, acceleration is equal to the second derivative of position as in $a = \frac{d^2x}{dt^2}$. By adding the additional variable of velocity and an additional equation, the second order system becomes a set of two first order differential equations as in $a = \frac{dv}{dt}$ and $v = \frac{dx}{dt}$ where a is acceleration, v is velocity, and x is position. A similar approach can be used for any higher order derivatives. Initialization of higher order derivative models requires an initial condition that is specified for each differential variable.

2.1.4 DAE Models with Integral Terms

Equations that contain integrals can also be fit into the standard form as shown in Equation 2.1 by creating a new differential variable for every integral term. For example, an ideal Proportional Integral Derivative (PID) controller may be included in a process model to simulate the action of an embedded control system as shown in Equation 2.2.

$$u = u_b + P\ (SP - PV) + I \int_0^t (SP - PV)\, dt - D\, \frac{d(PV)}{dt} \tag{2.2}$$

In this case, u is the controller output, u_b is the controller bias, and P, I, and D are the tuning constants. The integral term $\left(\int_0^t (SP - PV)\, dt\right)$ grows with persistent offset between the setpoint (SP) and process variable (PV). This integration term is placed in standard DAE form by differentiating the integral and creating a new variable X_I that accumulates the error. The DAE expression for a PID controller becomes two equations as shown in Equation 2.3.

$$u = u_b + P\ (SP - PV) + I\, X_I - D\, \frac{d(PV)}{dt} \tag{2.3a}$$

$$\frac{dX_I}{dt} = SP - PV \tag{2.3b}$$

The initial condition for the integral term, X_I, is set to zero when the controller is changed from manual to automatic. While the method of modeling integrals is shown for the PID equation as an example, it is generally applicable to other integral expressions as well. One drawback to differentiating any expression is that small numerical errors may accumulate over a time with a well known effect termed "drift off". This effect is also shown Section 2.3.3, in relation to differentiating higher index DAEs.

2.1.5 DAE Models with Discrete Variables

DAE models may contain discrete variables such as binary, integer, or discrete decision variables. When the DAE model is converted into algebraic form, these additional discrete variables require an MINLP solver. Several capable MINLP solvers exist [31–34] to solve this class of problems and may use strategies such as Branch and Bound (successive NLP), Outer Approximation (successive MILP), or a combination of these methods to solve the system of equations. Initialization of this class of DAE models is a relaxation of the discrete variables to form a continuous variable approximation [28].

2.2 Standard Objective Functions for Estimation and Control

The standard modeling frameworks discussed in previous sections are generally applied in dynamic estimation and control in an application for which an objective function is minimized. In the case of estimation, the error between model prediction and the measurements observed over time is minimized by manipulation of the unknown variables or parameters. In the case of optimization and control, the error between the controlled variables and the reference trajectories for them is minimized through the manipulation of decision variables. Different objective functions could be considered for both estimation and control applications. Dynamic estimation and control of the applications used in this dissertation benefit from an objective function in the form of an ℓ_1-norm. The standard formulation of an ℓ_1-norm objective function for estimation and optimization is reviewed in Sections 2.2.1 and 2.2.2, respectively. The equations developed for an ℓ_1-norm objective function are solved together with the equations presenting the system in consideration (with the general form shown in Equation 2.1).

2.2.1 Parameter Estimation

Many approaches can be used to find the parameters, two of which are least squares formulation and ℓ_1-norm formulation for the objective function. According to the Central Limit Theorem, errors resulting from several sources tend to be normally distributed regardless of the distributions of the individual sources. This indicates that under broad conditions, errors usually are normally distributed. However, if there are wild data points (outliers) that originate from other sources, the ℓ_1-norm is less sensitive to them than the least squares approach. Additionally, the form of the objective function used in this ℓ_1-norm formulation is smooth and continuously differentiable as opposed to using the absolute value function. The form of the objective function with ℓ_1-norm formulation is shown in Equation 2.4 [35, 36]. The nomenclature for Equation 2.4 is found in Table 2.1.

$$\Psi = \min_{\theta,x,y} w_x^T (e_U + e_L) + w_p^T (c_U + c_L) + \Delta\theta^T c_{\Delta\theta} \tag{2.4a}$$

$$s.t. \qquad 0 = f(\frac{\delta x}{\delta t}, x, y, \theta, d, u) \tag{2.4b}$$

$$0 = g(x, y, \theta, d, u) \tag{2.4c}$$

$$0 \leq h(x, y, \theta, d, u) \tag{2.4d}$$

$$e_U \geq (y - z + \frac{\delta}{2}) \tag{2.4e}$$

$$e_L \geq (z - y - \frac{\delta}{2}) \tag{2.4f}$$

$$c_U \geq (y - \bar{y}) \tag{2.4g}$$

$$c_L \geq (\bar{y} - y) \tag{2.4h}$$

$$0 \leq e_U, e_L, c_U, c_L \tag{2.4i}$$

Equations (2.4b) to (2.4d) represent the model of the system and the constraints. Equations (2.4e) and (2.4f) also represent the deadband for the measured variable; i,e, if the predicted value for this variable is within a deadband from the measurements, the objective function is not penalized. The expressions presented by Equations (2.4g) and (2.4h) permit the optimizer to pe-

nalize large deviation of the predicted variable from the prior model output. An ℓ_1-norm objective function is discussed in detail in [35, 37].

Table 2.1: Nomenclature for general form of the objective function with ℓ_1-norm formulation for dynamic data reconciliation

Symbol	Description
Ψ	minimized objective function result
y	model outputs $(y_0, \ldots, y_n)^T$
z	measurements $(z_0, \ldots, z_n)^T$
$\bar{y}$	prior model outputs $(\bar{y_0}, \ldots, \bar{y_n})^T$
w_x^T	measurement deviation penalty
w_p^T	penalty from the prior solution
$c_{\Delta\theta}$	penalty from the prior parameter values
δ	dead-band for noise rejection
x, u, θ, d	states (x), inputs (u), parameters (θ), or unmeasured disturbances (d)
$\Delta\theta^T$	change in parameters
f, g, h	equations residuals (f), output function (g), and inequality constraints (h)
e_U, e_L	slack variable above and below the measurement dead-band
c_U, c_L	slack variable above and below a previous model value

2.2.2 Control Optimization and Implementation

Similar to the parameter estimation developed in Section 2.2.1, many approaches could be used in control and optimization of the dynamic systems. The form of the objective function used in this dissertation is related to a nonlinear dynamic optimization with an ℓ_1-norm formulation. In comparison to the common squared error norm, ℓ_1-norm is advantageous as it allows for a dead-band and permits explicit prioritization of control objectives. The form of the objective function with ℓ_1-norm formulation is shown in Equation 2.5 [35, 36]. The nomenclature for Equation 2.5 is found in Table 2.2.

$$\Psi = \min_{u,x,y} w_h^T \; e_h + w_l^T \; e_l + y_m^T \, c_y + u^T \; c_u + \Delta u^T \; c_{\Delta u} \tag{2.5a}$$

$$s.t. \qquad 0 = f(\frac{\delta x}{\delta t}, x, u, d) \tag{2.5b}$$

$$0 = g(y, x, u, d) \tag{2.5c}$$

$$0 \leq h(x, u, d) \tag{2.5d}$$

$$\tau_c \frac{\delta z_{t,h}}{\delta t} + z_{t,h} = SP_h \tag{2.5e}$$

$$\tau_c \frac{\delta z_{t,l}}{\delta t} + z_{t,l} = SP_l \tag{2.5f}$$

$$e_h \geq (y - z_{t,h}) \tag{2.5g}$$

$$e_l \geq (z_{t,l} - y) \tag{2.5h}$$

Equations (2.5b) to (2.5d) represent the model of the system and the constraints. Equations (2.5e) and (2.5f) also represent the path that the optimization algorithm uses to achieve the desired set point for the controlled variable. The expressions presented by Equations (2.5g) and (2.5h) permit the optimizer to keep the controlled variable within a deadband without penalization. A more thorough comparison of the ℓ_1-norm and least squares for both estimation and control is provided in [35].

Table 2.2: Nomenclature for general form of the objective function with ℓ_1-norm formulation for dynamic optimization

Symbol	Description
Ψ	minimized objective function result
y	model outputs $(y_0, \ldots, y_n)^T$
$z_t, z_{t,h}, z_{t,l}$	desired trajectory target or dead-band
w_h, w_l	penalty factors outside trajectory dead-band
$c_y, c_u, c_{\Delta u}$	cost of variables y, u, and Δu, respectively
u, x, d	inputs (u), states(x), and parameters or disturbances(d)
f, g, h	equation residuals(f), output function (g), and inequality constraints (h)
τ_c	time constant of desired controlled variable response
e_l, e_h	slack variable below or above the trajectory dead-band
SP, SP_{lo}, SP_{hi}	target, lower, and upper bounds to final set point dead-band

2.3 DAE Initialization Strategies

This dissertation details several strategies to initialize a mathematical representation of a dynamic system to be solved by a simultaneous approach over a time horizon. The purpose of initialization strategies is to find a solution close to the originally intended problem, particularly for those problems that may require a nearby solution for successful and efficient computational methods. In this work, no initialization refers to the case where initial conditions for the problem are the best guess of a reasonable value between lower and upper bounds. When a best guess is poor, the decomposition strategy proposed in this work can identify which set of variables and constraints cannot be solved successfully because the decomposition simulation terminates and reports that the particular block was unsuccessful. The guess values or the form of the equations can then be modified to aide convergence (e.g. avoid divide by zero). In many cases the best guess for decision variables is to hold them constant at nominal values. While this may not be an easy problem to solve, a square system with equal number of equations and variables is first attempted to initialize the problem. If the system is inherently transient or unstable then a key decision variable can be calculated as long as a corresponding output is fixed to maintain a square system of equations. Approaches detailed are with linearization of all or parts of nonlinear equations, analysis of the problem sparsity to create a structural decomposition, warm start from a prior solution, and incremental unbounding of decision variables that leads up to solving the originally intended problem. An overview of the general strategy is presented in Figure 2.2.

These strategies are intended to seed an optimization solver with a nearby solution that may improve the computational performance and ability to find a feasible or optimal solution. The flowchart is intended as a guide for DAE systems where the solver either does not produce a solution or requires excessive computational effort. Not all of the steps are demonstrated in this paper, such as iterating in the decision variable space and filtering in new data. These strategies are the subject of other work [38, 39]. Any step within the flowchart can be consolidated or skipped if a following step is successful. If a prior solution exists, such as from a time-shifted predictive control or estimation, a warm start often improves computational performance [40].

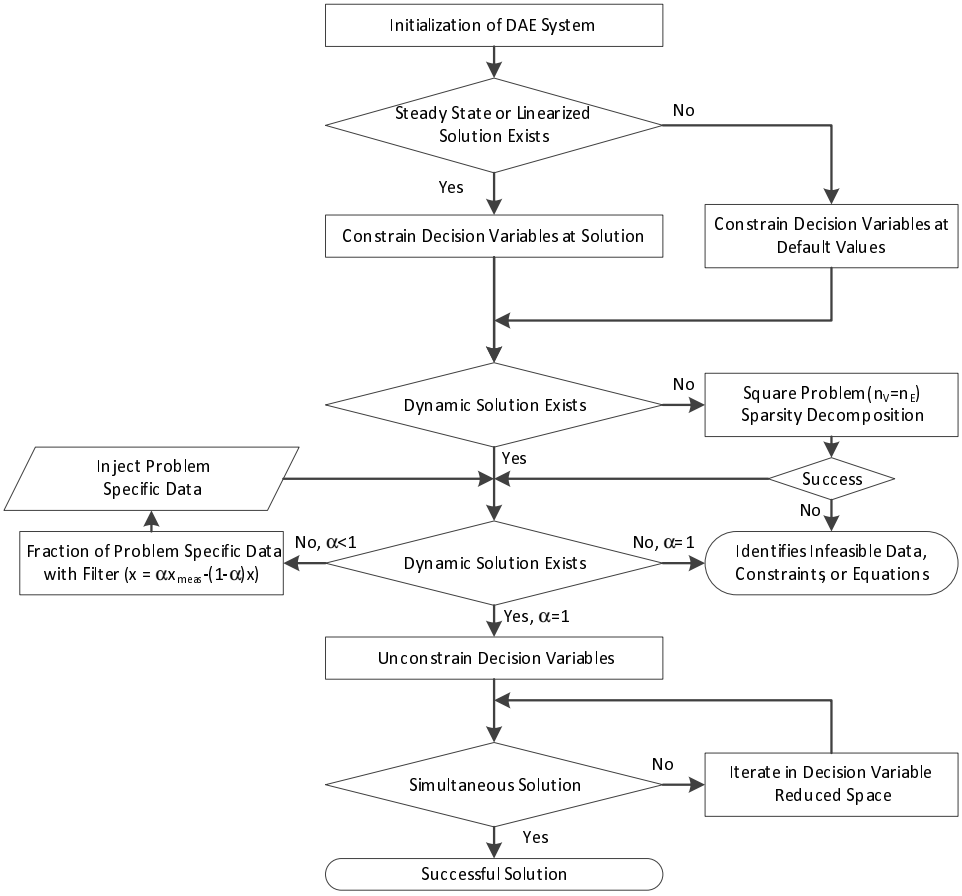

Figure 2.2: Flowchart for initialization of DAE systems

2.3.1 Initialization with Steady-State or Quadratic Approximate Solutions

One method for initialization of nonlinear dynamic models is to simplify the model form so that a solution can be computed and used to seed the original problem with better initial values. Steady-state initialization is accomplished by setting all derivative terms $\frac{dx}{dt}$ to zero and solving the resulting set of equations and objective function. Contour plots identify feasible regions and binding constraints [41] and can provide guidance on proper initialization values to both start feasible as well as seed the optimization. A second method is to take local derivatives of Equation 2.1 to produce a QP form of the model and objective function that is shown in Equation 2.6:

$$\min_u \frac{1}{2} z^T \nabla_{zz} h\, z + \nabla_z h\, z, \quad z = \begin{bmatrix} x & y & u \end{bmatrix}, \tag{2.6a}$$

$$\frac{dx}{dt} = Ax + Bu, \quad A = E^{-1}\nabla f_x, \quad B = E^{-1}\nabla f_u, \quad E = -\nabla f_{\dot{x}} \tag{2.6b}$$

$$y = Cx + Du, \quad C = F^{-1}\nabla f_x, \quad D = F^{-1}\nabla f_u, \quad F = -\nabla f_y \tag{2.6c}$$

With n state variables, m inputs, and p outputs, the dimensions of the matrices in the state space model are $A \in R^{nxn}$, $B \in R^{nxm}$, $C \in R^{pxn}$, and $D \in R^{pxm}$. In many applications derived from first principles models, C simply relates a subset of the states to output variables and D is a matrix of zeros. In some cases, either E or F is numerically singular. In this case, a more general state–space form is preferred as an alternative to Equation 2.6 as $E\frac{dx}{dt} = \tilde{A}x + \tilde{B}u$ and $Fy = \tilde{C}x + \tilde{D}u$. In this case, $\tilde{A} = \nabla f_x$, $\tilde{B} = \nabla f_u$, $\tilde{C} = \nabla f_x$, and $\tilde{D} = \nabla f_u$.

This initialization strategy may also apply to a nonlinear model where there is an explicit solution to linear model predictive control (LMPC) [42–51] and moving horizon estimation [52–56]. A potential strategy for obtaining a close initial guess is therefore to linearize the constraints and create a quadratic approximation to the objective and solve the resulting QP. The linear model solution may be sufficiently close to the nonlinear problem to enable fast convergence. Another point to consider for MHE and MPC is that, except for initializing the controller for the first time, a solution from the prior cycle time is typically available to initialize the current cycle [57]. Time-shifting can perform this initialization, where the entire solution is shifted backward by one time step [58]. The second step becomes the initial condition and each subsequent step receives values from the next step of the prior solution. The final time point can either stay the same or else the model can be integrated by one time step to initialize this final point.

2.3.2 Structural Decomposition of DAE Models

Discretization of DAE models creates sparse and structured NLP or MINLP problems. This sparsity and structure leads to efficient initialization of the optimization problem by breaking the larger problem down into smaller problems [59] that can be solved as independent subsets of variables and equations [60, 61]. An added benefit of successively solving independent sets of variables and equations is that infeasible equations, constraints, data, or other inputs can more easily be identified.

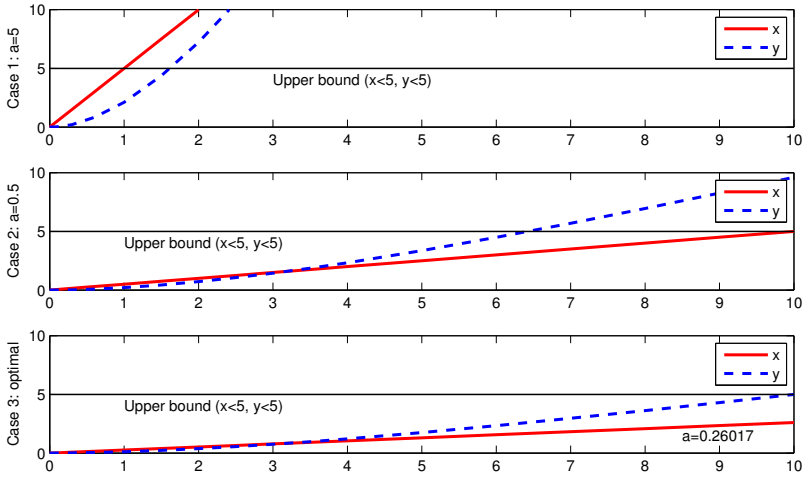

Figure 2.3: Two initialization cases for demonstration of infeasibility detection and a final optimal case

To illustrate the strength of this approach, a simple application with one parameter (p), two variables (x, y), and two equations $\left(\frac{dx}{dt} = a,\ 4\frac{dy}{dt} + y = 3x\right)$ is optimized to maximize the variables x, y by adjusting the parameter a. An upper bound of 5 is placed on each variable. As a first step, the problem is set up as a simultaneous optimization problem and decomposed to reveal independent sets of variables and equations. A first case has parameter $a = 5.0$, causing the value of x to reach the upper limit first. The algorithm correctly identifies the variable and associated equation that first cause an infeasible condition. A second case has parameter $a = 0.5$, causing the value of y to become infeasible before x and the decomposition algorithm again correctly identifies the first offending set. This decomposition does not just identify the particular time step that the problem becomes infeasible but also identifies the specific equation and variable within that time step. A third case in Figure 2.3 shows the optimal solution. While this case is trivial, the identification of an infeasible set may not be obvious for many large-scale or complex problems.

For some problems, such as the one posed above, the inequality constraints lead to an infeasible problem. In this case, the solver minimizes the infeasibility and reports an unsuccessful solution. Although unsuccessful in satisfying all constraints, the new starting point is sometimes valuable for initialization purposes. The infeasibility may be further reduced when degrees of freedom are introduced to the solver as shown in the last subplot of Figure 2.3. As with the energy

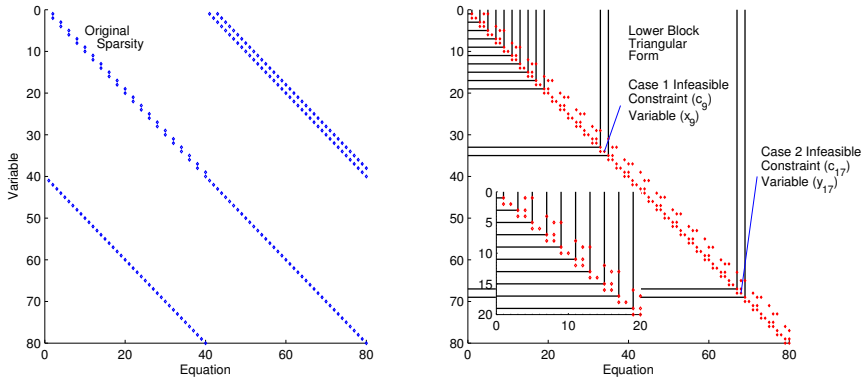

Figure 2.4: Problem is decomposed into independent variables and equations

storage application shown in Section 2.4.4 even an infeasible solution as a starting point may have improved convergence performance.

The decomposition method is to first rearrange the sparsity matrix of the Jacobian (1st derivatives) into a lower block triangular form [62] as shown in Figure 2.4. The next step is to solve each block as an independent set of variables and equations. Once a block is solved, the variable values are fixed and the next block is successively and separately solved from other variables and equations. In the successive solution of equation blocks, figures such as the one shown in Figure 2.4 help identify the infeasible equation(s), if any. This can then be used to resolve the infeasibility. This decomposition strategy is applied to problems that are square with the same number of variables and equations and where a zero-free diagonal is obtained in block triangular form. Sequential simulation is a special case of this method where successive initial value problems are solved to integrate forward in time. The block triangular form has the ability to identify further independent subsets at each time step and thereby show improvement over the time-step sequential strategy.

2.3.3 Initialization of Higher Index DAE Models

Special treatment is required to initialize and determine consistent algebraic and differential conditions for DAE models [19, 63]. The variables that do not appear as differential terms are categorized as algebraic variables. When a dynamic simulation is initialized with state and derivative information, arbitrary selection of the initial conditions may not satisfy the model equa-

tions at the initial time point. This inconsistent set of initial conditions may cause one step ahead (sequential) methods to fail to initialize.

The number of times that algebraic equations must be differentiated to return to ODE form is referred to as the index of the DAE. For example, an index-1 DAE becomes an ODE by differentiating each algebraic equation at most once. Before the development of DAE solvers, it was necessary to convert the DAE model through differentiation or rearrangement into ODE form. A popular algorithm for performing this conversion was developed by Pantelides [64]. Recent advances have alleviated this requirement for solving index-1 DAEs [65], index-2 [66] (Hessenberg form) [67], and automatic differentiation advances [68].

The numerical drift off is a well-known phenomenon for DAE equations that are differentiated to ODE or a lower index DAE form and several methods have been devised to reduce the error [69]. The cause of the drift can be attributed to small errors that integrate over time to cause a substantial deviation from the correct value and are caused by symbolically differentiating the higher index DAE terms back to ODE form. To avoid this drift, higher index DAE models are solved in NLP form with the simultaneous approach discussed earlier. Although the algebraic variables may not be consistent at the initial condition, after one time step of simulation the algebraic equations are consistent with the model equations and other variable values. If consistent initial conditions are required, a small (e.g. 1e-20 *sec*) time step can be taken to resolve the algebraic variables.

2.4 Case Studies on Dynamic Initialization

The following sections demonstrate the potential improvements and details of the DAE initialization approach. The breadth of applications is intended to demonstrate particular concepts as shown in Table 2.3.

2.4.1 Pendulum Motion: Higher Index DAE Forms

A pendulum application is used to investigate the effect of initialization on a range of different forms of the same model. In this case, the model is of a pendulum motion in index-0 (Equation 2.7a), index-1 (Equation 2.7b), index-2 (Equation 2.7c), or index-3 (Equation 2.7d) DAE

Table 2.3: Summary of Case Studies

Section	Description	Key Concepts Demonstrated
2.4.1	Pendulum Motion	Higher Index DAEs
2.4.2	Continuously Stirred Tank Reactor (CSTR)	Initialization with Linearized Equations and Structural Decomposition
2.4.3	Tethered Unmanned Aerial Vehicle (UAV)	Initialization with Sequential Simulation and Structural Decomposition
2.4.4	Smart Grid Energy System	Initialization Strategies and Structural Decomposition

forms as shown in Figure 2.5 and Equation 2.7. More details about the mathematical representation of pendulum problem are available in [70].

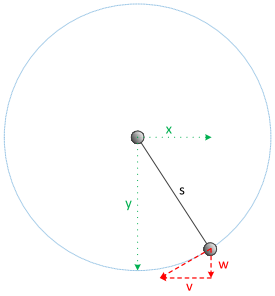

Figure 2.5: Pendulum motion

`Index-0 DAE or ODE Form`

$$\frac{d\lambda}{dt} = \frac{-4\lambda\left(xv + yw\right)}{x^2 + y^2} \tag{2.7a}$$

`Index-1 DAE Form`

$$m\left(v^2 + w^2 - gy\right) - 2\lambda\left(x^2 + y^2\right) = 0 \tag{2.7b}$$

`Index-2 DAE Form`

$$xv + yw = 0 \tag{2.7c}$$

`Index-3 DAE Form`

$$x^2 + y^2 = s^2 \tag{2.7d}$$

An additional 4 equations are shown as Equation 2.8 and are common to all of the pendulum models to describe velocity (v, w) and acceleration $\left(\frac{dv}{dt}, \frac{dw}{dt}\right)$.

$$\begin{aligned} \frac{dx}{dt} &= v \\ \frac{dy}{dt} &= w \\ m\frac{dv}{dt} &= -2x\lambda \\ m\frac{dw}{dt} &= -mg - 2y\lambda \end{aligned} \tag{2.8}$$

Additional parameters include m as the mass of pendulum, g as a gravitational constant, and s as the length of pendulum. The variable λ is a Lagrange multiplier. The simulated motion of the pendulum is shown in Figure 2.6 with both x-axis and y-axis positions as x and y and velocities as v and w, respectively. There is no significant difference between index-1 to index-3 simulation results while the index-0 DAE solution drifts over time as shown in Figure 2.6. DAE initialization with an ODE solver may lead to significant error. A recommended practice is therefore to solve the DAEs with solvers that allow higher index expressions without differentiation.

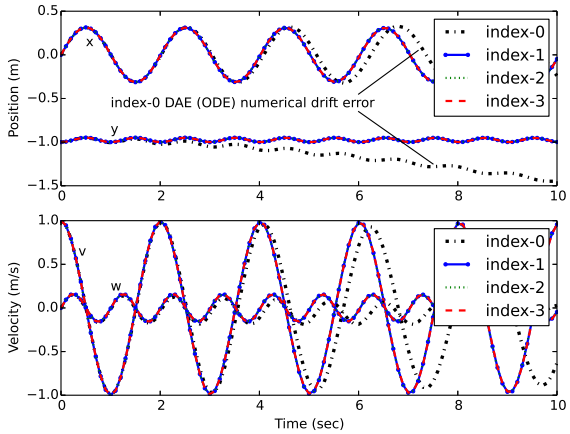

Figure 2.6: Solution to Index-0 to Index-3 DAE model forms

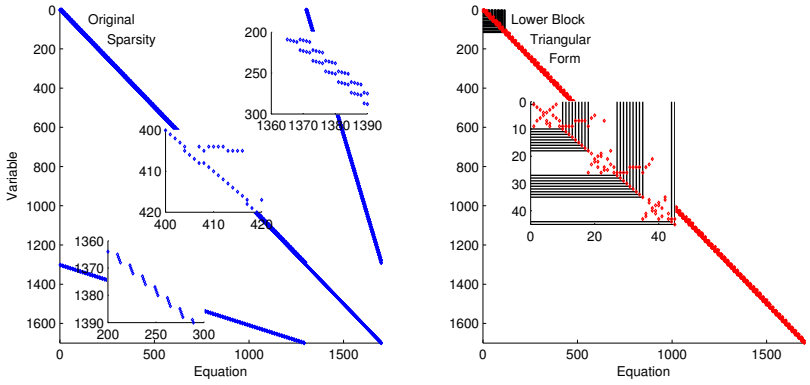

Figure 2.7: Lower block triangular form for pendulum data reconciliation

For initialization, a lower block triangular form of the index-3 DAE sparsity is used to identify small subsets that can be solved independently as shown in Figure 2.7. Each subset of equations is solved successively, leading to an initial solution with default parameters. An alternative approach is to pre-solve the system of equations with no degrees of freedom (DOF). This simulation step is a simultaneous solution of variables and equations but with decision variables fixed at nominal values. Table 2.4 presents results with the APOPT solver [33] while Table 2.5 gives results with the IPOPT solver [71]. With the APOPT solver, the initialization is not required for the index-3 and index-2 models because the initial conditions as default variable values produce a sufficiently accurate guess to enable a successful solution. On the other hand, some cases do benefit from the initialization strategy by decomposition as shown in Tables 2.4 and 2.5. These results show that both the active-set (APOPT) and interior point (IPOPT) sequential quadratic programming (SQP) methods benefit from initialization although the initialization time may increase the total time for some model forms as shown in this particular case.

The subsequent examples demonstrate that performance improvements are often possible with initialization but for the pendulum case there is no CPU-time benefit when considering the combined time of initialization and solution. The fastest solution for index-3 models is with APOPT and no initialization in 15.09 sec. For index-2 models it is with IPOPT and no initialization in 1.40 sec. The combined time for index-1 models is fastest with IPOPT in 2.68 sec although after initialization IPOPT solves the problem in 1.27 sec. Finally, for the index-0 (ODE) model, the fastest combined solution is with IPOPT in 32.5 sec. With IPOPT, a solution is only possible with

Table 2.4: Summary of Initialization Results with APOPT

DAE Form	Strategy	Var	Initialize	Solution	Total	Iter
Index-3	Decompose	3401	2.31 sec	13.37 sec	15.68 sec	24
Index-3	No DOF	3401	6.17 sec	13.72 sec	19.89 sec	24
Index-3	No Init	3401	-	15.09 sec	15.09 sec	19
Index-2	Decompose	3401	3.12 sec	1.78 sec	4.90 sec	6
Index-2	No DOF	3401	5.81 sec	2.36 sec	8.17 sec	4
Index-2	No Init	3401	-	6.46 sec	6.46 sec	8
Index-1	Decompose	3401	30.8 sec	2.25 sec	33.1 sec	4
Index-1	No DOF	3401	Failed	-	-	-
Index-1	No Init	3401	-	Failed	-	-
Index-0	Decompose	3601	37.5 sec	3.53 sec	41.0 sec	3
Index-0	No DOF	3601	Failed	-	-	-
Index-0	No Init	3601	-	Failed	-	-

Table 2.5: Summary of DAE Initialization Results with IPOPT

DAE Form	Strategy	Var	Initialize	Solution	Total	Iter
Index-3	Decompose	3401	4.82 sec	Failed	-	-
Index-3	No DOF	3401	1.41 sec	Failed	-	-
Index-3	No Init	3401	-	Failed	-	-
Index-2	Decompose	3401	5.12 sec	0.93 sec	6.05 sec	17
Index-2	No DOF	3401	1.28 sec	0.52 sec	1.80 sec	11
Index-2	No Init	3401	-	1.40 sec	1.40 sec	28
Index-1	Decompose	3401	44.1 sec	1.27 sec	45.4 sec	4
Index-1	No DOF	3401	Failed	-	-	-
Index-1	No Init	3401	-	2.68 sec	2.68 sec	41
Index-0	Decompose	3601	31.2 sec	1.29 sec	32.5 sec	20
Index-0	No DOF	3601	Failed	-	-	-
Index-0	No Init	3601	-	Failed	-	-

initialization because the solver failed to find a solution within 100 iterations when the problem was terminated.

2.4.2 Linear Initialization: CSTR Case Study

In linearized state-space form, it is generally easier to obtain an implicit solution to the dynamic optimization problem. For small systems, it is possible to obtain an explicit solution to

MHE and MPC. The solutions with linearized models are then used to initialize the nonlinear case. Prior work shows that initialization with linear or convex approximations to parameter estimation problems improves the convergence properties of the nonlinear or possibly non-convex problems [72]. A continuously stirred tank reactor (CSTR) with first order kinetics is a common benchmark problem used in other studies to demonstrate estimation [73] and control [74] algorithms. Species A and an energy balance equation for the CSTR in Figure 2.8 are shown in Equation 2.9. The reactor is fed with chemical A and a diluent. The objective is to maintain temperature control below 400 K in the reactor and the concentration of A below $0.2\ mol/L$.

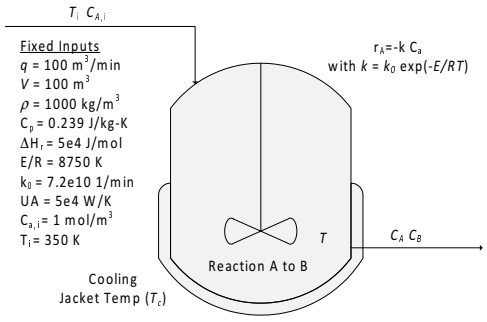

Figure 2.8: Continuously Stirred Tank Reactor

$$V\,\frac{dC_a}{dt} = q\left(C_{af} - C_a\right) - k_0 exp\left(-\frac{E}{R\,T}\right) V\,C_a \tag{2.9a}$$

$$\rho V C_p \frac{dT}{dt} = q\left(T_f - T\right) + \Delta H_r\, k_0 exp\left(-\frac{E}{R\,T}\right) V\,C_a + UA\left(T_c - T\right) \tag{2.9b}$$

With an elevated jacket temperature, without a controller in place, the reactor experiences temperature run-away as shown in Figure 2.9 due to the exothermic heat generation and exponential dependence on temperature. The exponential increase in temperature is also accompanied by a decrease in concentration of species A. The uncontrolled reactor temperature violates the upper limit on reactor temperature of 400 K. Solving the simulation case with zero degrees of freedom, as shown above, helps develop a feasible solution for the problem. This feasible solution can then be used to initialize the decision variables for the main nonlinear CSTR problem.

A Nonlinear Model Predictive Controller (NMPC) is developed to reduce the concentration of A below $0.1\ mol/L$ and maintain the temperature between $375 - 380\ K$. A reference trajectory

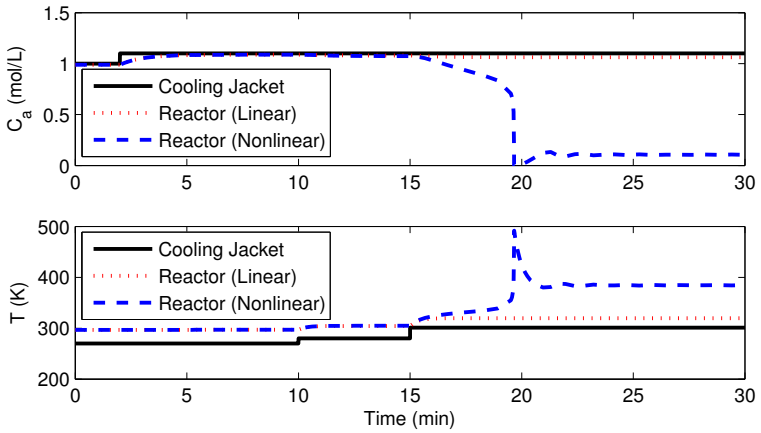

Figure 2.9: Uncontrolled linear and nonlinear response

with an ℓ_1-norm deadband [35] guides the approach to the desired setpoint as shown in Figure 2.10. The nonlinear MPC is initialized with a preliminary linear MPC solution (Equation 2.10b) or through structural decomposition. This potential initialization strategy is to solve a lower block triangular form of the nonlinear MPC to initialize the state and parameter values for a warm start near the desired solution (see Figure 2.11).

$$\begin{bmatrix} \frac{dC_a}{dt} \\ \frac{dT}{dt} \end{bmatrix} = \begin{bmatrix} -\left(\frac{q}{V}+k\right) & -k\frac{E}{RT^2} \\ \frac{\Delta H_r k}{\rho C_p} & \left(-\frac{q}{V}-\frac{UA}{\rho C_p V}+\frac{\Delta H_r k}{\rho C_p}\frac{E}{RT^2}\right) \end{bmatrix} \begin{bmatrix} C_a \\ T \end{bmatrix} + \begin{bmatrix} \frac{q}{V} & 0 & 0 \\ 0 & \frac{q}{V} & \frac{UA}{\rho C_p V} \end{bmatrix} \begin{bmatrix} C_{a,i} \\ T_i \\ T_c \end{bmatrix} \tag{2.10a}$$

$$\begin{bmatrix} \hat{T} \end{bmatrix} = \begin{bmatrix} 0 & 1 \end{bmatrix} \begin{bmatrix} C_a \\ T \end{bmatrix} + \begin{bmatrix} 0 & 0 & 0 \end{bmatrix} \begin{bmatrix} C_{a,i} \\ T_i \\ T_c \end{bmatrix} \tag{2.10b}$$

The original sparsity structure is shown on the left of Figure 2.11 while the reordered set of variables and equations appears on the right. The first 10 variable blocks are shown as successively larger blocks. The CSTR simulation has excellent decomposition with a maximum block size of 7 and a minimum block size of 2. The blocks represent the number of variables and equations that are independent and can be solved prior to other variables and equations.

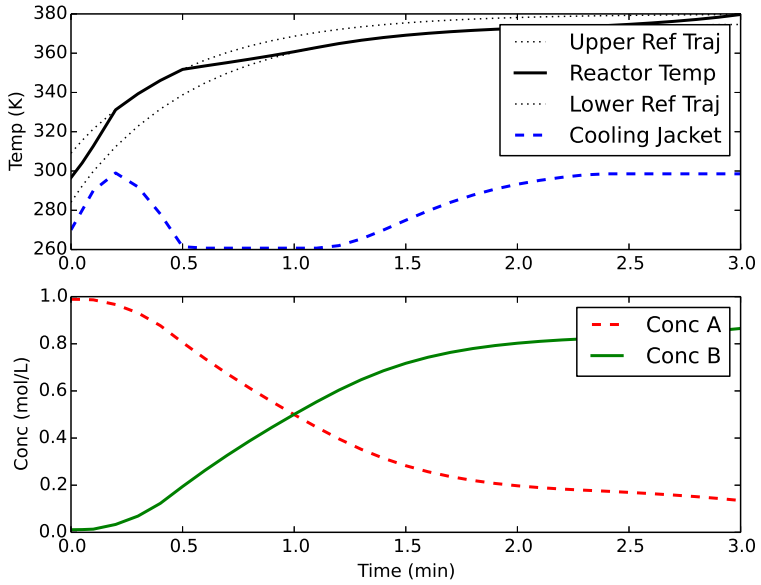

Figure 2.10: Nonlinear MPC solution with linear MPC initialization

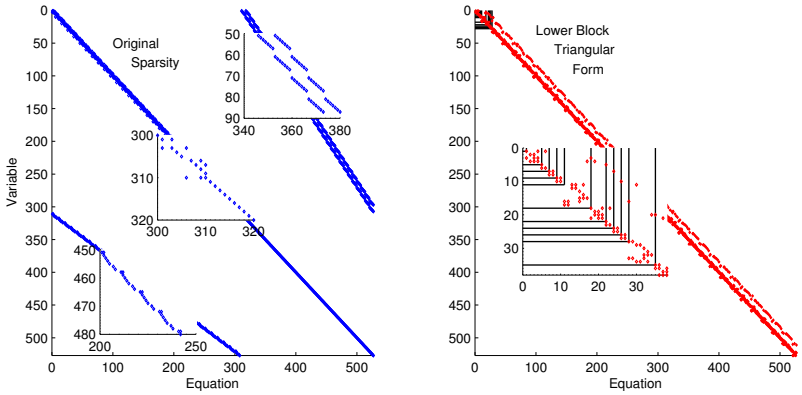

Figure 2.11: Lower block triangular form for nonlinear MPC of a CSTR

Table 2.6: CSTR MPC comparison of linear pre-solve, block diagonal decomposition, and no initialization

Solver	**Strategy**	**Var**	**Initialize**	**Solution**	**Total**	**Iter**
APOPT	Decompose	1054	0.10 sec	0.51 sec	0.61 sec	13
APOPT	Linear	1054	0.17 sec	0.45 sec	0.62 sec	18
APOPT	No Init	1054	-	0.95 sec	0.95 sec	27
IPOPT	Decompose	1054	0.42 sec	0.64 sec	1.06 sec	40
IPOPT	Linear	1054	0.51 sec	2.01 sec	2.52 sec	119
IPOPT	No Init	1054	-	1.27 sec	1.27 sec	65
SNOPT	Decompose	1054	0.11 sec	0.37 sec	0.48 sec	23
SNOPT	Linear	1054	0.15 sec	2.78 sec	2.93 sec	108
SNOPT	No Init	1054	-	Failed	-	-

Table 2.6 gives results for solvers APOPT [33], IPOPT [71], and SNOPT [75] with three scenarios including decomposed solution initialization, linear pre-solve, and no initialization except use of initial conditions. The fastest solution case is with a decomposition solution with SNOPT with a total time of 0.48 *sec*. The nonlinear MPC case is initialized with only the initial conditions that are propagated forward across the time horizon before solution begins. The best solution time without initialization is with APOPT at 0.95 *sec* or twice the CPU time even when the additional pre-solve decomposition time is included. For SNOPT, a solution is only possible with initialization because the original problem fails to solve after 500 iterations. An important result from this CSTR study is that initialization effectiveness is solver dependent but that an initialization strategy tends to improve solution time for all solvers. At a future point, solvers may incorporate initialization strategies that exploit the high degree of DAE problem structure to provide a feasible starting point.

2.4.3 Tethered Aerial Pipeline Inspection: Initialization with Sequential Simulation

One of the limitations of small Unmanned Aerial Vehicles (UAV) is the limited range with current battery technology and regulatory hurdles for autonomous and commercial flights in many jurisdictions. One method to overcome both of these obstacles for infrastructure inspection is to tether the aerial vehicle to a ground vehicle. The tether can provide a communication and power conduit to the UAV to allow it to remain aloft indefinitely. The ground vehicle and aerial UAV may be a fully automated system that is designed to regularly monitor infrastructure such as levee systems, bridges, dams, pipelines, electrical transmission cables, and other large scale structures.

In this simulation, a UAV is tethered to an autonomous ground vehicle. As the ground vehicle drives to the side of a pipeline, a multi-copter UAV hovers above the pipeline with an array of cameras and leak detection sensors. The cable that connects the UAV to the ground robot is specified to be 25 m in length. In this case the cable length is fixed although a retractable ground vehicle-based or UAV-based cable is possible to adjust cable length and maintain cable tension.

A simplified model of this multi-agent optimization problem consists of DAEs as shown in [3] but with a fixed position for the ground robot instead of dynamic equations for the drogue. The sparsity and structural decomposition are shown in Figure 2.12. The cable system dynamics are modeled by discrete nodes at regularly spaced intervals along the cable. The elasticity of the

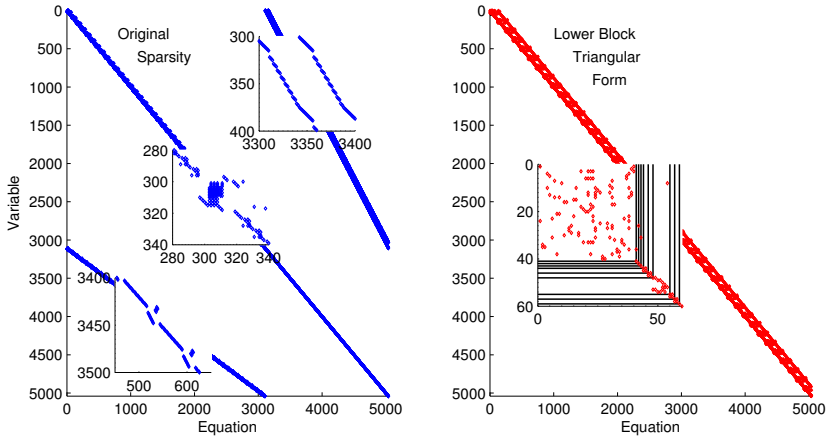

Figure 2.12: Lower block triangular form for a tethered UAV

cable, cross-wind disturbances, movement of the aerial and ground robots all contribute to the complex cable and UAV movement. The dynamics of the cable are important to plan a path for the UAV that maintains a minimum tension on the cable to avoid excessive slack. A secondary objective beyond maintaining tension limits is to fly along a corridor above the pipeline and keep pace with the movement of the ground vehicle. For fixed wing vehicles, a minimum relative air velocity is required to maintain lift on the vehicle. A minimum relative air velocity is enforced in this simulation although not required by a multicopter platform.

Unique aspects of this example problem for DAE initialization are that it is an unstable system, highly nonlinear, and has many decision variables. The optimizers plan a path for the UAV by adjusting the acceleration of the UAV in north, east, and vertical directions. Acceleration limits $\left(1\frac{m}{s^2}\right)$ are enforced to emulate responsive yet limited UAV capabilities. The optimizers seek to maintain tension, elevation above pipeline, position over the pipeline, and air velocity to meet monitoring objectives.

For this application, initialization steps are critical to first obtain a feasible and then optimal solution. In this case, the initialization is accomplished with either the lower block triangular solution or else with a single simulation with no degrees of freedom. The dynamic optimization of $5,670$ variables and $5,544$ equations is solved in APMonitor (APOPT, IPOPT, and SNOPT solvers) with a 2.4 GHz Intel i7-2760QM Processor. The results for this analysis are summarized

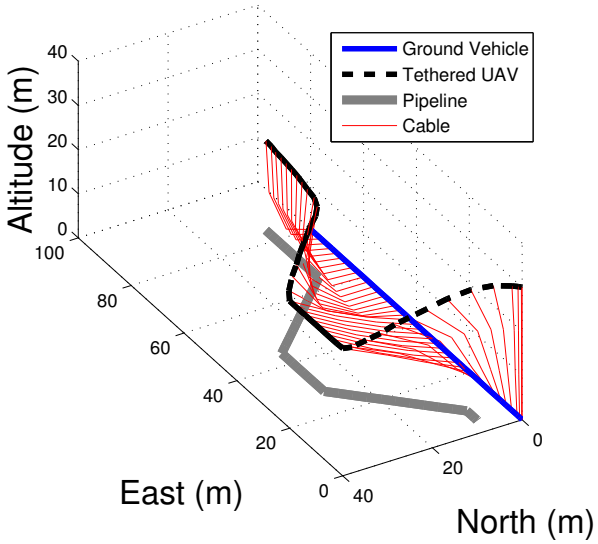

Figure 2.13: A simulated tethered UAV performs surveillance of a pipeline.

in Table 2.7. Without initialization, the solvers fail to find a solution with a maximum of $1,000$ iterations and CPU time of $3,600$ *sec*.

Table 2.7: Tethered UAV comparison of linear pre-solve, block diagonal decomposition, and no initialization

Solver	**Strategy**	**Var**	**Initialize**	**Solution**	**Total**	**Iter**
APOPT	Decompose	5670	3.1 sec	246.9 sec	250.0 sec	298
IPOPT	Decompose	5670	15.1 sec	47.2 sec	62.3 sec	255
SNOPT	Decompose	5670	3.2 sec	31.6 sec	34.8 sec	164
APOPT	No DOF	5670	2.6 sec	292.0 sec	294.6 sec	96
IPOPT	No DOF	5670	7.8 sec	61.7 sec	69.5 sec	158
SNOPT	No DOF	5670	4.4 sec	136.0 sec	140.4 sec	656
APOPT	No Init	5670	-	Failed	-	1,000
IPOPT	No Init	5670	-	Failed	-	1,000
SNOPT	No Init	5670	-	Failed	-	1,000

2.4.4 Smart Grid Energy System: Structural Decomposition

Cryogenic carbon capture (CCC) is a new technology for separation of CO_2 from flue gas. In this process, CO_2 is separated by cooling the temperature to lower than the CO_2 freezing point. The main advantages of the CCC process are low energy consumption, fast response to load

changes, and energy storage capability. The latter advantage is critically important for grid stability, especially in the face of a large penetration of renewable energy. Time-shifting the electricity demand of the CCC process is a result of the energy storage capability that can positively influence power grid stability. Integration of the CCC process with grid-scale power generation units including coal, gas, and wind power units is detailed in Chapters 4 to 6. The integrated system without energy storage is considered as an example case study for initialization purposes. A schematic diagram of the integrated system is shown in Figure 2.14.

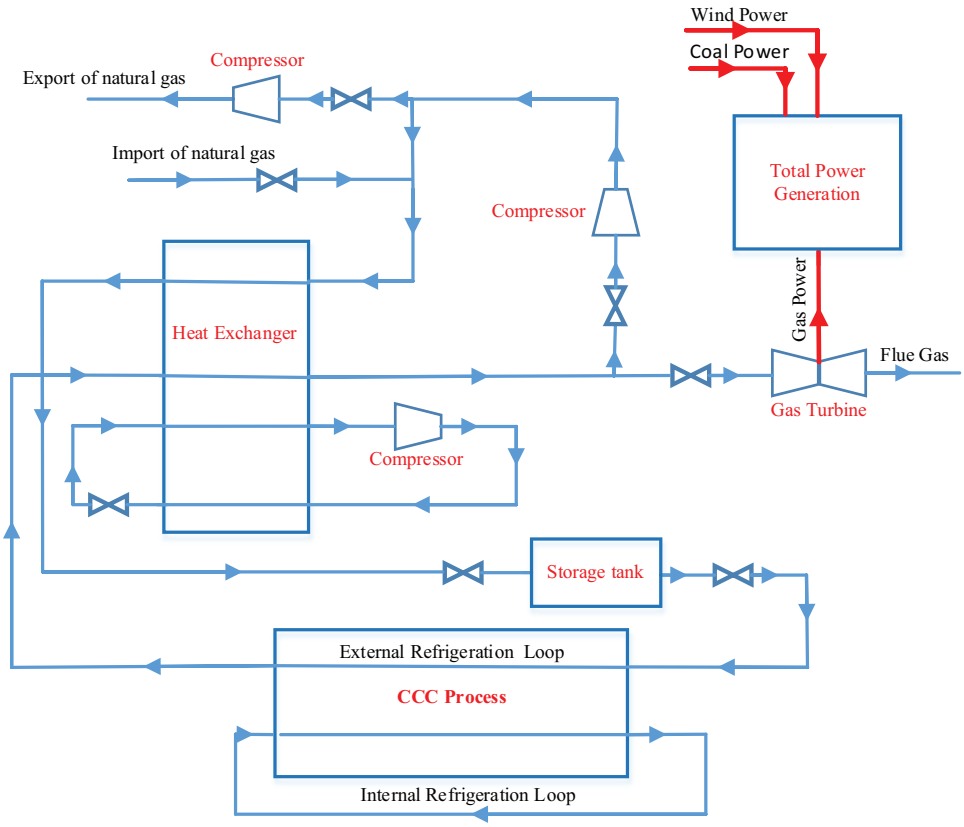

Figure 2.14: Hybrid system of CCC process and power generation units

The refrigeration cycles in the CCC process and integration of the process with power generation units make it a complicated system where many of the variables are co-dependent. The sparsity and structural decomposition of this system are shown in Figure 2.15. The model decomposes into 3072 separate blocks with the largest block at 14 variables and the smallest block at 1

variable. The independent blocks are, however, dependent on prior solutions of other independent blocks.

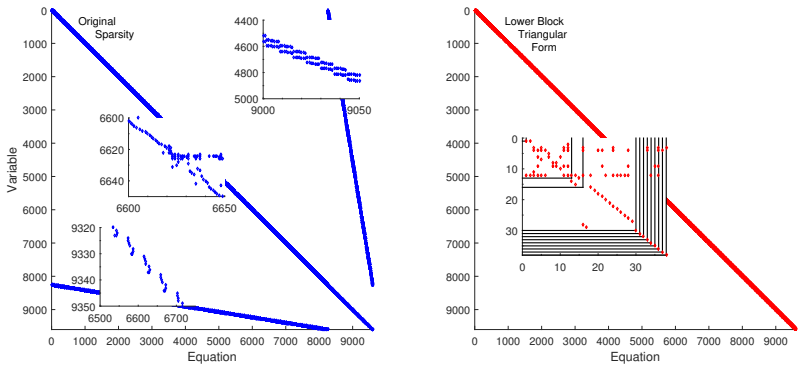

Figure 2.15: Lower block triangular form for hybrid system of CCC process and power generation units

The goal in this study is to maximize the operational profit of the integrated system. The hybrid system is required to meet the total electricity demands of the CCC process and residential area. In addition, the amount of the power produced should be controlled to avoid the excess power production. A dynamic optimization framework is used with a time horizon of 8 days and 1 hour time increments are considered. Consideration of eight days as the simulation time ensures that the results are not influenced by the initial and boundary conditions. The results for the three middle days of interest are shown in Figure 2.16. The number of variables and equations are $15,552$ and $14,784$, respectively, leading to 768 decision variables. This is more than the decomposition case ($9,600$ variables and equations) or the dynamic simulation case ($7,488$ variables and equations) because of the additional equations and variables necessary to implement reference trajectories and manipulated variable tuning. The 768 decision variables are the amount of coal and natural gas combusted for power production and the amount of natural gas imported to and exported from the plant at each time step. The model is implemented in APMonitor and is solved using the APOPT solver. The optimization problem is solved on a Dell R815 Server with an AMD Opteron Processor 6276 (2.3 GHz).

Without initialization of the problem, the solver fails to obtain a solution with a maximum of 400 iterations and CPU time of 14 *hr*. Several initialization strategies are used to obtain a feasible solution: (1) Nominal values are assigned for the decision variables and the problem and

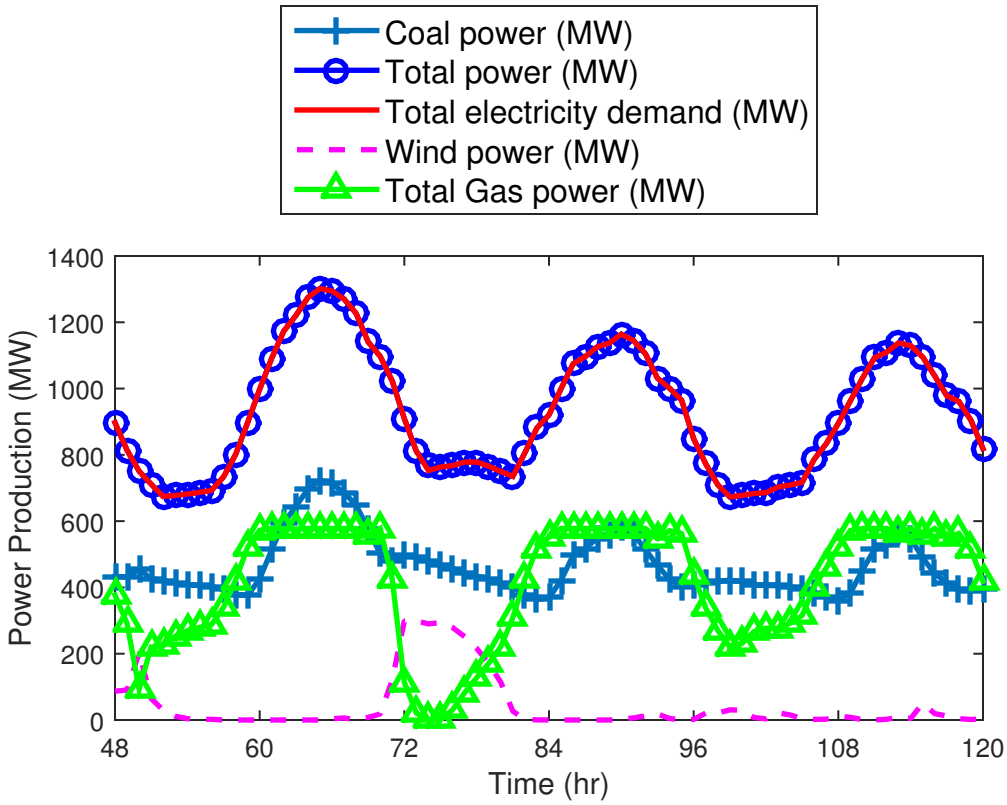

Figure 2.16: Power and demand profiles for the hybrid system of CCC process and power generation units

objective equations are solved with equal numbers of variables and equations (square problem), (2) the square problem is solved by using the structural decomposition of the equations, (3) restart from simultaneous dynamic simulation with all degrees of freedom fixed at specified values, and (4) restart from sequential dynamic simulation where initialization is accomplished by solving the square problem in a sequential time-step approach. With the strategies described above, the decision variables are initialized from the simulation case and the optimization case is solved. In this stage, decision variables are obtained by the optimizer. The combined CPU times for both the initialization and final solution for each case are summarized in Table 2.8. Results for IPOPT and SNOPT are not reported because the solvers failed for all cases. The computational time of each initialization step is reported in seconds as well as the total computational time in hours.

Of all of the cases, only case 4 had a feasible solution after the initialization step. The other cases also produced a solution but the solver was not able to find feasible values to satisfy all of the equations within a specified convergence tolerance. Interestingly, even starting from the infeasible

Table 2.8: Computation time for hybrid system of a CCC process and power generation units

Case	Strategy	Var	Initialize	Total	Iter
0	No Initialization	15,552	Skipped	Failed	400
1	Simultaneous simulation with objective equations	9,600	57.5 sec	5.56 hr	214
2	Structural decomposition as shown in Figure 2.15	9,600	25.6 sec	5.55 hr	214
3	Simultaneous simulation without objective equations	7,488	25.4 sec	5.54 hr	214
4	Sequential simulation initialization	7,488	2.5 sec	2.67 hr	137

solution helped the optimization case to find a successful solution. As it is seen from Table 2.8, initializing the optimization problem with a sequential dynamic solution of the square problem has the least amount of computation time while the other three cases take approximately the same amount of time to achieve a successful solution. The result of the optimization case is shown in Figure 2.16, where total electricity demand of the hybrid system is met through a combination of the coal, gas, and wind power.

2.5 Conclusions

A contribution of this dissertation is a strategy for improved initialization of dynamic systems. Techniques include structural decomposition, pre-solve with linear models, and initialization with no degrees of freedom. The dynamic models are often hybrid systems of fundamental relationships and empirical parameters that can be adjusted to fit model predictions to data or optimized over a time horizon. The discretized sparse structure is restructured to identify independent sets of variables and equations that can be solved successively and independently. Higher index DAEs, integral equations, and higher order derivatives fit into a general framework for addressing large-scale optimization of dynamic systems. Several case studies motivate the use of initialization to improve solution time and enable successful solutions. While all initialization strategies used in this analysis helped the convergence of the problem, finding the best approach for different problems is the focus of future work.

CHAPTER 3. FRAMEWORK FOR DYNAMIC PARAMETER ESTIMATION AND OPTIMIZATION

3.1 Introduction

There are approximately 40,000 distillation columns in the US that are used to separate chemical compounds based on vapor pressure differences in industries ranging from oil and gas to pharmaceuticals. These separation columns consume 6% of the yearly US energy demand [76]. While many of the large production facilities use continuous processes, specialty and smaller-use items are often processed in batch columns [77–79]. Continuous distillation columns have been the focus of optimization work since the first column was built, but the transient nature of batch columns has caused many to remain unoptimized. The transient nature of the market for these specialty items has further hindered the optimization of batch columns [78]. As a result, little research on batch column optimization is available in the literature before 1980 [80–83]. Work on batch columns has increased in the last 30 years as computers have become more sophisticated, and several studies have considered both advanced solving techniques and advanced column configurations [84–98]. Terwiesch, et al. [99] and Kim and Diwekar [100] provide a detailed history of the subject and a description of current batch distillation modeling and optimization methods.

The optimization of the batch columns can be subdivided into optimal design problems and optimal control problems. Optimal design problems generally deal with column configuration, while optimal control problems deal with column operation. These ideas are summarized well in separations textbooks such as Diwekar [85], Stichlmair and Fair [101] and Doherty and Malone [102] and will therefore not be discussed further here. Research studies on this subject follow the same general outline as presented in the textbooks [78, 103]. The models developed for batch column optimization generally fall into two categories: first-principles models and shortcut or simple models.

First-principles models are those with governing mass and energy balance equations, detailed thermodynamics, tray dynamics, system non-idealities and variable flow rates [104–107]. These models are theoretically more accurate than shortcut methods, but they are only as accurate as the thermodynamic and physical property models they use [78]. The use of these models has been limited due to high computational costs. Several studies have been conducted using first-principles models and advanced solving techniques to reduce computational cost [57, 108–113]. While these models accomplish the goal of reducing computational load, they are generally still slower than shortcut models. In addition, the lack of experimental data for batch columns makes it difficult to determine how much accuracy is lost when going from first-principles to lower-order (first-principles model with advanced or simplified numerical methods) to shortcut models [114].

The second class of models, shortcut models, has received far greater attention. These models contain less physics and are generally used for ballpark estimates and comparative studies. A typical set of assumptions for these models is as follows: constant boil-up rate, no external heat loss, ideal stages, constant relative volatility, constant molar overflow, total condenser without subcooling and no column holdup [103, 106, 115–117]. More recent shortcut models have kept most of the same assumptions while accounting for column dynamics using a non-zero column holdup [111, 114]. The primary purpose of these models is to create an accurate, computationally fast simulation for use in design and control of batch columns. While these models achieve the reduction in computational load, the lack of experimental data makes it difficult to determine the accuracy of these models [114]. The assumptions made in these models limit their use to ideal systems.

The gap between first-principles models and shortcut models is large. First-principles models can provide predictions for many systems but require thermodynamic and physical property models as inputs, while the assumptions in shortcut models make them applicable only to a small class of relatively ideal systems. In this work, a method is proposed for developing shortcut models with relaxed assumptions. The method is based on fitting parameters in place of simplifying assumptions to include system non-idealities without solving the first-principles equations. Solving for the fitting parameters requires extensive experimental data whereas first-principles models typically need less data, being based on fundamental correlations. Dynamic parameter estimation can be used to reduce the experimental load. The case study presented in this work required only one

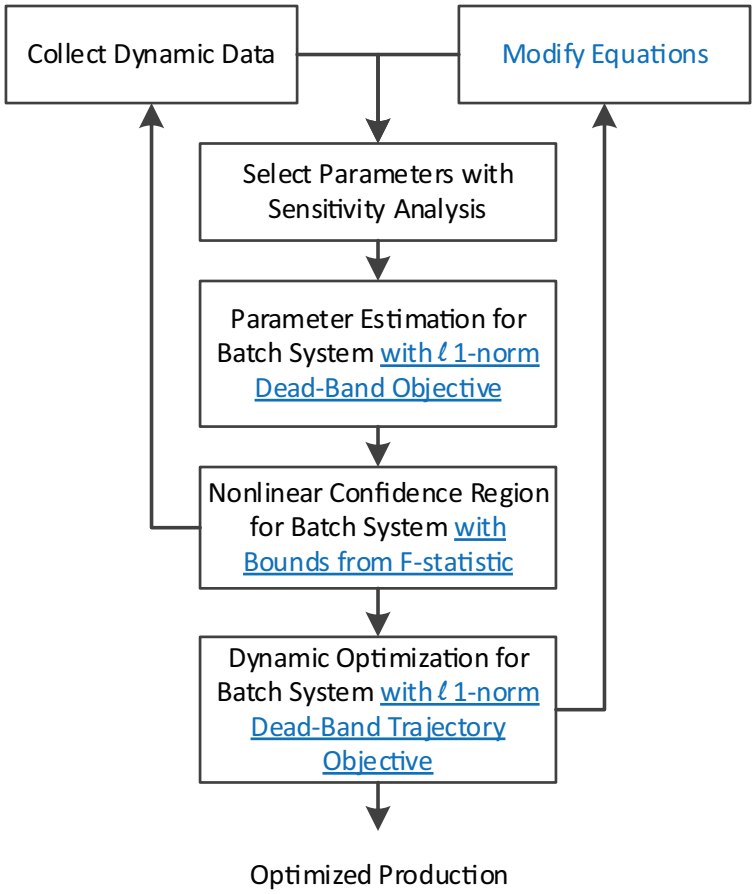

Figure 3.1: Overview of methodology for batch column optimization with novel contributions underlined

experiment to determine model parameters. As with any model containing fitting parameters, there is concern over the accuracy of the parameters. By using nonlinear statistics [118] and a model sensitivity analysis [119], it is possible to determine how many parameters can be estimated from the collected data and the acceptable range for those parameters. These steps are shown in Figure 3.1 (also shown in Chapter 1). Underlined elements of the methodology in Figure 3.1 indicate the new approach to batch separation systems.

The well-known methodology shown in Figure 3.1 is applied to an experimental case study. The methodology includes the use of ℓ_1-norm dynamic parameter estimation, nonlinear statistics [118,120], and a model parameter sensitivity analysis [119]. These techniques are applied together to a batch distillation column in a holistic approach to dynamic optimization. Models developed using this method account for system non-idealities not seen in typical shortcut models without sacrificing computational speed.

It should be emphasized that the dynamic parameter estimation, nonlinear statistics, and control frameworks developed for the batch distillation column are applicable more generally to complex dynamic systems. The general frameworks used for modeling, estimation, and control of this problem are discussed in Section 2.2. In Section 3.1.1, the general equations used to represent the nonlinear statistics and sensitivity analysis are overviewed.

3.1.1 Confidence Intervals and Sensitivity Analysis

Reliability of the parameters is investigated by implementing an approximate nonlinear confidence interval calculation [118]. Non-linear confidence intervals can be found by solving Equation 3.1 for the sets of parameters that make up the joint confidence region [121], then extracting the upper and lower bounds of that region in each dimension.

$$\frac{J(\theta) - J(\theta^*)}{J(\theta^*)} \leq \frac{p}{n-p} F_{n,n-p,1-\alpha} \tag{3.1}$$

In Equation 3.1, $J(\theta)$ is the error between the measurements and the model prediction at a value θ of the parameters, $J(\theta^*)$ is the error between the measurements and the model prediction at the best estimates of the parameters (θ^*), p is the number of parameters in the model, n is the number of data points, and $F_{n,n-p,1-\alpha}$ is the F-statistic at n and $n-p$ degrees of freedom with a confidence level of $1-\alpha$. The squared error objective is the only form of the nonlinear confidence interval that has a theoretical foundation. This is because the F-statistic used to define the confidence region is a ratio of χ^2 distributions that compares the equivalence of two sets of experimental results. The χ^2 distributions are intended for least square objectives instead of ℓ_1-norm objectives. According to the author's knowledge, an equivalent F-statistic for nonlinear confidence intervals and the ℓ_1-norm has not been derived. A nonlinear confidence interval for ℓ_1-norm objectives based on the F-statistic is future work.

It is also desirable to determine the number of parameters that can be estimated or are observable given a particular model form and set of data. Large confidence intervals signal that a particular parameter may not be observable or that the effect of that parameter may be co-linearly dependent with other parameters. A well-known systematic analysis is used to determine which parameters can be estimated and rank the parameters in terms of the ability of a particular parameter

to improve a particular model estimate [119, 122]. This procedure is accomplished in 3 steps: (1) efficient computation of the sensitivities, (2) scaling of the dynamic parameter sensitivities, and (3) singular value decomposition of the scaled sensitivity matrix to reveal an optimal parameter space transformation.

The first step in performing the parameter analysis is to compute the state dependencies to changes in the parameters. This can be accomplished with a variety of methods. One such method is to compute a finite difference sensitivity of the parameters with a series of perturbed simulations [123, 124]. A second method is to augment the model with adjoint equations that compute sensitivities simultaneously with the model predictions [125]. A third method is a post-processing method with time-discretized solutions to differential equation models [3, 8, 126]. This post-processing method involves efficient solutions to a linear system of equations, especially over other methods for large-scale and sparse systems [17].

The sensitivity is computed from time-discretized models that are solved by nonlinear programming solvers. At the solution, exact first derivatives of the equations with respect to variables are available through automatic differentiation. These derivatives are available with respect to the states ($\nabla f_x(x,\theta)$) and parameters ($\nabla f_p(x,\theta)$). For the objective function, objective gradients are computed with respect to states ($\nabla J_x(x,\theta)$) and parameters ($\nabla J_\theta(x,\theta)$). Sparsity in those matrices is exploited to improve computational performance, especially for large-scale systems. Sensitivities are computed by solving a set of linear equations as shown in Equation 3.2 with parameter values fixed at $\bar{\theta}$ and variable solution $\bar{x}$ as nominal values.

$$\begin{bmatrix} \nabla_x f(\bar{x},\bar{\theta}) & \nabla_\theta f(\bar{x},\bar{\theta}) & 0 \\ \nabla_x J(x,\theta) & \nabla_\theta J(x,\theta) & -I \\ 0 & I & 0 \end{bmatrix} \begin{bmatrix} \nabla_\theta x \\ \nabla_\theta \theta \\ \nabla_\theta J(\bar{\theta}) \end{bmatrix} = \begin{bmatrix} 0 \\ \Delta\theta_i = 1 \\ 0 \end{bmatrix} \tag{3.2}$$

To further improve the efficiency of this implementation, an LU factorization of the left hand side (LHS) mass matrix is computed. This LU factorization is preserved for successive solutions of the different right hand side (RHS) vectors because the LHS does not change and successive sparse back-solves are computationally efficient in comparison with the LU factorization. Each matrix inversion computes the sensitivity of the states to a particular parameter. Each parameter is successively set equal to a change of $\Delta\theta_i = 1$. All other elements of the vector on the RHS

are set to 0. The solution to this matrix inversion computes the sensitivity of all variables in the time horizon with respect to a particular parameter $S = (\nabla_\theta x)$. It also computes the sensitivity of the objective function with respect to the parameters $\left(\nabla_\theta J(\bar{\theta})\right)$.

To summarize the sensitivity analysis, an efficient method is presented to compute sensitivities as a post processing step that is efficient even for large-scale and sparse systems. The sensitivity matrix is decomposed into singular values and eigenvectors that give the relative magnitude and linear combination of parameters that are orthogonal. In this study, the transformed parameters are not estimated directly but instead used as an advisory tool to determine which parameters and how many can be estimated.

3.2 Dynamic Estimation and Optimization for a Batch Distillation Column

This established methodology is demonstrated for the first time on a binary batch distillation column. While the methods are not new, the application to this specific column is novel and gives experimental insight on issues encountered when applying dynamic optimization on applications that share common features. This section is subdivided into a brief discussion of the apparatus and experimental procedure, parameter estimation and validation, and model optimization and validation.

3.2.1 Apparatus and Experimental Procedure

A 38 tray, 2 inch, vacuum-jacketed and silvered Oldershaw column is used to collect all experimental data (see Figure 3.2). Cooling water supplies the energy sink for the total condenser at the top of the column. A 600 W reboiler heater is the only source of energy input. Reflux ratio is set using a swinging bucket and can be changed as frequently as every 5 minutes. The instantaneous distillate composition is determined using the refractive index of the solution and the total distillate collected is determined via a graduated cylinder. Cumulative distillate composition can be measured and inferred using the instantaneous compositions and a mass balance. The instantaneous distillate composition can be measured every 5 minutes. The reboiler is initially charged with 1.5 L of a 50/50 wt% mixture of methanol and ethanol for each run, with the goal being a product of 99 mol% methanol.

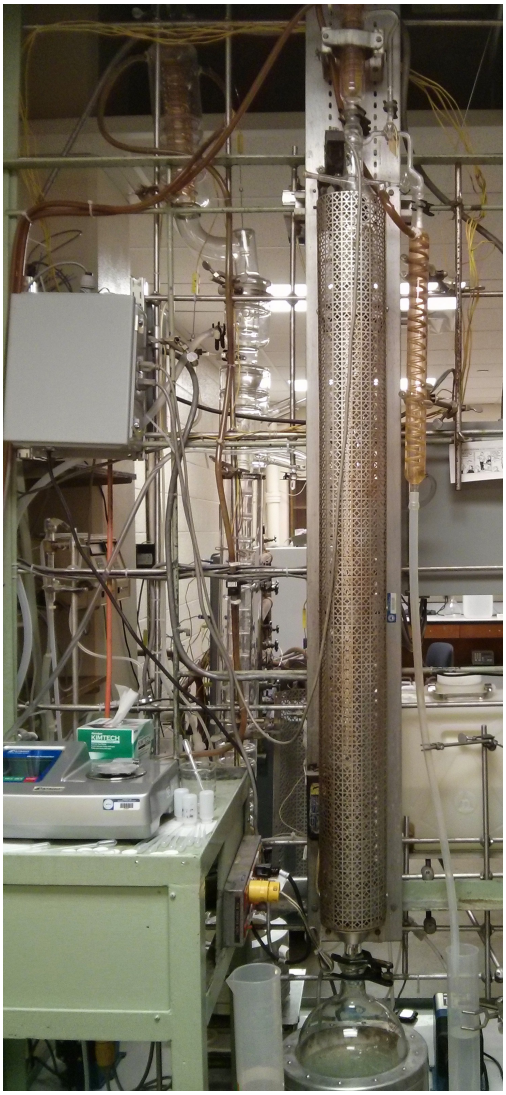

Figure 3.2: Apparatus used for the experiments

The non-optimized base case experiment consists of running the column at total reflux for 30 minutes, then setting the reflux ratio to a constant value, usually somewhere between 3 and 5, and letting the column run until the cumulative overhead composition reaches 99 mol% methanol. The collection time usually lasts 60 to 90 minutes, depending on the reflux ratio. The instantaneous and cumulative compositions for a typical run, as well as the amount of product collected, can be seen in Figures 3.3a and 3.3b, respectively. In this case, running the column at total reflux for 30 minutes, then using a constant reflux ratio of 4 for the next 90 minutes resulted in 13.7 moles of 99 mol% methanol.

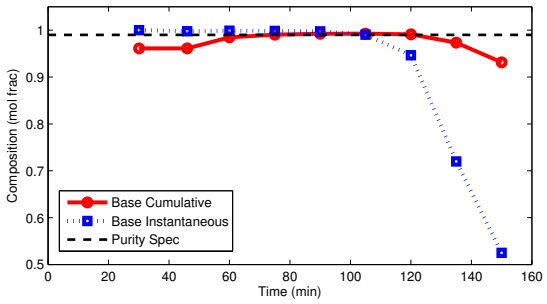

(a) Instantaneous and cumulative product mole fraction

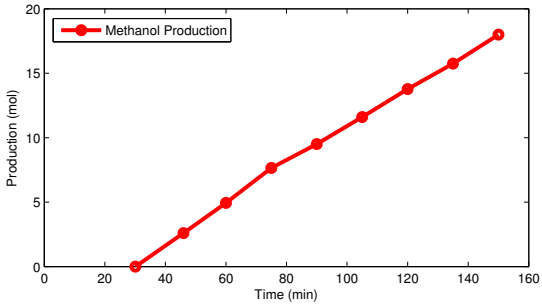

(b) Methanol production

Figure 3.3: Non-optimized base case where the final required purity ($>$ 99 mol% ethanol) is not met

3.2.2 Equations for the Simplified Process Model

Distillation is an inherently complex process involving mass and energy transfer, thermodynamics, and often reaction kinetics. Models that describe these phenomena do not have to be complex, however. The model developed here is used to describe the separation of a 50/50 wt% mixture of methanol and ethanol, and is simple by design to illustrate this point.

The VLE model used here is found in the CHEMCAD database [127] and is shown in Equation 3.3:

$$y_n^* = -2.016x_n^4 + 0.6861x_n^3 - 1.206x_n^2 + 1.721x_n + 0.0003984 \tag{3.3}$$

where x_n is the liquid mole fraction of methanol and y_n^* is the vapor mole fraction of methanol in equilibrium with the liquid. The subscript n denotes the stage for which the mole fraction is being calculated. The temperature difference across the column is not considered for the simplified model developed in this Section; however, the impact of temperature change throughout the column is considered in the model developed in Section 3.2.3. An adjustment to the equilibrium vapor mole fraction is used because equilibrium is not often achieved during column operation. This adjustment is in the form of a Murphree efficiency and is shown in Equation 3.4:

$$y_n = y_{n+1} - E_{MV}(y_{n+1} - y_n^*) \tag{3.4}$$

where y_n is the actual mole fraction and E_{MV} is the efficiency. The efficiency is a fitting parameter used to account for system non-idealities and is found using the data collected as part of this work.

The liquid mole fraction for each stage is found by performing a material balance at each stage, n, as shown by Equation 3.5 where V is the vapor flow through the column, L is the liquid return flow, and N_{tray} is the number of moles of liquid on the stage. The number of moles and the composition in the reboiler (N_{reb} and x_{reb}) change with time and are represented by Equations 3.6 - 3.7. The number of moles in the condenser (N_{cond}) is assumed constant while the composition of the condenser (x_{cond}) varies throughout the run (see Equation 3.8). Variation of the number of moles and composition of the product with time are represented by Equations 3.9 and 3.10. The liquid holdup for the condenser and trays are also design variables and are described in Equations 3.11 and 3.12, where f_{tray} and f_{cond} are the fitting parameters representing the fraction of the initial reboiler charge on each tray and in the condenser, respectively. The tray holdup is assumed constant across all stages. The stages are numbered from 1 to 40 with the top being 1 (condenser).

$$\frac{dx_n}{dt} = \frac{L(x_{n-1} - x_n) - V(y_n - y_{n+1})}{N_{tray}} \tag{3.5}$$

$$x_{reb}\frac{dN_{reb}}{dt} + N_{reb}\frac{dx_{reb}}{dt} = Lx_{39} - Vy_{reb} \tag{3.6}$$

$$\frac{dN_{reb}}{dt} = L - V \tag{3.7}$$

$$N_{cond}\frac{dx_{cond}}{dt} = V\ (y_2 - x_{cond}) \tag{3.8}$$

$$\frac{dn_p}{dt} = D \tag{3.9}$$

$$x_p\frac{dn_p}{dt} + n_p\frac{dx_p}{dt} = D\,x_{cond} \tag{3.10}$$

$$N_{cond} = N_{reb.init}\ f_{cond} \tag{3.11}$$

$$N_{tray} = N_{reb.init}\ f_{tray} \tag{3.12}$$

The vapor flow rate is found using the energy balance shown in Equation 3.13:

$$V = \frac{h_{dot}\ h_f}{H_{vap}} \tag{3.13}$$

where h_{dot} is the heat input from the heater, H_{vap} is the heat of vaporization for the methanol/ethanol system, and h_f is a fitting parameter representing the heating efficiency. The heat of vaporization is approximated as a weighted average of the pure component heats of vaporization obtained from the DIPPR Database [128]. The liquid flow rate, the reflux ratio, and the distillate rate are found using an overall mass balance and the definition of the reflux ratio, shown in Equations 3.14 and 3.15, respectively:

$$V = L + D \tag{3.14}$$

$$R = \frac{L}{D} \tag{3.15}$$

where R is the reflux ratio and D is the distillate rate. Constant molar overflow is assumed throughout the model and applies to the equations shown above.

3.2.3 Equations for the Detailed Process Model

A more detailed (although not completely from first-principles) model [129] with energy balance equations validates the simplified model developed in Section 3.2.2. A similar notation as the simplified model is used for the detailed model with a distinction in the stage number in which the material and energy balances are developed. Vapor and liquid leaving each stage are noted as V_n and L_n, respectively. The equations used in the detailed model are based on the following assumptions:

- constant molar hold up for the condenser and trays
- fast heat transfer throughout the column
- liquid temperature on each tray at the mixture bubble point

- vapor liquid equilibrium relationships based on temperature dependent vapor pressures
- pressure drop across each tray is 1 $mmHg = \Delta P$
- temperature dependent density, heat capacity, vapor pressure, and heat of vaporization

The overall and component mole balances as well as the energy balance equation for a control volume over the condenser and accumulator lead to Equations 3.16 to 3.19.

$$V_2 = L_1 + D \tag{3.16}$$

$$L_1 = R\,D \tag{3.17}$$

$$N_{cond}\frac{\mathrm{d}x_{cond}}{\mathrm{d}t} = V_2\,y_2 - (L_1 + D)\,x_{cond} \tag{3.18}$$

$$Q_{cond} = V_2\,h_{V_2} - (L_1 + D)\,h_{L_1} \tag{3.19}$$

A component and overall mole balance over the trays result in Equations 3.20 and 3.21. Equation 3.22 also represents an energy balance for each tray in the column.

$$N_{tray}\frac{\mathrm{d}x_n}{\mathrm{d}t} = L_{n-1}\,x_{n-1} - L_n\,x_n + V_{n+1}\,y_{n+1} - V_n\,y_n \tag{3.20}$$

$$0 = V_{n+1} - V_n + L_{n-1} - L_n \tag{3.21}$$

$$V_{n+1}\,(h_{V_{n+1}} - h_{L_n}) = V_n\,(h_{V_n} - h_{L_n}) - L_{n-1}\,(h_{L_{n-1}} - h_{L_n}) \tag{3.22}$$

A component mole balance and the associated energy balance equation for the reboiler are presented by Equations 3.24 and Equation 3.25. The reboiler heating rate, Q_{reb}, is 600 W to drive the separation together with the cooling of the condenser, Q_{cond}. The overall mole balance for this model is calculated from Equation 3.23.

$$\frac{dN_{reb}}{dt} = -D \tag{3.23}$$

$$x_{reb}\frac{\mathrm{d}N_{reb}}{dt} + N_{reb}\frac{\mathrm{d}x_{reb}}{dt} = L_{39}\,x_{39} - V_{40}\,y_{reb} \tag{3.24}$$

$$Q_{reb}\,h_f = V_{40}\,(h_{V_{40}} - h_{L_{40}}) - L_{39}\,(h_{L_{39}} - h_{L_{40}}) \tag{3.25}$$

Accumulation of product and the change in composition of the product with respect to changes in product moles are shown in Equations 3.9 and 3.10. The enthalpy of mixture for both liquid and gas phases is a mole average of the enthalpy of each component. Enthalpy of each component is obtained by integrating the heat capacity for liquid and adding the heat of vaporization for vapor. The temperature profile in the column is also a function of the equilibrium composition of each stage. The relationship between temperature and liquid composition of each stage is based on vapor pressure and the pressure on each tray (P_n) as shown in 3.26 with $n_s = 2$.

$$P_1 = 0.86\,atm\ (\text{Ambient Pressure in Provo, UT}) \tag{3.26a}$$

$$P_n = P_{n-1} - \Delta P \tag{3.26b}$$

$$P_n = \sum_{i=1}^{n_s} \gamma_i\,x_i\,P_i^{sat}\,(T_i) \tag{3.26c}$$

The vapor composition at each tray is determined by the vapor liquid equilibrium correlation shown in Equation 3.27 and is combined with the previous Equation 3.4 to relate the equilibrium composition (y_n^*) to the actual tray composition (y_n) based on the Murphree efficiency.

$$y_n^*\,P_n = \gamma\,x_n\,P_n^{sat}(T_n) \tag{3.27}$$

A full listing of the model equations, data, and Python source code is given in Appendix A. The more sophisticated model demonstrates that the simpler and less rigorous model is able to adequately predict the batch column performance for the purpose of optimization. The model validation is shown in the subsequent section.

3.2.4 Model Validation

Model validation is accomplished through dynamic parameter estimation. The parameter estimation experiment was similar to a doublet test, with reflux ratios set to 3.5, 1, 7 and 3.5. The column was allowed to come to steady state at infinite reflux before starting data collection; the reflux ratio was adjusted every 15 minutes thereafter. The parameters found by fitting the model with experimental data are heater efficiency $\left(h_f\right)$, vaporization efficiency (E_{MV}), condenser molar holdup as a fraction of initial reboiler charge (f_{cond}), and tray molar holdup as a fraction of initial reboiler charge (f_{tray}). The parameter best estimates are shown in Table 3.1.

Table 3.1: Confidence interval calculation for the four parameter case

Parameter	**Best Estimate**	**Upper 95% CI**	**Lower 95% CI**
h_f	0.719	0.799	0.639
E_{MV}	0.691	2.420	0
f_{cond}	0.029	0.254	0
f_{tray}	5.077e-4	0.142	0

The instantaneous distillate composition from the experimental run and the associated simplified and detailed model predictions using optimized parameters are shown in Figure (3.4a). The maximum error between the simplified model predictions and the experimental values is 10%. The maximum error between the more detailed model and experimental composition data is 4.8% for the ℓ_1-norm objective and 5.3% for the squared error objective. Cumulative methanol production is shown in Figure 3.4b. The error between model and prediction is almost non-existent using both an ℓ_1-norm or squared error objective. The simplified model parameter estimation has 3,510 equations with the squared error objective and 3,780 equations with the ℓ_1-norm objective and requires less than 10 CPU seconds to solve. The more detailed model parameter estimation has 11,644 equations with the squared error objective and 11,972 equations with the ℓ_1-norm objective and requires 89.4 (ℓ_1-norm) and 53.1 (squared error) CPU seconds to solve. All calculations are performed on a Intel Core i7-2760QM CPU operating at 2.4 GHz with the APOPT solver. Because the simplified model produces similar results to the detailed model and solves sufficiently fast for online real-time optimization, it is selected for the batch column optimization.

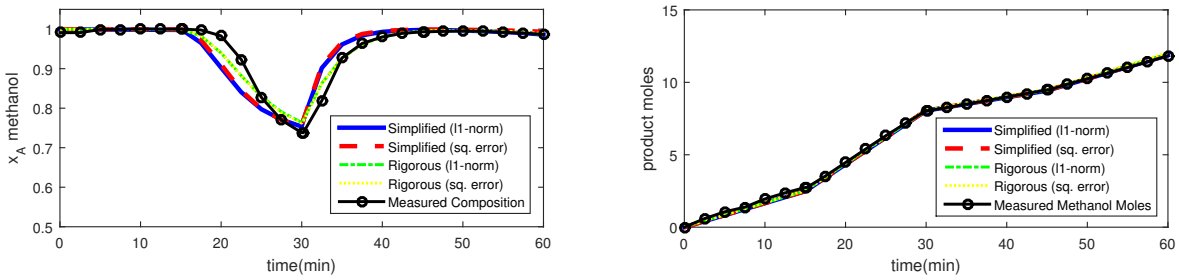

(a) Instantaneous distillate composition (b) Methanol production

Figure 3.4: Model validation for initial parameter estimation

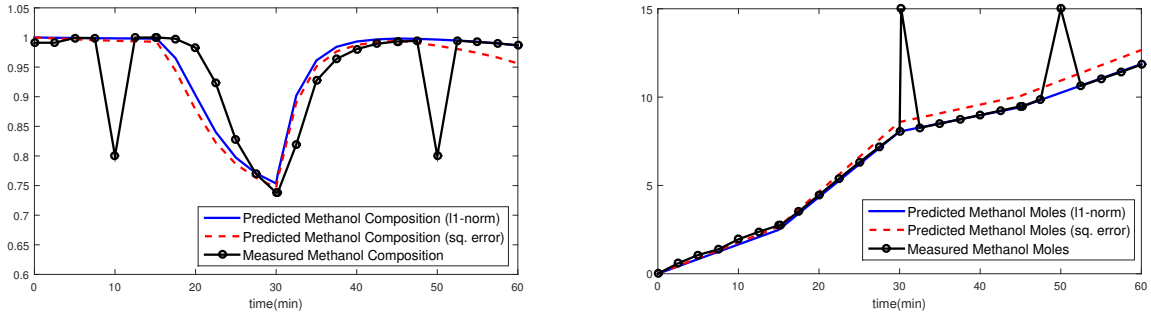

(a) Instantaneous distillate composition (b) Methanol production

Figure 3.5: Insensitivity of the ℓ_1-norm estimation to outliers compared to the squared error objective

If artificial outliers are introduced in both the composition (80 mol% ethanol at $t = 10\ min$ and $t = 50\ min$) and cumulative production (15 moles at $t = 30\ min$ and $t = 50\ min$), the squared error predictions deviate while the ℓ_1-norm estimates do not (see Figure 3.5). This is because the ℓ_1-norm is less sensitive to outliers and results in better predictions. In this comparison, the same model and initial values are used to represent the governing equations of the distillation column while the objective functions for error minimization differ, as described by [35]. While this particular example did not include significant outliers, many industrial applications of batch distillation may have instruments that report values with drift, noise, or outliers [130]. While gross error detection can resolve many of these data quality issues, it is also desirable to have estimation methods that are less sensitive to bad data as shown in this example.

3.2.5 Testing the Reliability of the Estimated Parameters

Nonlinear confidence intervals are calculated for four potential parameters. Confidence regions are typically reported as upper and lower limits on a particular parameter. This work extends the nonlinear confidence region to multivariate analysis that improve co-linearity assessment for batch distillation processes beyond a singular value decomposition or linear analysis. However, a look at the confidence interval for each individual parameter is useful to illustrate the procedure for model validation. A wide confidence interval suggests that there is insufficient structure in the model (observability) to determine the parameters from available measurements. Another insight that is gained from the confidence intervals is a test of the data diversity that leads to tight confidence regions. A tighter confidence region implies that a smaller deviation of the parameter from an optimal value is not statistically likely given a set of data to which the model is reconciled. Table 3.1 shows the expected value and 95% confidence interval for each parameter. As seen in the table, the interval for heater efficiency is narrow and in the range of values expected for a heater. The intervals for the other three parameters are large enough to include zero and the interval for vapor efficiency includes physically impossible values. Although the fit between model and data is excellent there are large parameter confidence intervals. One possible explanation for the large intervals is that the model is over-parameterized and thus has too many degrees of freedom. Thus, a sensitivity analysis is implemented to investigate the correct parameterization of the model.

The scaled sensitivity is shown graphically in Figure 3.6. The sensitivity is scaled by solution values as $\hat{S}_{i,j} = \left(\nabla_{\theta_j} x_i\right) \frac{\bar{\theta}_i}{\bar{x}_i}$ to show relative effects with a unitless transformation. The scaling is applied with parameters $\bar{\theta}$ and variables $\bar{x}$ at solution values. One clear result from this sensitivity study is that the total production (n_p) is dependent on the heat input to the batch column and that other parameters have little effect on the total production. As expected, a higher heating rate (h_f) vaporizes additional liquid and increases the flow to the condenser. With a specified reflux rate, the total production rate increases proportionally. In other words, a 1% increase in heating produces 1% additional product. This scaled sensitivity is shown as a value of 1.0 in the top subplot of Figure 3.6. The sensitivities of instantaneous product composition to the parameters are nearly co-linear as seen by the bottom subplot of Figure 3.6. For example, heater efficiency $\left(h_f\right)$ and tray holdup fraction $\left(f_{tray}\right)$ can be increased and decreased, respectively, to produce nearly the same final answer. Other parameters also show a high degree of co-linearity.

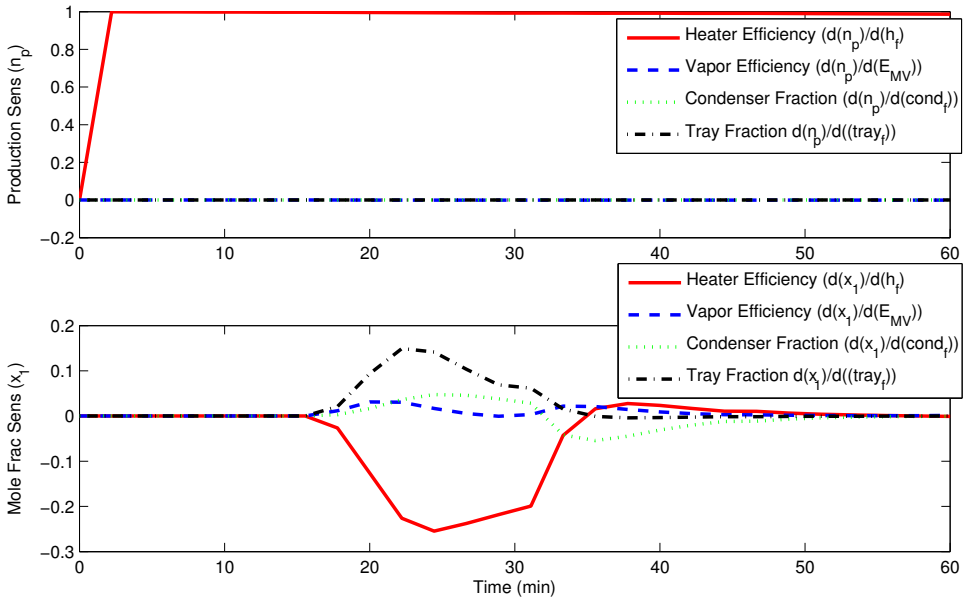

Figure 3.6: Scaled variable sensitivities to the parameters

While sensitivity plots such as Figure 3.6 are instructive, it can be difficult for large-scale systems to detect co-linearity or the number and selection of parameters that can be estimated from the data. An alternative way to show the same information is to decompose the sensitivity matrix with a singular value decomposition to reveal magnitudes of singular values (relative importance of transformed linear combinations of parameters) and eigenvectors (orthogonal vectors for the parameter space transformation). The singular value decomposition is applied to the dynamic sensitivity analysis to show that there is one principle parameter $\left(h_f\right)$ that can be used to match production data (n_p) as shown in Figure 3.7.

In this application, the parameter h_f is principally used to match n_p. For selecting a next parameter, f_{tray} or E_{MV} are feasible candidates with similar effect on the model. Estimating a third parameter is likely not needed as seen by the magnitude of the singular values. The singular value analysis gives a linear combination of the parameters estimated in transformed parameter space as given by the eigenvectors.

This analysis is useful even for the non-transformed parameter estimation where the parameter estimates have physical meaning and constraints are enforced to reflect physical realism. For example, in the case of h_f, a value greater than 1.0 is not likely because it represents the fraction

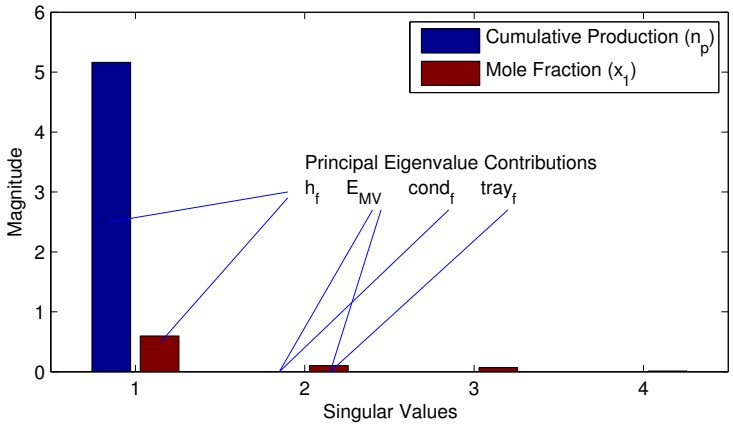

Figure 3.7: Magnitude of singular values from singular value decomposition reveals independent linear combinations of parameters to reconcile data

of reboiler heater duty that enters the liquid. It is expected that some of the heat escapes due to lack of insulation or conduction. In transformed space, the physical connection to the parameters is lost.

As mentioned, f_{tray} and E_{MV} have a similar effect on the model. In this study, E_{MV} is selected as the second parameter. It was therefore determined to first solve for all four parameters using ℓ_1-norm analysis, then fix both holdups and re-solve for the heater efficiency and the vaporization efficiency. The resulting confidence region and parameter best estimates are shown in Figure 3.8.

With only two parameters, the confidence regions are able to be graphically visualized. Instead of confidence intervals with lower and upper bounds, the 95% confidence region is given by any point within the area on the contour plot that falls within the boundary. Both the ℓ_1-norm and squared error objectives are included in this plot to demonstrate that slightly different optimal solutions and confidence regions are reported for differing objectives that align model and measured values. One notable issue is that the objective function is relatively insensitive to vapor efficiency (E_{MV}), especially as the vapor efficiency is above 0.4. The 95% confidence region suggests that values between 0.37 and 1.0 are valid parameter estimates for E_{MV} and that only one parameter is required for parameter estimation. The objective function is very sensitive to heater efficiency $\left(h_f\right)$ but not to E_{MV}. One possible explanation for this is that this is a high purity column where a difference of 0.01 in the mole fraction is of approximate equal importance to about 1.0

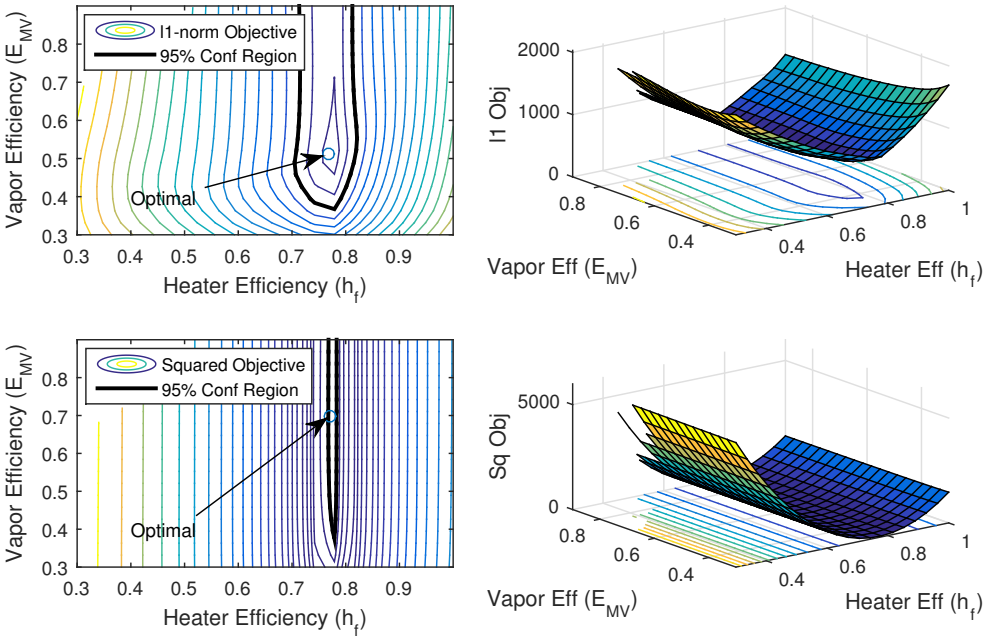

Figure 3.8: Contour and surface plots of the objective function value for values of heater efficiency (h_f) and vapor efficiency (E_{MV}). The 95% confidence interval for the ℓ_1-norm is not correct (future work) and the confidence interval for the squared error is an approximation.

mole of production. Although the objective is scaled to account for this discrepancy, parameters such as h_f greatly influence both the predicted moles produced and the product composition. The additional parameter E_{MV} is required to achieve an acceptable fit for product composition although it is less influential than the value of h_f. The objective function contours confirm the observations from the sensitivity analysis and singular value decomposition shown previously in Figures 3.6 and 3.7. The fit to the parameter estimation experiment is shown in Figures 3.9a and 3.9b. With the model sufficiently validated, the next step is to optimize the column control scheme.

3.2.6 Model Optimization and Validation

The objective in this case study is to maximize the amount of methanol produced in the column during a 90 minute run. The non-optimized base case production over a 90 minute run is 9.5 moles of 99.2 mol% methanol at a constant reflux ratio of 4 (see Section 3.2.1). The design variable in this study is reflux ratio, with the option to change the reflux ratio every 5 minutes. The control scheme for the optimized run is shown in Figure 3.10; the base case profile is shown

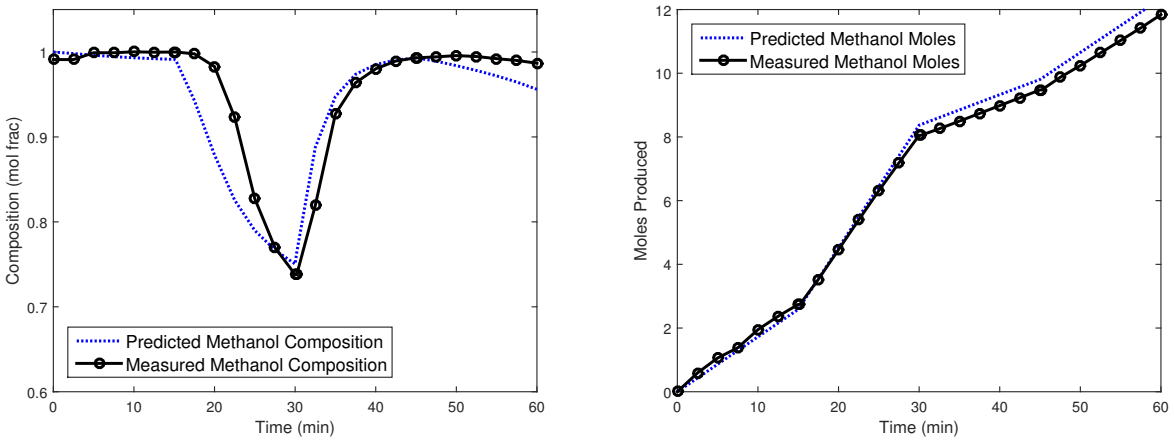

(a) Instantaneous distillate composition

(b) Methanol production

Figure 3.9: Model validation for final parameter estimates

for comparison purposes. The optimized reflux ratio scheme starts low before increasing in a nominally linear pattern. This is done to take advantage of the initially high concentration of methanol in the condenser after the startup period.

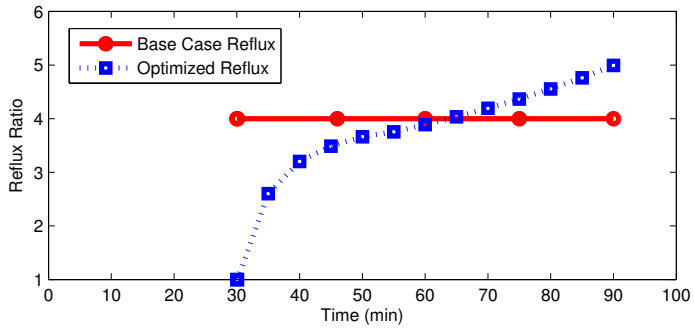

Figure 3.10: Reflux ratio for optimized control scheme compared to the non-optimized base case

The cumulative composition and total production are shown in Figure 3.11a and Figure 3.11b, respectively, with parameter values of $h_f = 0.8$, $E_{MV} = 0.37$, $f_{tray} = 0.0009$, and $f_{cond} = 0.006$. Also shown in the figures are the model predictions and the non-optimized base case results. The optimized control scheme resulted in 10.8 moles of 99.8 mol% methanol. This change represents a 14% increase in column production over the base case. Given the high concentration, it is possible to collect more product throughout the optimized run and still meet the purity

specification. However, given the error associated with experimental measurements, the prediction was left at a slightly conservative estimate to ensure the purity specification was achieved. The success of this effort is seen in the fact that the error bars on the optimized composition measurements stay above the purity requirement while those for the non-optimized base case do not.

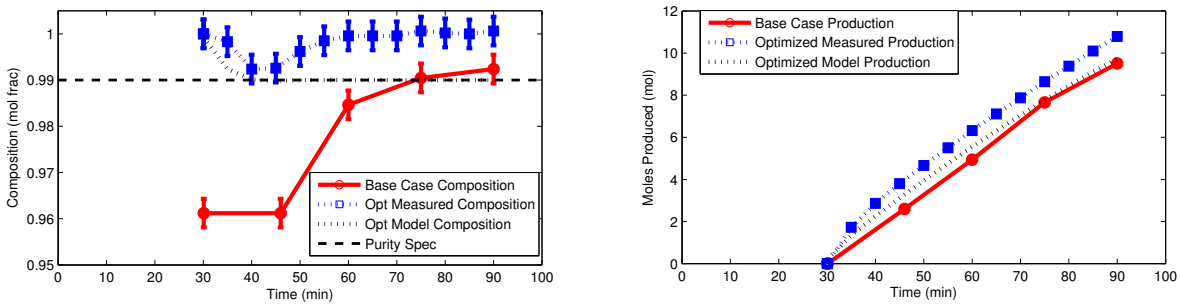

(a) Cumulative composition

(b) Methanol production

Figure 3.11: Optimized control scheme compared to the non-optimized base case and to the model prediction

Also seen in the figures are the model predictions. The model predicts 9.75 moles of 99.0 mol% methanol will be produced during the run. The difference between model prediction and experiment is 10% and 0.8% for overall production and product composition, respectively. The agreement between model and experiment is excellent and reflects the work done to validate the model.

3.3 Conclusions

Models of batch distillation are typically either first-principles and computationally expensive or simple and valid for ideal systems. In this work, a well-known methodology for parameter estimation, uncertainty quantification, and dynamic optimization is used to develop a simplified model for optimization of a batch distillation column. This methodology uses experimental data to solve for model fitting parameters and validates the results with nonlinear confidence intervals. This allows the models to include system non-idealities and be applicable for real-time analysis. This is accomplished using dynamic data with ℓ_1-norm error minimization. A dynamic sensitivity analysis reduces batch experimental data requirements by determining a priori which parameters

can be estimated. Nonlinear statistics are applied to quantify a posteriori the accuracy of those same parameters. The results from the simplified model also agree with a first-principles model but the simplified model solves 5-10 times faster than a first-principles model. While the methodology is not novel, the application to this specific case study with experimental data is demonstrated for the first time with insight into practical implications of working with real data.

The case study involves optimizing the control scheme for an existing batch column. A 38 tray, 2 inch, vacuum-jacketed and silvered Oldershaw batch distillation column was used to collect experimental data. One experiment was performed to collect data for model validation and another experiment was performed to validate the optimized control scheme. The optimized control scheme resulted in a 14% production increase over the base case while still meeting the purity requirements. The model predictions for the optimized run are within 10% of the experimental data.

CHAPTER 4. HYBRID SYSTEM OF CRYOGENIC CARBON CAPTURE AND POWER GENERATION UNITS

4.1 Introduction

Electricity transmission is one of the main forms of energy delivery today. According to the International Energy Agency (IEA) [131], electricity transmits roughly 33% of the total energy worldwide. Over eighty percent of this electricity is generated from non-renewable sources [132]. This makes the power sector one of the main sources of CO_2 emission. The International Energy Agency (IEA) estimated 42% of the 2012 global CO_2 emissions are derived from power and heat production [133]. There is nearly universal agreement among climatologists that anthropomorphic CO_2 and other greenhouse gases are the main causes of global warming [134]. The US and other developed nations have reduced CO_2 emissions in recent years through a combination of events, including a global recession, transformation from coal to natural gas in new power generation systems, increased automobile efficiency, and decreased miles driven [134, 135]. Furthermore, interest in renewable energy sources like solar and wind power continues to increase which further helps reduce the CO_2 emissions. However, many renewable energy supplies are intermittent and have capacity factors that are small compared to thermal power generation units. Therefore, because a one megawatt (MW) wind or solar power unit cannot replace a 1 MW thermal power unit, wind or solar power units must be integrated with thermal power units to develop a reliable power generation system.

There is a wide body of research on integrated power generation systems that include both thermal and renewable power plants. Goransson et al. [136] presented a model to investigate the effect of large-scale wind and thermal power integration. The purpose of the study was to investigate the impact of wind power generation on the production strategies of thermal power production systems. They also considered the startup and turn down performance of the thermal units. However, spinning reserves must often be on standby due to the limited rate of startup and the possibility

of decrease from an intermittent supply. Delarue et al. [137] studied the impact of wind power generation on the cost associated with electricity generation, fuel, and CO_2 emission. They considered the unpredictability of wind speed forecast and proposed a wind forecasting method. The power plant was scheduled over a 24 hour horizon with forecasted wind power data to meet the demand with minimal cost. Hu et al. [138] developed a Solar Aided Power Generation (SAPG) system, using the traditional Rankine power cycle and solar heating. They concluded that SAPG is more efficient than both the solar thermal power systems and the conventional fuel-fired power cycles. Manenti et al. [139] developed a dynamic model for solar power plants with storage. The dynamic simulation optimized power generation and improved the net income of a concentrating solar power plant. This optimization considered the market demand in real-time, storing superfluous energy, and using the stored energy when necessary. Powell et al. [140, 141] considered a solar thermal power plant integrated with a two-tank-direct thermal energy storage system. They found that the energy storage system led to a 64% increase in utilization of solar power with intermittent supply. Onar et al. [142] studied the combination of wind, fuel cell, and ultra-capacitor systems for energy production. The fuel cell and ultra-capacitor systems worked as a backup for the variations in wind turbine power output to keep a reliable power production system. In the investigation, wind power was the main source of energy. It also powered an electrolyzer that produced hydrogen for the fuel cell during peak hours. In peak hours, when wind power was insufficient, the fuel cell and ultra-capacitor systems provided the required additional power.

Despite the increased contribution of renewable power sources in reducing the CO_2 emissions from power plants, the global trend of CO_2 emissions is still increasing. Consequently, more restrictive regulations for CO_2 emissions have been enforced or are under consideration [143–145] to control the CO_2 emissions. For instance, the US Environmental Protection Agency (EPA) recently promulgated regulations under Clean Air Act Sections 111(b) and 111(d) for the CO_2 emissions from the US power industry. Existing natural gas and coal–fired power plants can emit up to 1100 and 1400 lbs of CO_2 per MWh energy generation. New power plants must reduce CO_2 emissions by 20% from 2014 levels [143]. Current combined–cycle natural gas plants meet these standards and they are about 30% below the emissions of most coal plants. Such large reductions from coal plants lie well beyond the reach of plant efficiency improvements or other modest operational changes and threaten decommissioning of existing plants and curtailing plans for new

plants. In fact, coal consumption has declined in the US for many years and there are very few new coal plants planned. These declines, however, stem from low–cost natural gas competition and not from CO_2 emissions controls. Low–cost natural gas is a recent develoment in the US but is not a global shift in the energy landscape. Globally, coal is by far the most rapidly growing source of primary energy [134]. Coal will continue to play a major role in power generation in the US, even by EPA projections, and shows every sign of continuing a rapidly increasing role in power globally. Global CO_2 emissions must decrease by 60-80% to limit global climate change to a 2 °C increase [146]. This is about twice as much as the total CO_2 emissions from all forms of power generation. Therefore, global climate change critically depends on finding ways to reduce CO_2 emissions from fossil power plants generally and from coal specifically. In this sense, fossil– and specifically coal–based emissions reduction represents one of the most important elements of climate change mitigation. No national or global climate change policy can likely succeed without addressing this issue.

Carbon capture and storage (CCS) is a viable approach to achieve the target CO_2 emission level. The literature for CO_2 removal mainly considers three typical CCS technologies: post combustion, pre-combustion, and oxyfuel [134]. Cryogenic technologies have also been considered for carbon dioxide removal and they have several forms such as an inertial carbon extraction system, a thermal swing process, and cryogenic carbon capture with an external cooling loop (CCCECL) [147–150]. Many state of the art technologies for CO_2 mitigation processes are energy intensive. Thus, it is critically important to study the impact of CO_2 capture processes on power generation systems.

Kang et al. [151] studied an integrated system of energy production consisting of a coal plant, a wind power facility, and a temperature-swing CO_2 capture unit [151]. A natural gas combustion turbine and heat recovery steam generator supplied heat for CO_2 capture. The turbine also supplied supplemental electricity when required. The study also considered demand response in the form of storing CO_2-rich amine solution during peak demand. They concluded that with an optimized operation, 20% more profit is obtained compared to a heuristic procedure. Belaissaoui et al. [152] explored the CO_2 capture challenges for a gas turbine plant. The low concentration of CO_2 in a gas turbine power plant led them to consider membrane separation for CO_2 capture. It was found that the overall energy requirement is less than 205 kWh/ton CO_2 with a highly selective

membrane. Chalmers et al. [153] studied the flexibility added to power plants retrofitted with CO_2 capture by operating under different scenarios. They considered a post-combustion capture process. The goal of investigation was to maximize profit by choosing the operation pattern in response to electricity market prices. The scenarios that are considered are: (1) power plant shut down; (2) using a CO_2 capture system; and (3) bypassing the CO_2 capture system. Cohen et al. [154–156] considered the flexible operation of a CO_2 capture unit integrated with a fossil-fueled power plant. They used an amine-based CO_2 capture process with the objective of maximizing the profit of the hybrid system in response to electricity price volatility (incorporating spikes in the power price). In comparison to a similar system without the spikes in power price [157], flexible operation of the CO_2 removal created higher operating profit. They also evaluated the profitability of two flexible configurations for the operation of CO_2 removal system under three 20-year CO_2 price paths and compared them with the operation of inflexible CO_2 removal. Chalmers et al. [158] studied the impacts of post-combustion capture on transient performance of coal-fired power plants. They also differentiated between plants with CO_2 capture and without CO_2 capture in the load-following capability, and recommended considering some constraints to power plant start-up due to the post-combustion capture. Gerbelov et al. [159] explored the performance, cost impacts, and feasibility of retrofitting an amine based post-combustion capture method for existing power plants. Two sub-critical coal power plants and two natural gas combined cycle plants were considered in the investigation. Net plant efficiency loss of the coal-fired and gas-fired power plants were found to be 12% and 8%, respectively, based on the higher heating value (HHV). The capital cost of both natural gas-fired and coal-fired power plants was explored and it was found that natural gas-fired power plants require less capital costs because of lower CO_2 concentrations in the flue gas. The investigation also examined the effect of fuel price on the breakeven point (the point at which the cost of electricity is equal for plants with and without Carbon Capture and Storage (CCS) at a set price of CO_2 emission).

Cormos et al. [160] assessed the techno-economic and environmental aspects of power generation for an Integrated Gasification Combined Cycle (IGCC) power plant with and without CCS. A pre-combustion method using gas-liquid absorption in physical solvents (Selexol) was used for carbon capture. The study investigated IGCC with CCS from different aspects, including plant capital cost, operational and maintenance cost, Levelized Cost of Electricity (LCOE), and

CO_2 capture. Cormos et al. [161] explored integration of CCS with both Pulverized Coal (PC) power plants and IGCC plants. A post-combustion carbon capture method was used for PC plants; however, for IGCC power plants, a pre-combustion method was used. It was found that energy penalty for introduction of CCS, on the net energy percentage basis, is 8-9 % for PC power plants and about 7 % for IGCC plants.

Some studies also considered using renewable energy sources to provide the energy requirement of CO_2 capture process or to efficiently utilize CO_2 produced from power plants to adopt more renewable energy. Khorshidi et al. [162] explored using auxiliary units fueled by biomass to compensate for the energy loss of the CO_2 capture process. They considered a combined heat and power (CHP) production unit that used biomass as the fuel and found that a CO_2 price of at least \$55/tonne CO_2 or a biomass price of less than 1 \$/Gj is required to cost-effectively capture CO_2 from both the coal plant and auxiliary biomass CHP unit. Mohan et al. [163] considered an integrated system of an IGCC power plant and an enhanced geothermal system (EGS). The purpose of the study was to extract geothermal heat by using CO_2 produced from an IGCC plant as the heat transfer fluid. In addition to the power produced from geothermal energy in an organic Rankine cycle (OCR), power was also produced by expansion of CO_2 in a high pressure turbine before being re-injected to the reservoir. For a sample case, it was shown that such a hybrid system was able to recover 74% of the energy consumption of the carbon capture and sequestration.

Although various methods have been developed for CO_2 capture, the major drawback of most of CO_2 removal systems is the parasitic energy load. Jensen et al. [150] stated that the average energy consumption of using oxy-combustion, absorbents, adsorbents, or membranes for CO_2 removal is 1.69, 1.72, 3.39, and 1.3 MJ_e/kg CO_2, respectively. As mentioned previously, the cryogenic carbon capture (CCC) process [164] is another technology for CO_2 removal and is less energy intensive compared to the aforementioned capture systems (an average of 0.7 MJ_e/kg CO_2). This process has some configurations that store energy in the form of liquefied natural gas (LNG). This capability manages the energy loss of CO_2 removal by using stored refrigerant to drive the process during peak demand, transferring the reduced parasitic load to the grid to help meet the demand, and regenerating the refrigerant during low-demand periods. In addition, the rapid-load-change capability of the CCC enables conventional power generation systems to integrate more easily with renewable intermittent power sources [164]. As renewable energy sources become

a larger portion of the energy market, fossil-fueled generators that were originally designed for baseline power production have to operate on a load-following basis, which results in increased emissions and operational costs [165]. Thus, by adopting more renewable energy sources into the power grid, the significance of rapidly responding to large fluctuations with energy storage becomes critical to maintaining a reliable and cost-effective electric grid.

This investigation considers the grid-level responses of CCC-equipped systems. Most of the research on integrated systems of power generation and carbon mitigation have only considered steady-state simulations. With steady-state simulation, the transient behavior of the intermittent power sources and energy storage are neglected; however, with transient optimization, time-shifting of the parasitic load of the carbon mitigation process can be considered, which can help reduce the operating cost. Thus, the dynamic optimization of an integrated system including conventional and renewable power plants with and without energy storage versions of the CCC process is considered in this investigation. Two types of fossil–fueled power generation units are considered in this dissertation: (1) load–following unit, and (2) baseline unit.

This chapter includes three sections; the first section provides an overview of the CCC process. The next section presents the hybrid power generation system and the non-energy-storing version of the CCC process. The final section discusses the simulation results for a simplified hybrid system without energy storage. The simulations of a hybrid system with energy storage are the focus of Chapters 5 and 6.

4.2 Non-energy-storing Version of the Cryogenic Carbon Capture (CCC)

The CCC process is a retrofit, post–combustion technology that captures CO_2 in the flue gas through desublimation; i.e. the CCC process cools flue gas from power generation units to the point that CO_2 desublimates. Other pollutants in the flue gas, such as mercury and hydrogen sulfide, are also separated in the cooling process. The resulting solid is separated from the remaining light gases. Solid CO_2 is then melted, pressurized, and transported to underground containment wells [147]. Two refrigeration cycles are used to accomplish the cooling in the CCC process (Figure 4.1). The first refrigeration cycle (internal refrigeration loop in Figure 4.1) uses CF_4. The electricity demand associated with running this refrigeration cycle and other auxiliary equipment in the CCC process is referred to as CCC plant electricity demand. The second refrigeration

cycle (external refrigeration loop in Figure 4.1) uses liquefied natural gas (LNG), although other refrigerants could be selected. The electricity demand associated to run the external refrigeration cycle in the LNG production process is referred to as the LNG plant electricity demand. The advantage of using LNG in the CCC process is that when it passes through the CCC process (stream 3 in Figure 4.1), it is vaporized so that heat is removed from the process. The vaporized LNG (stream 4 in Figure 4.1) is then warmed up to higher temperatures in the LNG/mixed refrigerant recuperator. The warm natural gas (stream 5 in Figure 4.1) can then be combusted to produce power. Thus, the refrigerant is also the fuel which significantly reduces the operational costs of the plant. However, only a fraction of the vaporized LNG is allowed for combustion so that oversizing of the gas turbine is avoided. The decisions about the magnitude of power production from natural gas and the time that gas power should be produced are made by the optimizer. Because a fraction of the natural gas is burned in the gas turbine, natural gas is imported to the plant (stream 1 in Figure 4.1) so that enough LNG is available for treating the flue gas in the CCC process.

Although the CCC process is able to integrate with both gas- and coal-fired power plants independently, in this investigation it is assumed that the combination of them establishes a single power generation unit and the lumped unit is equipped with the CCC process. Thus, the feed to the CCC process has two sources: (1) flue gas from burning the coal for steam production (2) flue gas from burning the natural gas in the gas turbine. A more in-depth analysis of CCC can be found at [147–149, 164]

4.3 Modeling Framework for the Non-energy-storing Hybrid System

4.3.1 Model Equations

This section presents the model developed for the hybrid system of the power generation unit and the CCC capture process. First, relationships for power generation from each source are developed and are all presented in the unit of MW. The power production in the coal-fired steam boiler (P^{ST}) is calculated from a first order differential equation (Equation (4.1)) that relates the power output (P^{ST}) to the set point of the power output (P^{SP}). This relation represents the transient response of steam boilers when a change in the power output is required. The set point of the steam boiler power output (P^{SP}) is a decision variable and is optimized based on the economical

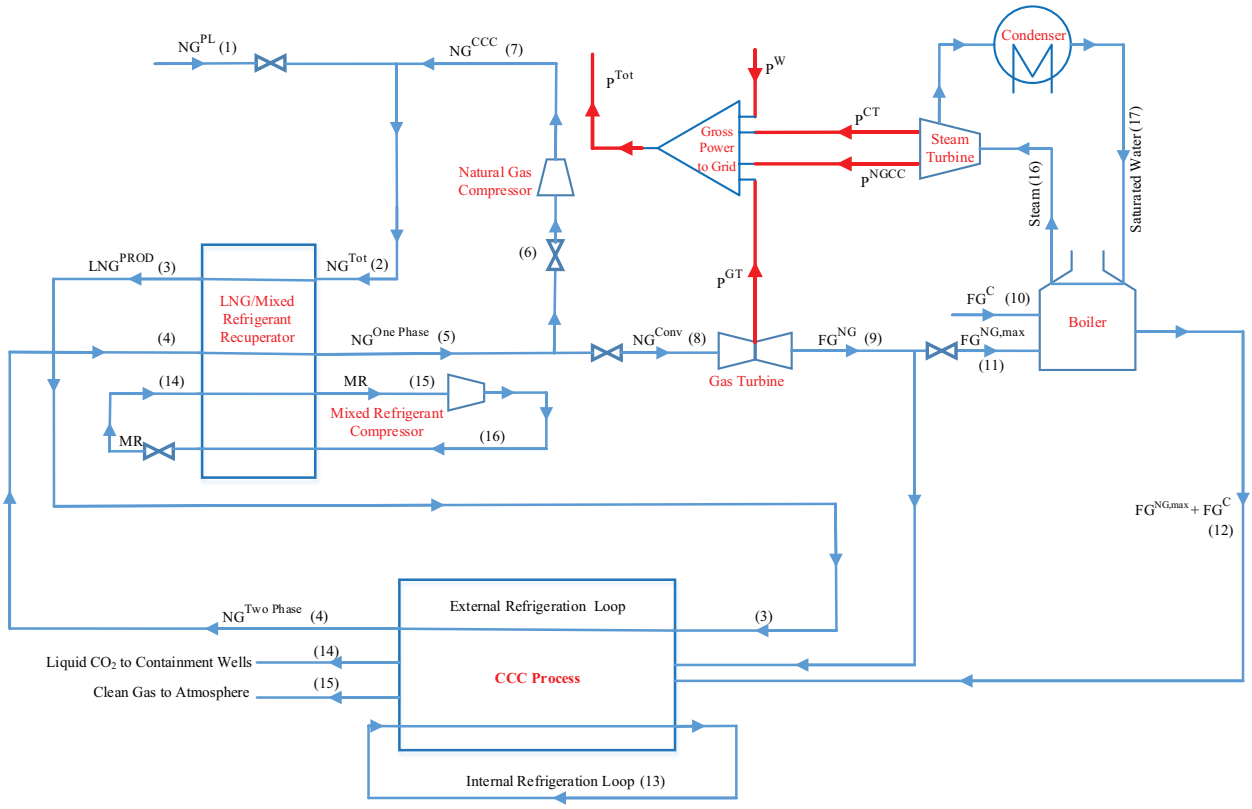

Figure 4.1: Schematic configuration of the integrated system of power generation unit and the CCC process without energy storage

evaluation of the hybrid system. The range of variation of P^{SP} is considered between the nominal capacity of the steam boiler and and 44% of this capacity. When integrating the CCC capture process with existing power generation units, this range should be modified according to the capacity of the steam turbine.

$$\tau^{ST}\frac{dP^{ST}}{dt} = -P^{ST} + K^{ST}P^{SP} \tag{4.1}$$

In this case, τ^{ST} and K^{ST} are the time constant and gain, respectively, for power production in the steam boiler. The time constant represents the time it takes to reach 63.2% of the total change in steam boiler power output when there is a change in the set point. Gain is the ratio of total change in the power output from the steam boiler and the magnitude of change in the set point. An assumed value of 2 hours for the time constant represents the slow response of the steam boilers to changes in set points in practice. A gain value of 1 is used in Equation (4.1) for the steam boiler. It should be noted that reference to the power production in a steam boiler (P^{ST}), in

this investigation, is in fact the result of producing power in a turbine that is driven by the steam generated in the boiler. Steam is generated from the heat content of the flue gas produced from coal combustion (simple cycle). Exiting flue gas from a gas turbine can also be introduced to the boiler to produce more steam and achieve the efficiency of a combined cycle. Thus, total power output from the steam turbine (P^{ST}) in the combined cycle is the summation of equivalent power from exchanging heat by the flue gas generated from coal and natural gas combustion (Equation (4.2)).

$$P^{ST} = P^{CT} + P^{NGCC} \tag{4.2}$$

P^{CT} and P^{NGCC} are the power generated from the coal and natural gas flue gases, respectively. P^{NGCC} is dependent on the rate of natural gas combusted in the gas turbine, NG^{Conv}, (or equivalently on the gas power production, P^{GT}) and is defined in (4.4). Either P^{CT} or P^{GT} can be selected as the second decision variable and the other variable (as well as P^{NGCC}) is calculated from solving Equations (4.2) and (4.4) simultaneously. Similarly, mass flow rates of combusted coal (C) and natural gas (NG^{Conv}) can be selected as the second decision variable. In this investigation, flow rate of the natural gas combusted in the gas turbine is selected as the second decision variable. Power generated in the gas turbine, P^{GT}, is then calculated from Equation (4.3):

$$P^{GT} = NG^{Conv}\varepsilon_g \Delta H_g \tag{4.3}$$

where ε_g, ΔH_g are the efficiency of power production in the gas turbine and enthalpy of combustion of natural gas, respectively. The values assumed for these two parameters are 0.3275 and 53.89 MJ/kg, respectively [166]. It should be noted that all equations involving flow rates are presented on a mass basis with units of kg/hr.

Power production from the steam generated from the natural gas combined cycle is obtained from Equation (4.4). In deriving this equation, it is assumed that the heat transfer from the flue gas to the boiler feedwater has an efficiency of 88% (ε^{SB}). It is also assumed that the steam turbine is 41.6% efficient (η^{ST}). Ratio of the mass flow rates of the flue gas to natural gas combusted in the gas turbine is presumed to be 42.56 kg/hr (Equation (4.5)). These assumptions are based on the simulation studies for a NGCC power plant with a single reheat 16.5 MPa/566 °C/566 °C cycle

and an overall combined cycle efficiency of 50.2% [166]. Thus, the overall power production in the steam turbine is the product of specific enthalpy change of the flue gas (ΔH_{FG}^{NG}), mass flow rate of the flue gas produced from natural gas combustion (FG^{NG}), efficiency of the heat exchange in the boiler (ε^{SB}), and efficiency of the steam turbine (η^{ST}):

$$P^{NGCC} = \Delta H_{FG}^{NG} FG^{NG} \varepsilon^{SB} \eta^{ST} \tag{4.4}$$

$$NG^{Conv} = \frac{FG^{NG}}{42.56} \tag{4.5}$$

As mentioned previously, solving Equations (4.2) and (4.4) simultaneously returns the value of P^{CT}. An equation similar to Equation (4.4) is then used to calculate the mass flow rate of the flue gas from the combustion of coal (Equation (4.6)):

$$FG^{C} = \frac{P^{CT}}{\varepsilon^{SB} \eta^{ST} \Delta H_{FG}^{C}} \tag{4.6}$$

In this case, FG^{C} and ΔH_{FG}^{C} are the mass flow rate of the flue gas from coal combustion and specific enthalpy change of the flue gas, respectively. It is also assumed that 10.93 kg/hr flue gas is produced from the combustion of 1 kg/hr of coal (Equation (4.7)).

$$C = \frac{FG^{C}}{10.93} \tag{4.7}$$

All these assumptions are based on the simulated results from [166] for a subcritical pulverized coal power plant that uses a single reheat 16.5 MPa/566 °C/566 °C cycle and has an overall plant efficiency of 36.8%. Table 4.1 summarizes most of the data used in this investigation.

Although flue gas produced in the gas turbine can be completely directed to the boiler, it is assumed that only a fraction of it is used for excess steam generation in the boiler. This constraint addresses the limitation of the steam boilers in utilization of the flue gas in a combined cycle. The flow rate of the flue gas directed to the steam boiler is limited to a flow rate that can potentially produce sufficient steam to generate power up to 20% of the assumed upper bound for the steam turbine capacity and is calculated from Equations (4.8) and (4.9). It should be noted that the

Table 4.1: Summary of the input parameters

Parameter	Value
Thermal efficiency of boiler, ε^{SB}	0.88
Efficiency of the steam turbine, η^{ST}	0.416
Specific enthalpy change of the flue gas from coal combustion, ΔH_{FG}^{C}, (MJ/kg)	2.335
Efficiency of the gas turbine, ε_g	0.3275
Enthalpy of combustion of natural gas (HHV), ΔH_g (MJ/kg)	53.89
Specific enthalpy change of the flue gas from natural gas combustion, ΔH_{FG}^{NG} (MJ/kg)	0.587
Overall efficiency of coal–fired power plant	36.8%
Overall efficiency of the NGCC power plant	50.2%
Work of compression for natural gas compressor (kWh/(kg inlet)) or (GJ/tonne CO_2)	0.051 (0.1656)
Work of compression for mixed refrigerant compressor (kWh/(kg inlet)) or (GJ/tonne CO_2)	0.077 (0.1818)
Electricity demand of the CCC for treatment of the flue gas (coal combustion)(GJ/(tonne CO_2 captured))	0.389
Electricity demand of the CCC for treatment of the flue gas (gas combustion)(GJ/(tonne CO_2 captured))	0.428
LNG demand to process the coal flue gas (kg/(tonne CO_2 captured))	856
LNG demand to process the gas flue gas (kg/(tonne CO_2 captured))	685

numerator of Equation (4.8) is normalized with the capacity of the gas turbine to keep the units of both sides on a mass basis.

$$NG^{Conv,max} = \frac{GP_{max}^{CC}}{GT^{cap}} NG^{Conv} \tag{4.8}$$

$$FG^{NG,max} = 42.56 NG^{Conv,max} \tag{4.9}$$

Table 4.2: Coal properties

Component	Weight percentage
Carbon	48.18
Hydrogen	3.310
Oxygen	11.87
Chlorine	0.01
Sulfur	0.37
Nitrogen	0.7
Ash	5.32
Moisture	30.24

$NG^{Conv,max}$ represents the maximum flow rate of combusted natural gas, of which the corresponding produced flue gas ,$FG^{NG,max}$, is directed to the steam boiler. The maximum permitted power production in the combined cycle and the capacity of the gas turbine are represented by GP^{CC}_{max}, GT^{cap}, respectively.

Next, electricity demand of the CCC and LNG production facilities and the LNG requirement to treat the flue gas are calculated. While the power production from natural gas in a combined cycle is limited, all the flue gas produced in the gas turbine should be treated in the CCC process. Thus, total electricity demand of the CCC process and the required LNG to treat the flue gas resulting from the combustion of natural gas are based on NG^{Conv} and is calculated from the rearrangement of Equation (4.5). It is assumed that the treatment of hot flue gas from the gas turbine and the cold flue gas from the steam boiler requires the same amount of electricity and LNG. According to [36], treatment of the flue gas produced from coal and natural gas combustion requires 0.389 and 0.428 GJ per tonne of captured CO_2, respectively. Adopting the combustion reaction mechanisms used by [151] for a subbituminous Wyoming Powder River Basin coal and natural gas with the compositions given in Tables 4.2 and 4.3 [167] results in 851.23 and 545.47 kg/hr CO_2 production from one MW power generation from coal and natural gas, respectively. With a 90% capture rate, the electricity demands of the CCC process for treatment of the flue gases generated from coal and natural gas combustion are 0.083 and 0.058 MW per one MW generated power from each source, respectively. The overall electricity demand for the CCC facility is then calculated from Equation (4.10):

$$D^{CCC} = 0.083P^{CT} + 0.058P^{NGCC} \tag{4.10}$$

Table 4.3: Natural gas properties

Component	Mole percentage
Methane	83.4
Ethane	15.8
Nitrogen	0.8

According to [36], required LNG to process the flue gases from coal and natural gas combustion are 856 and 685 kg per tonne CO_2 captured. Similar to the calculation of the CCC electricity demand, LNG demand for treatment of the flue gas from combustion of coal and natural gas are 656.2 and 336.4 kg/hr per one MW generated power from each source, respectively. Thus, the overall LNG demand is calculated from Equation (4.11):

$$LNG^{R} = 656.2P^{CT} + 336.4P^{NGCC} \tag{4.11}$$

The work of compression of the natural gas ($D^{NG,Comp}$) and mixed refrigerant ($D^{MR,Comp}$) compressors are 0.051 and 0.077 kW per kg/hr of the inlet streams, respectively [36]. After unit conversion, these lead to the following equations:

$$D^{NG,Comp} = 5.1 \times 10^{-4} NG^{CCC} \tag{4.12}$$

$$D^{MR,Comp} = 7.7 \times 10^{-5} MR \tag{4.13}$$

In this case, NG^{CCC} and MR are the mass flow rates of natural gas coming from the CCC process and mixed refrigerant, respectively. Total electricity demand of the LNG production facility, D^{LNG}, is the summation of $D^{NG,Comp}$ and $D^{MR,Comp}$ (Equation (4.14)).

$$D^{LNG} = D^{NG,Comp} + D^{MR,Comp} \tag{4.14}$$

Total electricity demand from the CCC and LNG production facilities, D^{plant}, is then calculated by adding up the individual components (Equation (4.15)):

$$D^{plant} = D^{CCC} + D^{LNG} \tag{4.15}$$

Total electricity demand is a summation of the CCC and LNG plants, D^{plant} and residential area, D^{Res}, presented by Equation (4.16). Residential electricity demand assumed in this investigation is an input to the optimization problem.

$$D^{Tot} = D^{plant} + D^{Res} \tag{4.16}$$

The overall power generation is also calculated from Equation (4.17):

$$P^{Tot} = P^{CT} + P^{GT} + P^{NGCC} + P^{W} \tag{4.17}$$

The variable P^{W} represents the power generated from the wind and is considered an input to the model.

Next, mass and energy balance equations used in this investigation are presented. The amount of the LNG that is produced in the recuperator is the sum of the natural gas imported from the pipeline and natural gas that comes from the CCC plant. Thus, total LNG production (also equals the value of NG^{Tot} shown in Figure 4.1 on a mass basis) is calculated from Equation (4.18):

$$LNG^{Prod} = NG^{PL} + NG^{CCC} \tag{4.18}$$

Deriving all equations on a mass basis also results in the equality of $NG^{Twophase}$, $NG^{Onephase}$, and LNG^{R}. This conclusion is used in deriving a relationship between NG^{CCC}, LNG^{R}, and NG^{Conv}. As a result, it is obvious from Figure 4.1 that natural gas from the CCC plant, NG^{CCC}, equals the difference between mass flow rates of the LNG requirement, LNG^{R}, and natural gas combusted in the gas turbine ,NG^{Conv}:

$$NG^{CCC} = NG^{Onephase} - NG^{Conv} \tag{4.19}$$

When there is no energy storage, LNG production also equals the mass flow rate of LNG requirement (Equation (4.20)):

$$LNG^{Prod} = LNG^{R} \tag{4.20}$$

While combustion of the natural gas in the gas turbine is approximately instantaneous, an equation similar to Equation (4.1) is considered for the natural gas imported to the plant (Equation (4.21)). This equation represents the dynamic response of the system to changes in set point of imported natural gas.

$$\tau^{NG}\frac{dNG^{PL}}{dt} = -NG^{PL} + K^{NG}NG^{PL,SP} \tag{4.21}$$

where $NG^{PL,SP}$ is the set point of the natural gas imported from the pipeline and is a decision variable. Time constant and gain of the first order model used in this equation are represented by τ^{NG} and K^{NG}, respectively. A time constant of 5 minutes and a gain value of 1 are assumed for the import of natural gas.

An energy balance over the recuperator defines the relationship between the natural gas imported (NG^{PL}) and recirculated in the system (NG^{CCC}). It also defines the trend of variation of mass flow rate for the mixed refrigerant (MR). Total energy gain from the cold streams entering the recuperator is obtained from Equation (4.22):

$$Q^{g} = NG^{Twophase}\Delta H^{1} + MR\Delta H^{2} \tag{4.22}$$

where ΔH^{1} is the enthalpy difference of the two phase gas stream exiting the CCC plant and warm natural gas after the recuperator and is equal to 299 kJ/kg. ΔH^{2} is also the enthalpy difference of the cold mixed refrigerant entering the recuperator and is equal to 620 kJ/kg.

Total energy loss from the hot streams entering the recuperator is also obtained from Equation (4.23):

$$Q^{L} = NG^{Tot}\Delta H^{3} + MR\Delta H^{4} \tag{4.23}$$

where ΔH^{3} is the enthalpy difference between the warm natural gas that is liquefied and the LNG produced in the plant and is equal to -582 kJ/kg. ΔH^{4} is also the enthalpy difference of the hot mixed refrigerant entering the recuperator and is equal to -9 kJ/kg.

The values assumed for ΔH^{1}, ΔH^{2}, ΔH^{3}, and ΔH^{4} are based on the results obtained at [147] with the assumption that temperature and pressure of the entering and exiting streams to and from the recuperator are constant. Results presented in [168, 169] propose a design for a plate heat

exchanger that the temperature and pressure remain constant despite the fluctuations in inlet and outlet conditions of the heat exchanger. These fluctuations occur because of the process transients introduced by energy storage and specifically by large swings in LNG production rates in response to the variations in electricity demand and wind power. The proposed design is able to minimize the transient impacts of energy storage and LNG production on the operating conditions of the heat exchanger. Thus, the recuperator considered in this study has a steady–state performance and is very responsive to fluctuations in the inlet and outlet conditions of the recuperator.

The summation of Q^g and Q^L should be zero, assuming no heat loss to the environment (Equation (4.24)).

$$Q^g + Q^L = 0 \tag{4.24}$$

Finally, the objective function is defined as follows:

$$Profit = (D^{Res} - D^{Plant})P^E - (NG^{PL})P^N - P^C C \tag{4.25}$$

where P^E, P^N, and P^C represent energy price ($/$MWh$), natural gas price ($/kg), and coal price ($/kg), respectively. An hourly energy price is also assumed in this study. This investigation focuses on operating costs, though levelized capital costs could be introduced to the cost functions if investment decisions are to be included.

4.3.2 Controlled variable

The overall power generation from the coal, gas, and wind should always match the sum of the electricity demands for the residential users and the CCC and LNG production facilities, as shown with Equation (4.26)

$$P^{Tot} = D^{Tot} \tag{4.26}$$

To achieve this goal, excess energy production is defined as shown in Equation (4.27) and it is considered as a controlled variable with high and low set point values of zero. This also permits

the assignment of a higher penalty for underproduction of power. Selection of a value of zero for the high and low set points of excess energy production highlights that neither overproduction nor underproduction of power is an optimal solution in practice.

$$P^{Ex} = P^{Tot} - D^{Tot} \tag{4.27}$$

4.3.3 Constraints

Power produced in the gas turbine should always be less than its capacity.

$$P^{GT} \leq GT^{cap} \tag{4.28}$$

Steady state simulations have shown that the combined electricity demand of the LNG and CCC plants is 15-20% of the power generated in the power plant [147]. A value of 20% is adopted for $D^{plant,max}$ in the results presented in this Chapter [170] while a lower value of 15% is considered for the results presented in Chapters 5 and 6 [36]. However, the optimization results shown in Section 4.5 demonstrate that D^{plant} is always less than 15% of $P^{SP,Max}$.

$$D^{plant} \leq D^{plant,max} P^{SP,Max} \tag{4.29}$$

After formulating the system, it is necessary to set up an optimization framework to increase the effectiveness of the hybrid system. The optimization framework used in this system benefits from an objective function in the form of an ℓ_1-norm (2.5). In this equation, a desired objective function for the problem (Equation (4.25)) is added to the expression presented by Equation (2.5a) and forms the overall objective function. The mathematical equations presented by Equation (2.5) are used to tune the model to obtain satisfactory results; i.e., in each simulation, variables $c_y, c_u, c_{\Delta u}$ are adjusted such that smooth results are observed in the trend of the decision variables. Thus, these variables are the tuning parameters for the model. High penalization factors are also assigned for the deviation of the controlled variable from the desired set point. The penalization factors are w_h and w_l to penalize over and under production of power, respectively.

The set of equations discussed is implemented in the APMonitor Modeling Language [29] and solved either with an interior point solver (IPOPT) [71] or an active set solver (APOPT [140,

141]. More information about how to implement an optimization in the APMonitor Modeling Language can be found in [35].

4.4 Model Implementation

In this section, the model developed for the hybrid system of power generation and the non-storing version of the CCC process is implemented with a set of assumptions and input data. In this case, it is assumed that power production in the coal–fired generation unit is based on a simple cycle; i.e. $FG^{NG,max}$ is zero which results in P^{NGCC} be equal to zero).

4.4.1 Model Inputs

In this study, the power output of ten wind power stations, each comprising multiple windmills, in southern California, USA is considered along with coal and gas power generation units. The maximum actual power output from the wind stations is 300 MW while steam boiler has a capacity ($P^{SP,Max}$) of 1200 MW. The steam boiler considered in this investigation is also able to follow the electricity load at a maximum change rate of 7% per minute [171]. A capacity of 240 MW is considered for the gas turbine. A more accurate analysis of the size of the gas turbine is made by considering capital cost of the equipment and is outside the scope of this dissertation.

The electricity demand profile adopted for this section is related to the forecasted data for a zone in southern California, USA. Electricity demand data is taken from [172]; this is the predicted data for 2022 with a maximum of 1200 MW. The assumed data for these variables are typical for most residential areas. The wind power [173] and electricity power prices [174] are represented by 2006 and 2009 data, respectively. Two time periods are selected to compare the effect of seasonal changes on electricity demand and weather condition. The first time period is between July 18$^{\text{th}}$ and July 20$^{\text{th}}$ (summer case), when the peak electricity demand of the year is predicted to occur. The second time period is between January 25$^{\text{th}}$ and January 27$^{\text{th}}$ (winter case), when wind power had the highest standard deviation among all possible three consecutive day time horizons in 2006. Trends of variation of electricity demand data and energy price are presented in Figures 4.2 and 4.3 for the summer and winter, respectively. Trend of wind power for each scenario is shown along with the optimization results shown in Section 4.5.

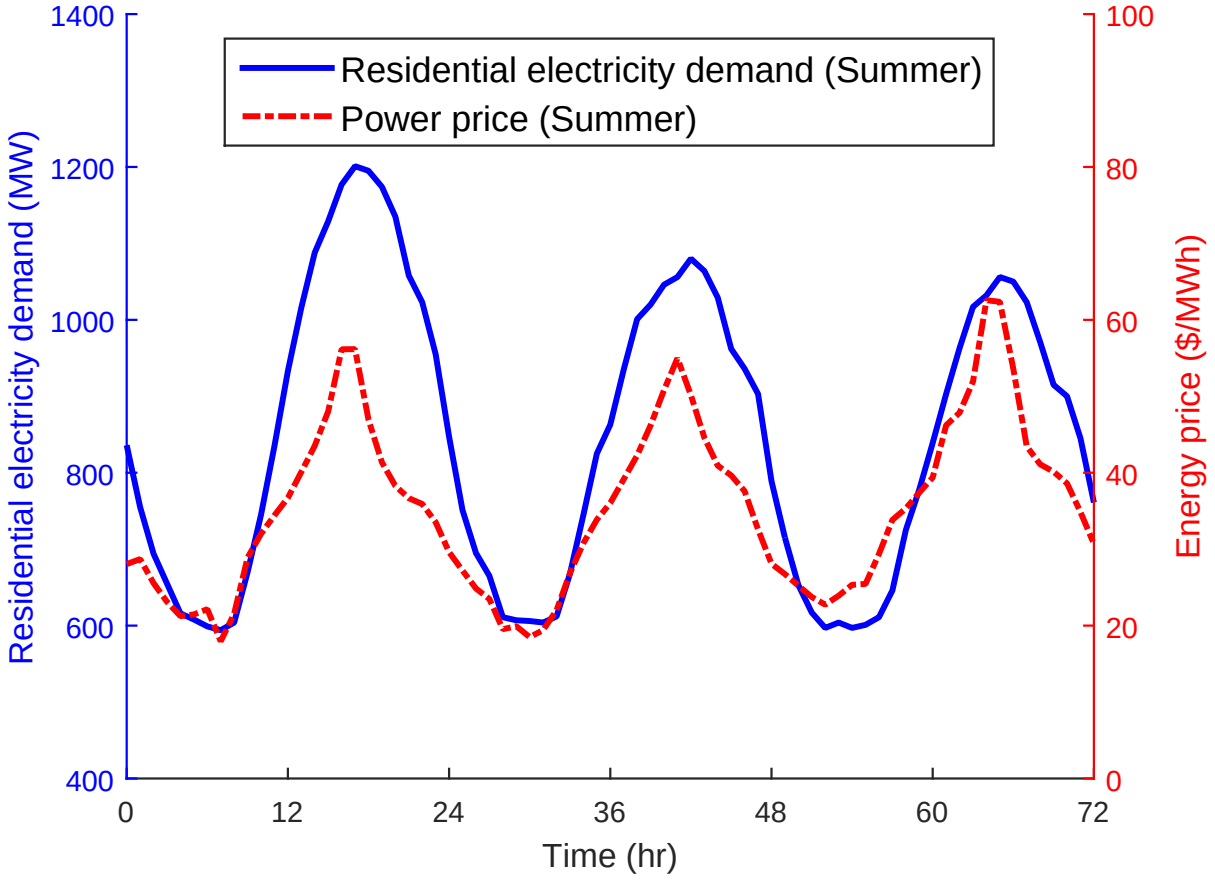

Figure 4.2: 2022 forecasted electricity demand data for a zone in southern California, USA (Summer case) [172].

The simulation time horizon considered in this investigation is 72 hours with one hour time discretization.

4.5 Optimization Results

4.5.1 Comparison Between Summer and Winter Results

The main results of the optimization of the integrated system without energy storage for both summer and winter cases are presented in this section. The summer case result, displayed in Figure 4.4, shows that the total power produced in the system is always greater than or equal to the total electricity demand. The total excess power over the time horizon is approximately zero in this scenario. Coal power is the main source of the electricity generation, while gas power is produced

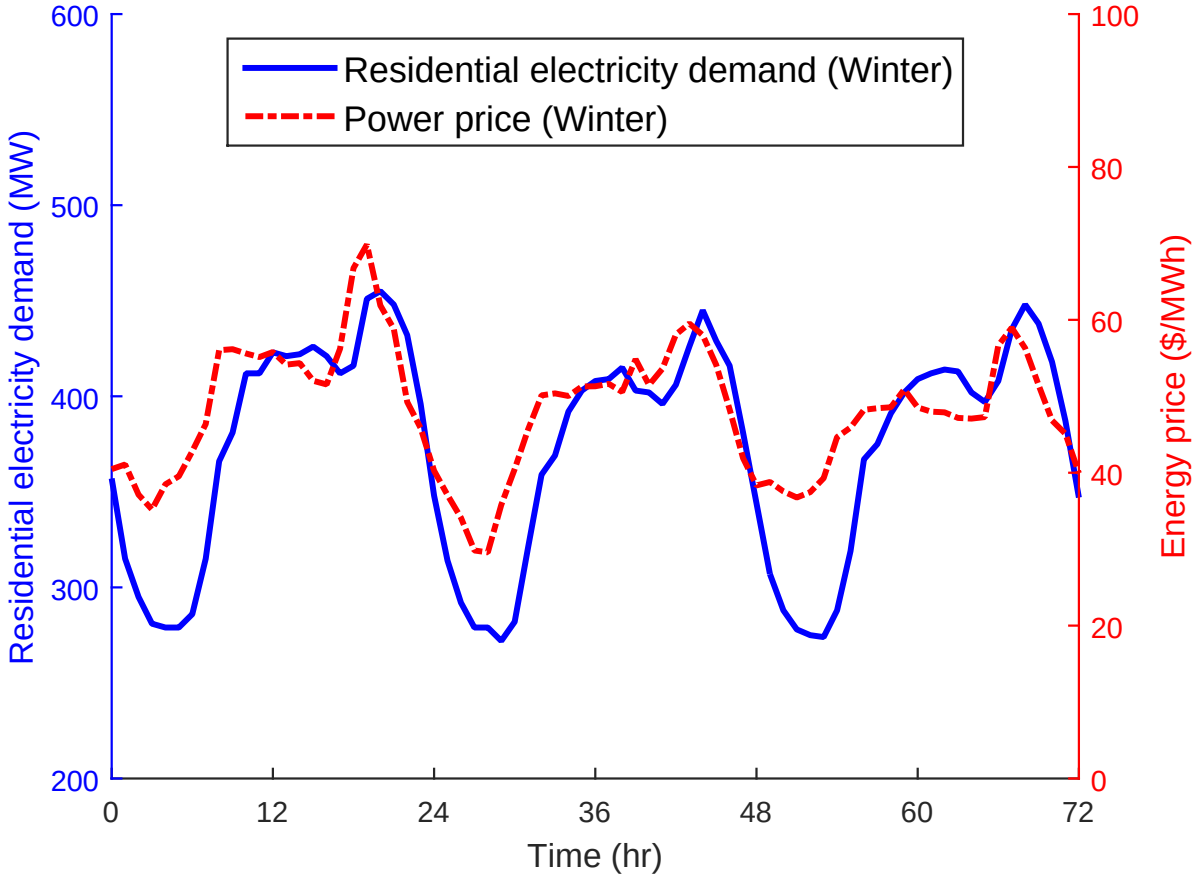

Figure 4.3: 2022 forecasted electricity demand data for a zone in southern California, USA (Winter case) [172].

during peak hours to meet the total electricity demand. Whenever wind is available, it is used first to meet the demand. Coal power is mainly dispatched after the wind while gas power is mostly produced in periods with high electricity demand. Optimization shows a maximum change rate of 0.3% per min for the load in the steam boiler that is less than the maximum anticipated change rate of 7% per minute. Figure 4.4 shows that the combined LNG and CCC electricity demands satisfy the constraint described in Section 4.3.3.

For the winter case (shown in Figure 4.5), the electricity demand decreases significantly and wind power is more readily available than in the summer case. In fact, there are times (such as the period between hours 26 and 29) when wind power can fully meet the total electricity requirement of the residential area and the CCC and LNG plants. Therefore, power production from coal and gas are not needed and are reduced to zero. Wind power also has a high rate of fluctuation in

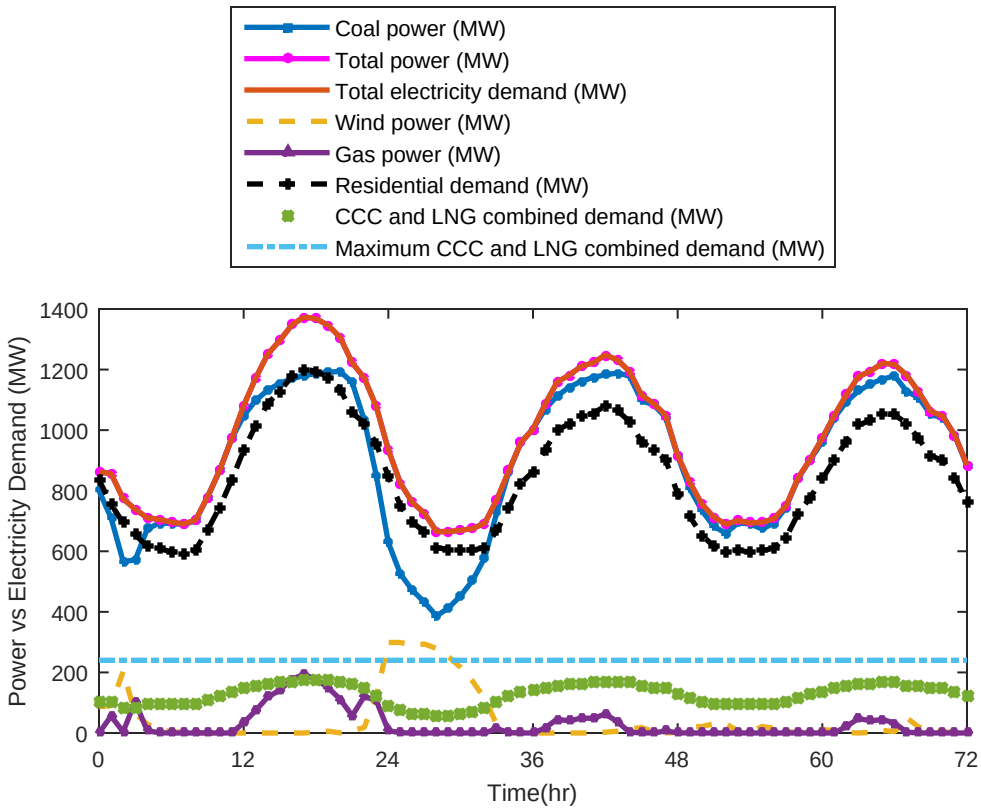

Figure 4.4: Power vs. electricity demand profile (summer case)

the winter. Thus, when wind power is not sufficient to meet the total electricity demand or when it is fluctuating frequently, both gas and coal power are used to compensate for the lack of wind power. Gas power is used as much as possible during peak hours and when wind power is not sufficient. After reaching the maximum allowable limit for gas power, coal power is used to meet the electricity demand. The total excess power over the time horizon is less than 0.6% in this scenario. The maximum rate of load change in the steam boiler (0.2% per min) is also less than the maximum anticipated change rate of 7% per minute. Similar to the summer case, the combined electricity demand for the LNG and CCC plants is less than the assumed upper bound (240 MW).

The range of operation of the steam boiler used in this study is considered to vary from zero to full capacity. While it is important to show the concept of more wind utilization by assuming a lower limit of zero for the steam boiler, the zero limit is not practical. The lower limit of the steam boiler is selected to be zero to add enough flexibility to the hybrid system so as to not produce

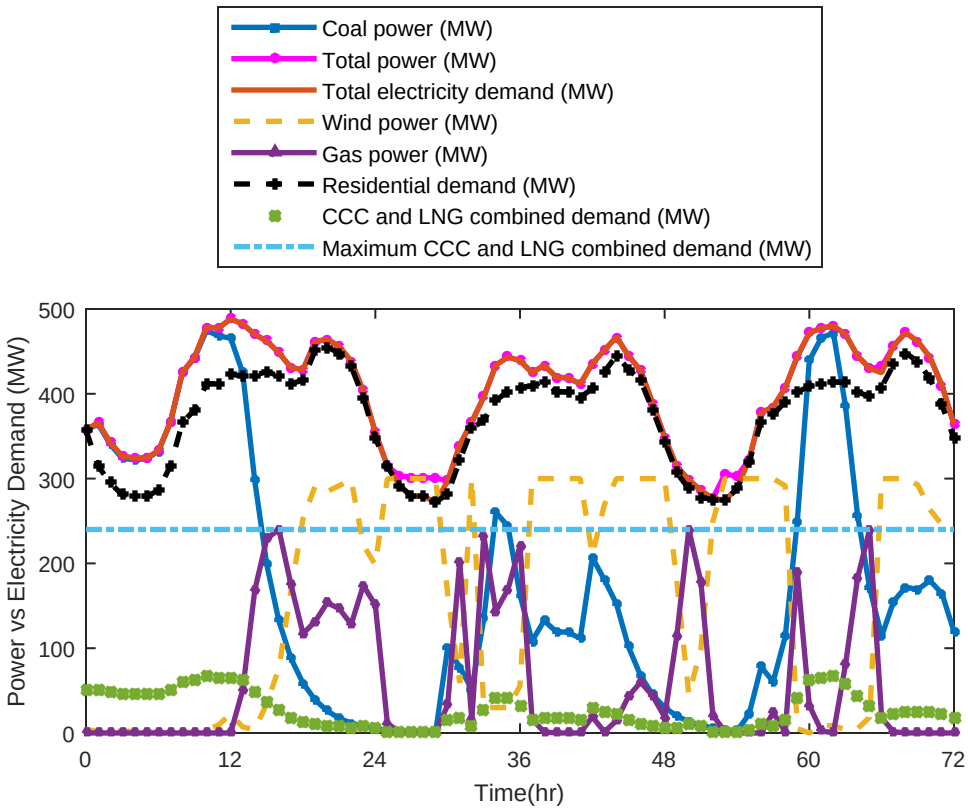

Figure 4.5: Power vs. electricity demand profile (winter case)

excess power. A longer time frame and economical evaluations are needed to find an appropriate boiler capacity. In that case, the simplifying assumption for the lower limit of power output from the steam boiler can be easily modified. Adding the energy storage capability of the CCC process is another viable option to make the rate of change of the boiler smoother [36].

Figure 4.6 shows trends of the natural gas from the pipeline for both summer and winter cases. This figure illustrates how more natural gas is taken from the pipeline during peak hours and when wind power is insufficient. Two reasons are attributed for taking natural gas from pipeline in peak hours: (1) more LNG is required to treat the flue gas of the power plants (2) a fraction of natural gas is combusted in the gas turbine and the amount of natural gas lost due to combustion should be compensated. As mentioned before, when wind power is not sufficient to meet the electricity demand, a combination of gas and coal power is used to achieve this goal. However, the steam boiler's response to the intermittent behavior of the wind power is slow and gas power is used

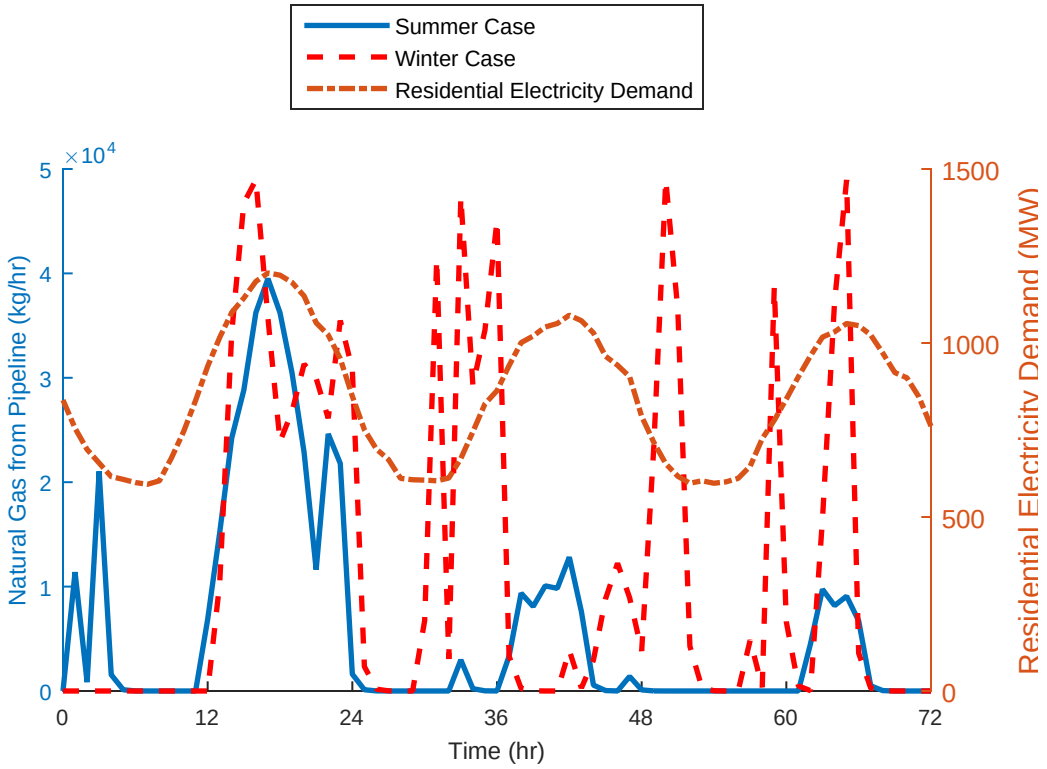

Figure 4.6: Natural gas imported to the plant

more frequently in the winter as the rate of variation of wind power is greater in the winter than the summer. The overall amount of the natural gas taken from the pipeline over the optimization time horizon is approximately 100% more in the winter case than the summer case.

The same trend is observed for the LNG production rate (Figure 4.7). During off peak hours, less LNG is required and it is produced from the recirculating natural gas inside the plant (stream 7 in Figure 4.1). Since more LNG is required during peak hours, the necessary LNG is supplied from both pipeline and recirculating natural gas. The overall amount of LNG produced inside the plant for the winter case is 80% less than the summer case. This difference is attributed to the higher penetration of wind power into the power production unit in the winter. In addition, gas power is produced more than the coal power in the winter case. As CO_2 emissions from the gas combustion are less than from coal combustion, smaller amounts of LNG are required to run the CCC process during the winter. Thus, when more wind power is adopted into the power

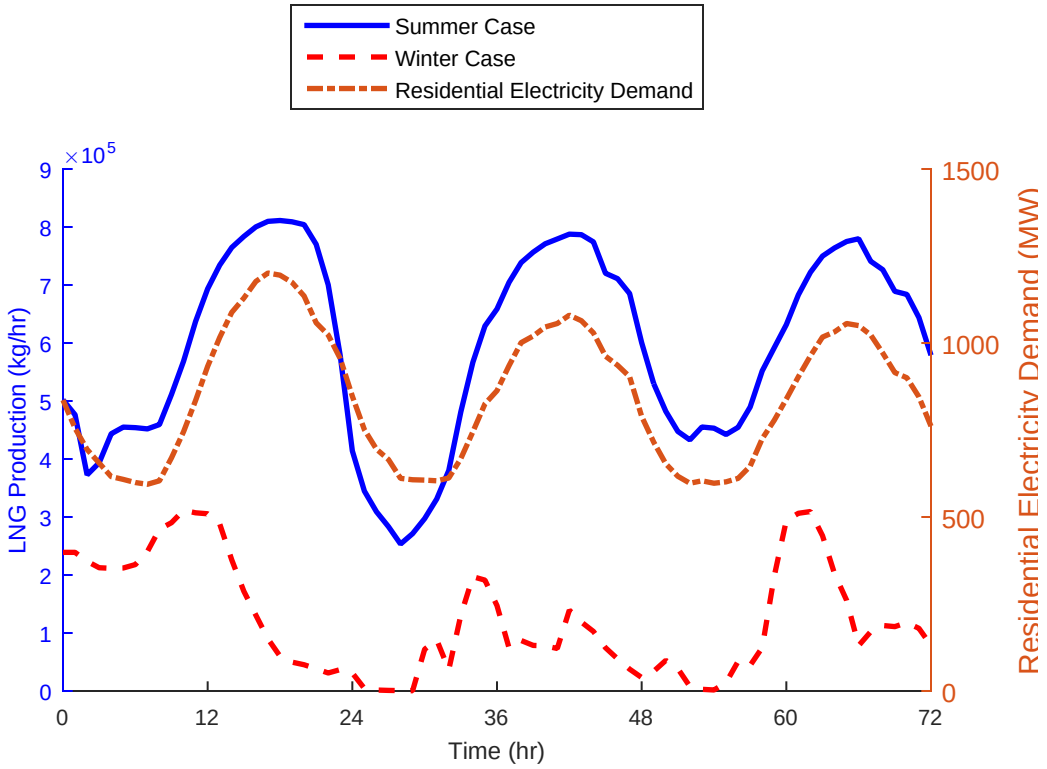

Figure 4.7: LNG production in the system

generation units, the LNG production rate decreases. The same behavior is observed for the sum of the electricity demands for the LNG and CCC plants.

The average operational profit obtained from the integrated system, assuming a constant natural gas price, is approximately \$21k/hr for the summer case. The average operational profit for the winter case is approximately \$13k/hr. The higher profit obtained for the summer case is expected as larger variation in the electricity price creates more benefit from the hybrid system.

4.5.2 Sensitivity Analysis for Wind Power Adoption

Finally, a sensitivity analysis is implemented to compare the effect of different rates of wind power adoption on the utilization of coal and gas power. For the cases outlined in this section, the winter data and a wind adoption factor (α) are used to define the fraction of the available wind power adopted in power generation. When $\alpha = 1$, all of the available wind power is adopted to

meet the electricity demand, while $\alpha = 0.5$ means that only half of the available wind power is used. As shown in Figure 4.8, adopting more wind power causes less coal power production. However, gas power has higher influence at higher wind power adoption rates; this is due to its fast response to the intermittent behavior of the wind power. Using more gas power is advantageous as coal power produces more CO_2 and using more wind and gas power results in lower electricity demands for the LNG and CCC plants. Conversely, lower adoption of the wind power requires more power to be produced from coal to meet the total electricity demand.

The impact of the adoption factor on the profitability of the hybrid system is shown in Figure 4.9. The revenue of sale of electricity to residential consumer is constant at all values of α. Coal cost and the electricity cost to run the LNG and CCC plants decrease by adopting more wind power into the power generation units. However, gas cost increases by increasing the wind power adoption factor. This conclusion is expected because gas power, as opposed to coal power, is used more to meet the total electricity demand when more wind power is adopted. It is observed from Figure 4.9 that at $\alpha = 0.66$ the integrated profit over the simulation time is at a maximum. This means that at this value, a combination of the three power sources lead to the maximum profit obtainable from this system for the winter case. Thus, further adoption of the wind power does not increase profitability in the assumed hybrid system. The average profit obtained from the hybrid system at a wind adoption factor of $\alpha = 0.66$ is \$14.5k/hr. The natural gas price used to obtain results in Figure 4.9 is an average value of 5.74 \$/Mcf. However, the same trend in the profitability is obtained with a natural gas price ranging from 3.54 to 18.25 \$/Mcf. This price range is sufficiently wide to capture the possible growth in the natural gas price in 2022 [175, 176] and is sufficient for the purpose of this study. Change in the coal price from 12.65 \$/ton to 17 \$/ton (the projected price for the Powder River Basin coal in 2022) also leads to the same conclusions.

4.6 Conclusion

The impact of the CCC process (a post-combustion CO_2 removal process) on fossil-fueled power plants is considered in this chapter. The CCC process is considered as a response to the tightening restrictions on CO_2 emission from fossil-fueled power plants (such as the new regulations recently unveiled by the EPA in the Clean Power Plan). The fast response of the CCC process to electricity demand helps utilize more renewable energy sources on the grid, which emits less

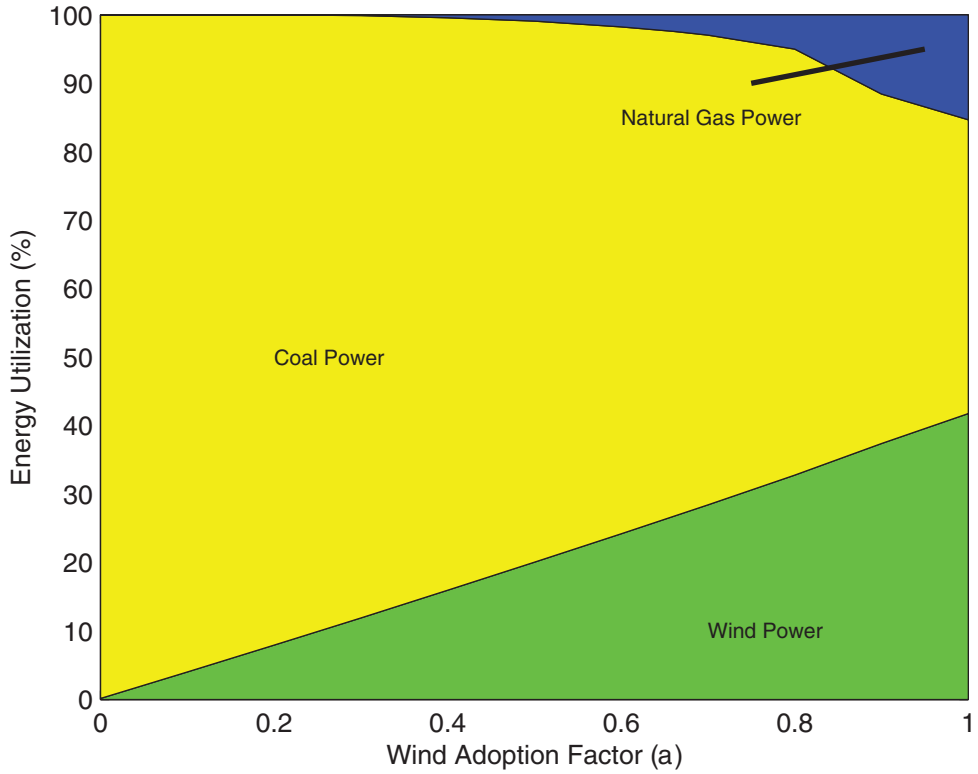

Figure 4.8: Impact of wind power adoption factor on power production from gas and coal (winter data)

CO_2. The effects of seasonal variations in electricity demand and wind availability are investigated by considering the summer and winter cases. The proposed hybrid system is able to meet the total electricity demand. All of the available wind power is utilized in this study to meet the electricity demand. The operating profit obtained from the proposed system for the summer case is \$21k/hr, while the winter case profit is approximately \$13k/hr. The larger availability of wind power in the winter leads to 100% more intake of natural gas to the plant than in the summer case. LNG production over the optimization time horizon decreases by 80% for the winter case.

A sensitivity analysis examines the change in operating strategy of the proposed system with respect to the wind power adoption factor (α). At higher values of α, coal power utilization decreases while gas power utilization increases. At $\alpha = 0.66$, the profit obtained to run the integrated system in the winter is at a maximum.

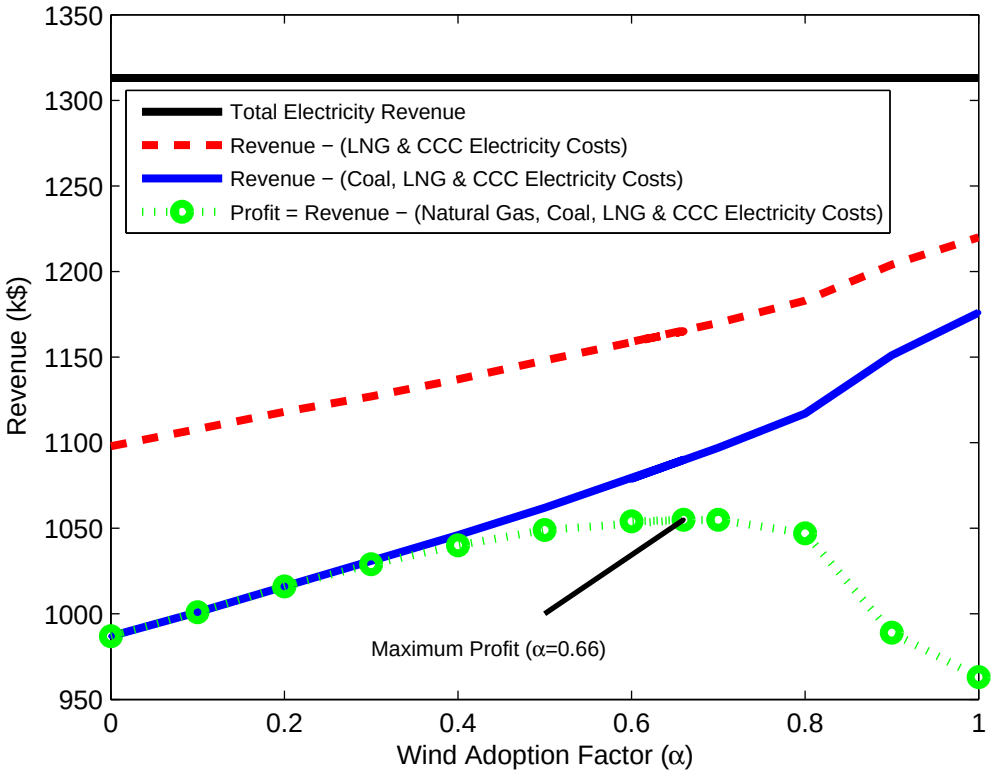

Figure 4.9: Operating costs and electricity demand revenue vs wind power adoption factor (α) (winter data)

The hybrid system of a load–following power generation unit and the CCC process with the associated energy storage facilities is addressed in Chapter 5. Furthermore, the impact of the CCC process on a baseline power plant is the focus of Chapter 6.

CHAPTER 5. INVESTIGATING THE IMPACT OF ENERGY-STORING CRYOGENIC CARBON CAPTURE ON POWER PLANT PERFORMANCE

5.1 Introduction

As mentioned in Chapter 4, the CCC process requires two refrigeration loops that consume most of the energy in running the compressors. However, refrigerant can be generated during non-peak hours and stored in insulated vessels that save the refrigerant for peak hour usage, thereby replacing the compressor energy with the stored refrigerant. This causes the refrigerant production rate to decrease during peak hours, which decreases the energy demand required by the CCC for as long as the stored refrigerant is available. Therefore, more power is available during peak hours relative to the baseline coal boiler rated capacity. Generating the refrigerant during non-peak hours, when electricity is cheaper, also results in higher profits. In this investigation, storage of only one of the refrigerants is considered as it provides more energy during the recovery mode. The refrigerant considered for this purpose is LNG, although others could be selected.

In addition, the LNG generation and storage cycle primarily involves compressors and heat exchangers; therefore, the storage/recovery or load changing response time is fast (seconds) compared to those of the steam boilers (hours). The faster energy storage response time is well matched to intermittent sources like wind turbines. Therefore, this energy storage system enables the steam boiler to follow rapidly changing loads. Storage capacity of LNG vessels also allows scaling from the proposed energy storage to large-scale systems.

The hybrid system of power generation units and energy-storing version of the CCC process is shown in Figure 5.1. To better represent the storage and recovery modes of operation, a stream (stream 6 in Figure 5.1) bypasses the tank. The storage tank allows natural gas to be imported from the pipeline and converted to LNG during periods with low electricity prices. The fraction of the produced LNG required to run the CCC process during off peak hours directly flows toward the process through the bypass stream. The excess LNG flows to the tank inlet (stream 5 in Figure

5.1). During peak hours or periods with expensive electricity prices, LNG is supplied from two sources: (1) the storage tank (2) the liquefaction of the recirculating natural gas. As for the case study without energy storage, the LNG directed to the CCC process (stream 8 in Figure 5.1) is vaporized so that heat is removed from the process. The natural gas coming from CCC (stream 9 in Figure 5.1) has sufficient cooling potential to be used to liquefy a fraction of the recirculating natural gas (stream 13 in Figure 5.1). Thus, by passing the cold natural gas coming from the CCC (stream 9 in Figure 5.1) through the LNG/mixed refrigerant (MR) recuperator, heat is recovered from the warm recirculating natural gas (stream 13 in Figure 5.1). Therefore, a fraction of the required LNG for running the CCC process is supplied from the recirculating natural gas. The rest of the required LNG is supplied from the tank (stream 7 in Figure 5.1). Thus, LNG production is ramped down during peak hours by using an LNG storage tank; i.e. the parasitic loss of the mixed refrigerant compressor decreases in peak hours or when electricity is expensive. However, it should be emphasized that at any given time, either the storage or recovery mode is always in operation. The combination of the LNG storage tank, LNG/MR recuperator, mixed refrigerant compressor, and natural gas compressors used in LNG production is referred to as the LNG plant.

Another option to decrease energy consumption in the LNG plant is to export a fraction of the recirculating natural gas to the pipeline (stream 1 in Figure 5.1) and avoid processing it in the LNG/MR recuperator. However, the pressure of the natural gas before the natural gas compressor is approximately 11 bar and the pressure of the pipeline natural gas is approximately 55 bar; thus, the pressure must be increased to pipeline pressure if natural gas is to be exported. A pressure increase is implemented in two stages in this study: (1) in the natural gas compressor (from 11 to 37 bar) and (2) in the pipeline compressor (from 37 to 55 bar). The pressure increase in the natural gas compressor should always occur, even if natural gas is not exported to the pipeline. However, the pressure increase in the pipeline compressor does not significantly increase the parasitic loss of the plant (approximately 3.2 MW). The exported natural gas also offers a lower CO_2 concentration and is more pure than the imported natural gas because of the purification that occurs through the refrigeration cycle. The natural gas export is a cost saving measure for the integrated system as it recovers part of the operating costs for unused natural gas. However, the price value of the more pure natural gas is the same as the natural gas from the pipeline in this investigation and is not awarded extra credit for the purification. This is mainly because of the unwillingness of

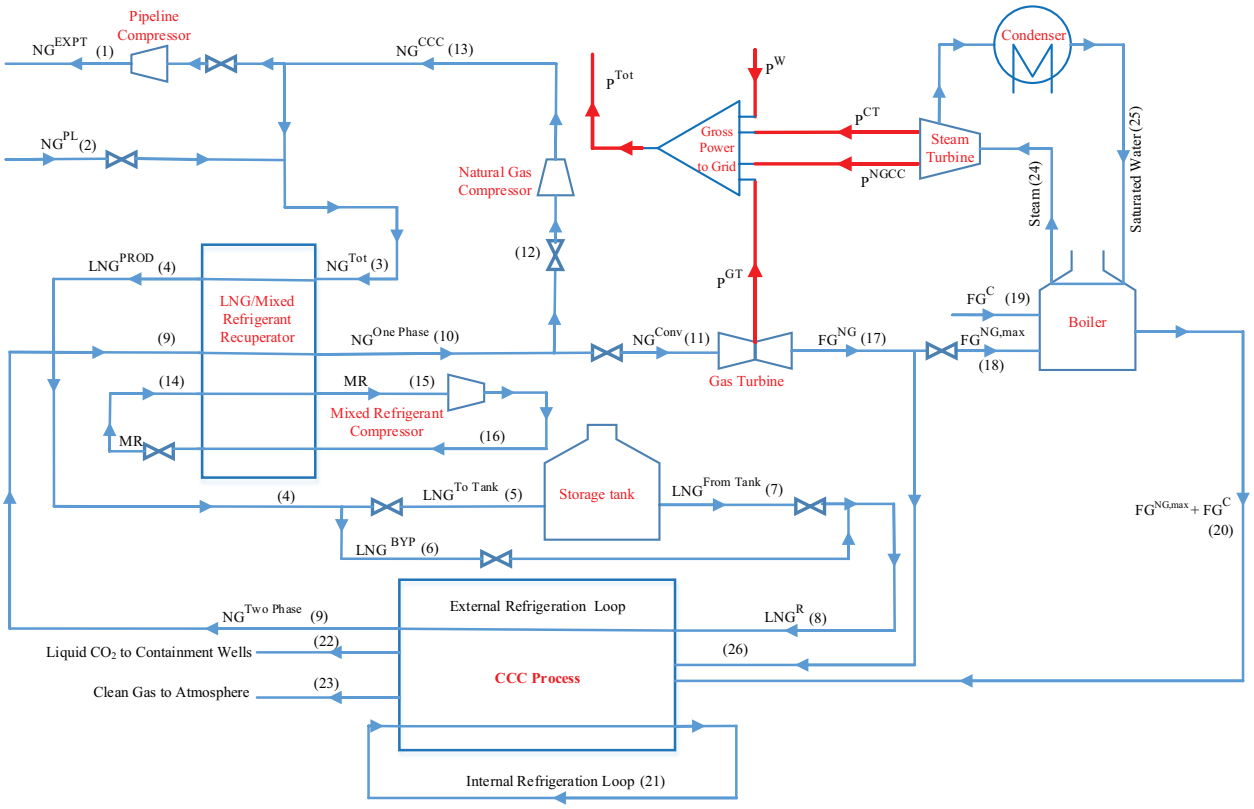

Figure 5.1: Schematic configuration of the integrated system of power generation unit and the CCC process with energy storage

the utility contractors to buy back natural gas at a higher price. In other words, if natural gas is to be simultaneously purchased or sold to utility contractors, the sale and purchase price will be equal. This study assumes constant natural gas price. Decisions about whether natural gas should be exported or imported at each time step are based on the economic evaluation of the objective function.

The focus of this chapter is on the optimization of the hybrid system of power generation units and the CCC process with consideration of the energy storage of the capture system. The coal–fired power plant considered in this chapter is capable to follow the electricity demand load with a maximum change rate of 7% per minute. The remainder of this chapter is divided into four sections; in the first section, an example case study is discussed to demonstrate the concept of peak-shaving of the electricity demand by using an energy storage system. Then, some of the equations developed in chapter 4 are modified to account for the energy storage and export of natural gas to

pipeline. Next, the inputs for this hybrid system are presented. Finally, simulation results for the integrated system are discussed.

5.2 Example Case Study for Energy Storage Concept

In this section, an example case study is developed to demonstrate the energy storage concept. The main power generation unit output is assumed to be constant in this case. Excess energy is stored during off-peak hours or when more energy is available than the required electricity demand. The stored energy is used during peak hours to meet the higher electricity demand. The objective is to minimize the power production unit output. This goal is obtained by efficiently using the energy storage system to meet the cyclical demand cycle that is typical for a grid-scale power distribution system. The assumed demand profile has a periodic form that is typical for both industrial and residential areas. As energy storage and energy recovery are not coincident, slack variables are used in this example case to help the optimizer switch between energy storage and energy recovery. The time horizon considered for this simplified case is 24 hours with 20 minute time discretization.

The equations used to model this simplified case are given below. These equations represent a simple power dispatching system and demonstrate the concept of peak-shaving of the electricity demand by using an energy storage system.

$$min \quad P \tag{5.1a}$$

$$s.t. \qquad \frac{\delta I}{\delta t} = S \cdot \varepsilon - R \tag{5.1b}$$

$$S = P - D + S_2 \tag{5.1c}$$

$$R = D - P + S_1 \tag{5.1d}$$

$$P - D = S_1 - S_2 \tag{5.1e}$$

$$S_1, S_2 \geq 0 \tag{5.1f}$$

$$S_1 \times S_2 \leq 0 \tag{5.1g}$$

$$P + R - S \geq D \tag{5.1h}$$

$$I \geq 0 \tag{5.1i}$$

where P, D, S, R and I represent power production, electricity demand, stored energy, recovered energy, and inventory of stored energy, respectively. S_1 and S_2 are slack variables to help switch between energy storage and energy recovery and are constrained to be positive. The efficiency loss during storage of energy is represented by ε. Equation (5.1a) defines the objective function. Equation (5.1b) represents the energy balance for the energy storage system. Equations (5.1c) and (5.1d) represent the magnitude of the stored and recovered energy, and Equation (5.1e) defines the magnitudes of S_1 and S_2. Equations (5.1f) and (5.1g) ensure that storage and recovery modes do not operate simultaneously (either S_1 or S_2 or both should be zero during the time horizon). Equation (5.1h) guarantees that power supply from power production and energy recovery, with consideration of the storage of energy during off peak hours, is always greater than the electricity demand. Equation (5.1i) ensures that energy inventory is always greater than or equal to zero. According to the optimization framework proposed previously, Equation (5.1c) to (5.1e) serve as the equality constraints (Equation (2.5c)) while and Equation (5.1f) to (5.1i) serve as the inequality constraints (Equation (2.5d)).

When S_2 is zero, S_1 is equal to $P - D$, according to Equation (5.1e). Consequently, S equals excess energy $(P - D)$ based on Equation (5.1c) and R equals zero in agreement with Equation (5.1d). Thus, this case represents the storage mode, and the inventory of the storage system increases according to Equation (5.1b). When S_1 is zero, S_2 becomes $D - P$ from Equation (5.1e). Consequently, R equals $D - P$ from Equation (5.1d) and S equals zero. Thus, this case represents the recovery mode, and the inventory of the storage system decreases according to Equation (5.1b).

Results of the simplified case are presented in Figure 5.2. As shown in the figure, when power generation is more than the required electricity demand, energy is stored and the energy inventory of the storage system increases. When electricity demand is greater than the power production, energy is recovered from storage and energy inventory in the storage system decreases. Slack variables show consistent trends with these findings. This example case demonstrates the energy storage optimization concept used in the more detailed case of power production with CCC.

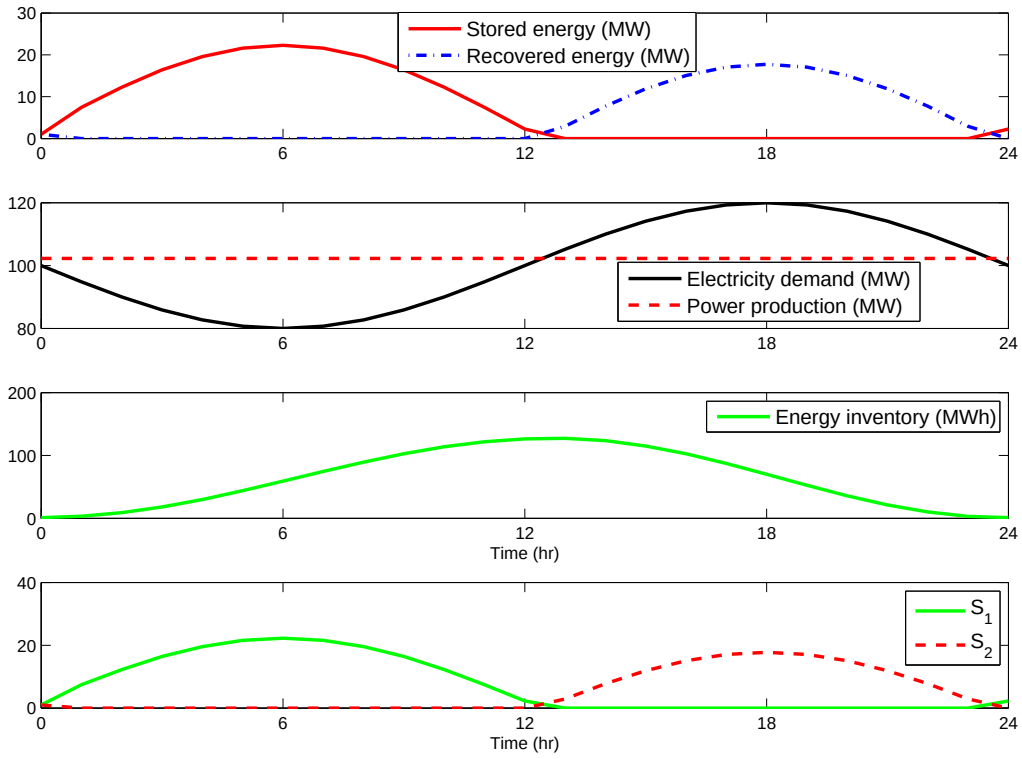

Figure 5.2: Results for the simplified case of energy storage

5.3 Modeling Framework for the Energy-Storing Hybrid System

5.3.1 Governing Equations

This section considers the modification of some of the equations developed in Chapter 4 to account for the energy storage and export of natural gas to pipeline. Except for the equations and figures that are modified in this chapter, similar relationships used in Chapter 4 are used for the hybrid system with energy storage.

In the system considered in this chapter, the flow rate of natural gas exported to the pipeline is deducted from the total recirculating natural gas (NG^{Tot}). As all relations are expressed on a mass basis, NG^{Tot} also equals LNG^{Prod}. Thus, total LNG production should also be modified (Equation (5.2)). The energy balance over the recuperator is also modified accordingly.

$$LNG^{Prod} = NG^{PL} + NG^{CCC} - NG^{EXPT} \tag{5.2}$$

In this case, NG^{EXPT} represents the natural gas exported to the pipeline (kg/hr) and is a decision variable. Produced LNG also equals the summation of the LNG to the tank and the LNG bypassing the tank Equation (5.3):

$$LNG^{Prod} = LNG^{To\ Tank} + LNG^{BYP} \tag{5.3}$$

In Equation (5.3), $LNG^{To\ Tank}$ and LNG^{BYP} represent the LNG directed to the tank and the amount that bypasses it. $LNG^{To\ Tank}$ is also a decision variable in the hybrid system with energy storage. LNG from the tank is calculated from a mass balance at the tank outlet Equation (5.4):

$$LNG^{From\ Tank} = LNG^{R} - LNG^{BYP} \tag{5.4}$$

A dynamic mass balance equation is also developed in Equation (5.5) for defining the inventory of tank, LNG^{Tank}:

$$\frac{d(LNG^{Tank})}{dt} = LNG^{To\ Tank} - LNG^{From\ Tank} \tag{5.5}$$

The work of compression of pipeline compressor ($D^{NG,Pipe}$) is 0.01 kW per kg/hr of the inlet stream [36] and is based on the results obtained previously [147, 164]. After unit conversion, this leads to the following equation:

$$D^{NG,Pipe} = 1 \times 10^{-5} NG^{EXPT} \tag{5.6}$$

The total electricity demand from the CCC and LNG production facilities, D^{plant}, is then calculated from Equation (5.7):

$$D^{plant} = D^{CCC} + D^{NG,Comp} + D^{MR,Comp} + D^{NG,Pipe} \tag{5.7}$$

The profit function used in this investigation is also modified to account for the export of natural gas Equation (5.8).

$$Profit = (D^{Res} - D^{Plant})P^{E} - (NG^{PL} - NG^{EXPT})P^{N} - P^{C}C \tag{5.8}$$

An hourly energy price is also assumed in this analysis. As mentioned before, the credit given to export of the natural gas is considered to be the same as the purchasing price of the imported natural gas. The electricity demand profile is an input to the model and is not a decision variable. Revenue obtained from selling the electricity (first term in the right hand side of Equation 5.8) is constant in all scenarios considered in Section 5.5. Thus, the optimizer actually tries to optimize the profit function from the remaining expressions in Equation 5.8. Using the electricity demand in the profit function, however, would provide a comparison basis for the profitability of the hybrid system.

A time horizon of eight days with one hour time increments is considered for profit maximization. By removing the boundary conditions, the performance of the three middle days represents an infinite time horizon. Because of the complexity of the model and the large number of variables and equations to be solved, initialization strategies developed in Chapter 2 are applied to decrease the computational time of the simulations.

5.3.2 Constraints

As mentioned in Section 5.1, either energy storage or an energy recovery mode is in operation at each time step. The selection of operating mode depends on the economic evaluation of each time step. The constraint developed in Equation (5.9) helps the optimization algorithm choose between the operational strategy at each time step:

$$LNG^{To\ Tank} LNG^{From\ Tank} = 0 \tag{5.9}$$

While this constraint assumes that either $LNG^{To\ Tank}$ or $LNG^{From\ Tank}$ is zero at each time step, LNG^{BYP} always has non-zero values. This is because of the continuous demand of LNG to the CCC plant for the treatment of CO_2 produced from the power plant. It is also unlikely that import and export of natural gas occur simultaneously in practice. Thus, a similar relationship is assumed between them (Equation (5.10)):

$$NG^{PL} NG^{EXPT} = 0 \tag{5.10}$$

5.4 Model Inputs

In this investigation, a residential electricity demand profile is used as the actual hourly integrated data for San Diego, USA, for the period between September 13, 2014 and September 20, 2014. These data give the peak electricity demand of the year in the area [177]. Because this study represents the integration of the CCC process with only one power generation unit, the electricity demand data is scaled to have a maximum residential demand of 2000 MW. The assumed electricity demand profile is typical for many residential areas and is shown in Figure 5.3. The average price of electricity for the same period in 2014 for California is also shown in Figure 5.3 [178]. It is seen from Figure 5.3 that periods with high electricity demand also have more expensive power price. Wind data shown in Figure 5.4 are based on the actual wind power data for the same period of time in 2014 for southern California (SP-15 trading hub) [177]. This study assumes that wind power only contributes up to 10% of the integrated residential demand over the time horizon. Thus, total actual hourly wind power data from the SP-15 trading hub is uniformly scaled down such that integrated wind power over the time horizon is approximately 10% of the integrated residential demand used in this investigation. It should be mentioned that the assumed residential electricity demand and wind power curves are for one of the possible worst-case scenarios (summer days) when the electricity demand reaches the maximum of the year in the assumed zone in California in 2014. The trend of the power price in the period of time considered in this investigation shows less spikes than the rest of the year [178]. More severe fluctuations are expected to improve the economic justification for energy storage with the CCC. A typical period was therefore selected over an extended time frame without inflating the benefits.

As for the case without energy storage, excess natural gas produced from the hybrid system is combusted in a gas turbine for power production. The hot gas outlet from this turbine is combined with the coal gases in the boiler convection pass, which gives the turbine the efficiency of a combined-cycle system. Thus, a fraction of the flue gas from gas turbine (stream 18 in Figure 5.1) is directed to the steam boiler to produce steam for power generation and the rest of it (stream 26 in Figure 5.1) is directed to the CCC plant. Despite the fact that the flue gases produced from coal and gas combustion have different compositions, it is assumed that the flue gas exhausts from both streams are treated with the same CCC process for simplicity (Figure 5.1). One approach to operating with only one boiler for both flue gas exhausts is to consider a recirculation cycle after

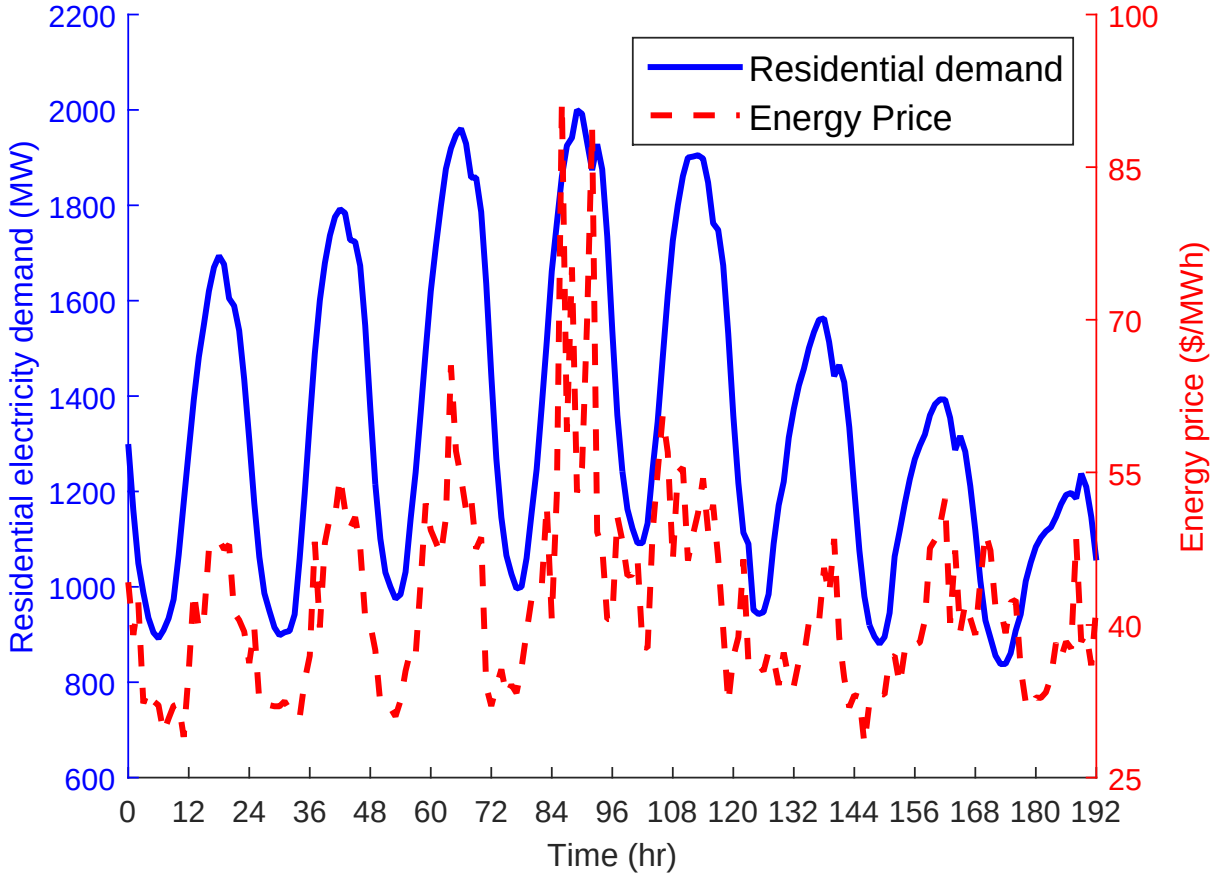

Figure 5.3: Actual electricity demand for San Diego, USA, and average power price for California for the period between September 13, 2014 and September 20, 2014 [177, 178].

the gas turbine, in which part of the natural gas flue gas is recirculated and introduced back into the compressor inlet. As a result, the CO_2 concentration of the natural gas flue gas directed to the boiler can be increased to the coal flue gas CO_2 level [179–181]. The recirculation concept is the subject of future work and is not included in this contribution.

In addition, it is presumed that the set point of power production in the steam turbine (P^{SP}) can vary from 800 to 1800 MW. The capacity of the gas turbine is also assumed to be 50% of the maximum residential electricity demand (2000 MW) considered in this investigation (see Table 5.1). While the presumed turbine capacity is large and is not a typical capacity size in practice, it should be noted that the assumed electricity demand profile has a large range of variation (838 to 2000 MW). Because the gas and steam turbines considered in this work are the main energy sources during peak hours and the steam turbine is anticipated a baseline unit, it is not possible to meet the

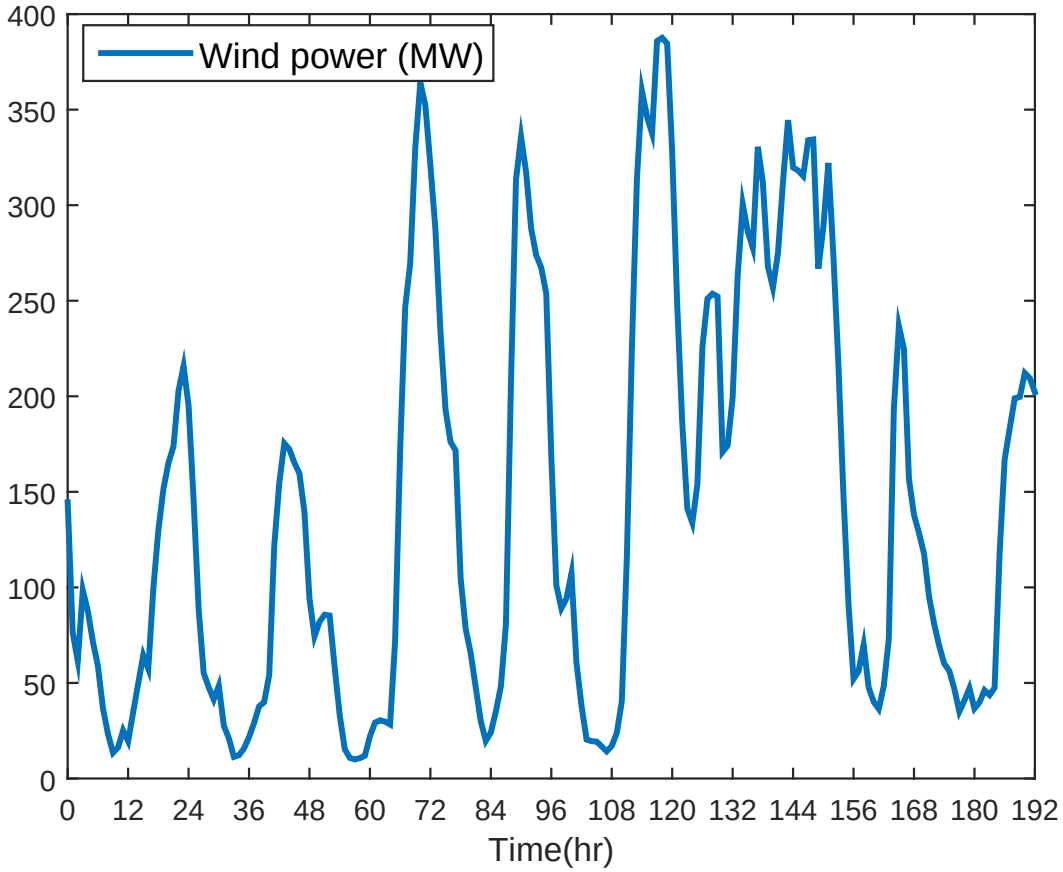

Figure 5.4: Actual wind power data for the period between September 13, 2014 and September 20, 2014 [177].

peak of the residential electricity demand without a large gas turbine. With current technologies, such a large fluctuation in electricity demand is met through several peaking generation units. Thus the need for oversized gas or oil turbines is eliminated. With a single power generation unit it is not possible to meet the large gap between maximum and minimum electricity demand. The need to optimize load following capacity highlights the importance of simulating a power grid in which the fossil–fueled power generation units are equipped with the CCC process. In this case, peak electricity demand is met through a combination of power sources. In addition, the energy storage portion of CCC can effectively become the grid spinning reserve by adjusting its parasitic load in time to accommodate the dispatch schedule of the grid. This large–scale energy storage capacity has the potential for significant economic and operational benefit. Study of a large scale power grid system when fossil–fueled power generation units are equipped with the CCC process is the focus

Table 5.1: Additional input parameters for the case with energy storage

Parameter	Value
GP_{max}^{CC} (MW)	360 (20% of the upper bound for the steam turbine power output)
Maximum residential electricity demand (MW)	2000
Gas turbine capacity (GT^{cap}) (MW)	1000

of future work. For the purpose of a single generation unit, it is assumed that a large capacity for the gas turbine is a valid assumption. The pressumed overall efficiencies of the coal and gas-fired power plants are also 36.8% and 50.2%, respectively, based on higher heating values (HHV) [166].

The coal composition used in this work is that of the subbituminous Wyoming Powder River Basin coal as given in Table 4.2. Delivered coal price for Wyoming Powder River Basin is assumed to be $12.65/ton as of March 2014 [182]. Composition of the imported natural gas is also taken from Table 4.3. Natural gas price is the US national average price of 2014 for the electric power sector ($5.19 per thousand cubic feet) [183]. Long-term contracts can be secured to reduce the variability of fuel costs from sources such as natural gas.

The set of equations discussed in this chapter along with those described in Chapter 4 is implemented in the APMonitor Modeling Language [29] and solved either with an interior point solver (IPOPT) or an active set solver (APOPT).

5.5 Results and Discussion

This section presents the results of the optimization of the integrated system with energy storage. The results are for a case study with an LNG tank capacity of 8 million kg. This tank capacity is selected based on the performance of the hybrid system because the overall trend of variables does not change with different tank sizes. As mentioned previously, all variables are presented in mass units to remain independent of the pressure and temperature conditions of the LNG tank. For typical LNG at the tank temperature and pressure of -94 °C and 37 bar (LNG density is 290.6 kg/m^3), the standard capacity for the 8 million kg LNG inventory is 28000 m^3, which is small compared to LNG tanks in commercial use and represents a very small incremental expense as a fraction of the overall CCC process and power plant.

Electricity demand and power production curves (Figure 5.5) show that a dynamic combination of power sources meets the power demand over time. Power production from coal combustion is the main source of power (with a potential capacity of 1800 MW power generation) and the gas turbine is mainly used for peak-shaving. However, when wind power is available, less coal and gas power are produced and the required demand is met from all three resources. Power produced from natural gas combustion allows for a maximum power output of 1000 MW, though the power output from the turbine only reaches the maximum when electricity demand is at the maximum of the year (the middle four days). The heat content of the flue gas from gas turbine produces extra steam in the boiler. When the inefficiency of steam turbines is taken into consideration, the maximum steam produced as a result of the heat exchange of the flue gas is equivalent to 190 MW of power during peak hours. Therefore, combustion of the vaporized LNG during peak hours compensates for the parasitic loss of the CCC and LNG plant and is able to deliver power up to 1190 MW.

While the maximum capacity for coal-based power generation is 1800 MW, variation limitations of the boiler, the economic advantages of natural gas power, and the intermittent generation from wind cause the optimized coal power production to stay below 1000 MW. This limited power production from coal is also because of the slow response of the boiler to ramp up to meet the peak demand. Relaxing the rate of change constraints on coal power leads to more power production from coal (not shown here). The maximum variation in the boiler load at any time step for the constrained case is less than 0.1% per minute (76 MW in an hour); thus, maximum variation in boiler load is much less than the assumed allowable change rate (7% per minute). The boiler also operates in the typical range of 45-100%.

The dynamics of wind generation require a detailed discussion. This optimization technique looks both backward and forward in time, resulting in power dispatch that anticipates to some degree the future behavior of wind. Wind conditions can be accurately predicted about 24 hours into the future, with accuracy decreasing to near zero as time increases to about 72 hours. Unlike the quite predictable and mostly periodic total power demand, wind is neither predictable in the long term nor periodic, and the wind data here are both representative of quite different results on different days and of the time of day when wind is most available. Specifically, wind on average blows more during off-peak than during peak power demand. One of the great challenges

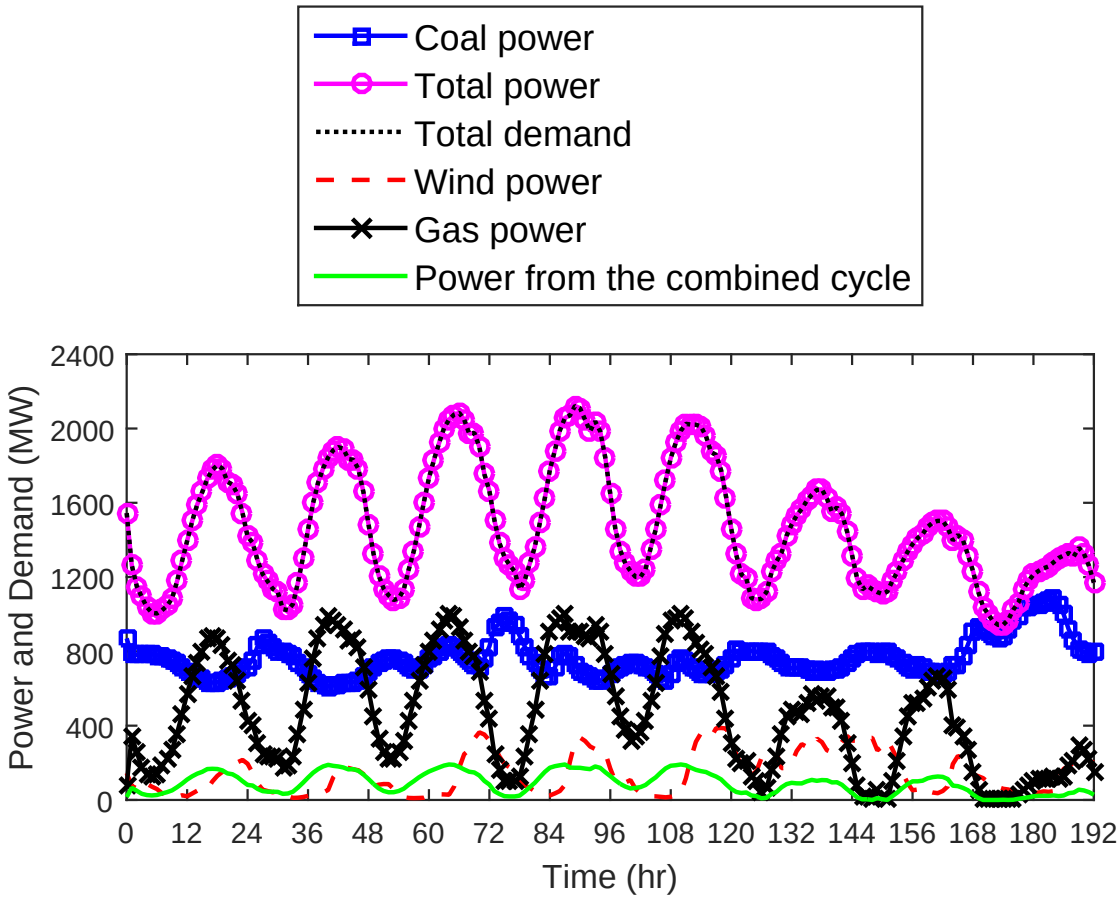

Figure 5.5: Electricity demand vs. power production

of intermittent sources such as wind is to maximize its value and contributions on the grid even though it contributes mostly during low-value periods and in inconsistent ways. These data show how the CCC process provides a synergy between wind and coal power that significantly benefits both processes.

Figure 5.6 better presents the trends of power production and electricity demand for the period between hours 36 and 80 (also shown in Figure 5.5). Between hours 36 and 60, it is seen from Figure 5.6 that integrated wind power is much less than that of hours 60 and 84 (approximately 50% less). The surge in wind power for the period between hours 60 and 84 would generally be known to a dispatcher by hour 36. As indicated in the data, the amount of power produced from the coal boiler began to decrease a few hours prior to the wind coming on line, with the energy storage component of the CCC making up the difference until the anticipated wind power had material-

ized. The energy storage of the CCC comes from the reduced parasitic load in the coal plant, which is not directly plotted but corresponds with the natural gas power production. In effect, the CCC process has moved the wind power and the stored energy in the LNG tank that was filled in the evening and night hours of the day before from a time of day when power demand is decreasing to near the peak power demand, optimizing its value on the grid both in economic terms and in CO_2 reduction. In contrast, for the period between hours 36 and 60, when wind was not significant, the energy storage from the previous evening had to make up most of the power demand that the coal boiler could not provide, and coal power production remained high during a longer portion of the day.

This illustrates how the coal system with energy storing CCC can effectively move the wind power to peak demand when it is available and can compensate for a lack of wind when it is not sufficient, providing significant benefit to grid stability and to the economies of both systems. While it is not shown here, wind is generally shifted forward or backward in time to the nearest available peak in power demand, within a 24-hour window.

The LNG inventory, LNG production, and LNG requirement to run the CCC process with the electricity price appear in Figure 5.7. Natural gas flowing to and from the pipeline and electricity price appear in Figure 5.8. In this study, LNG inventory is initialized from a non-zero value because the integrated system of power generation and the CCC should be in operation throughout the year. Thus, at the beginning of the simulation, a non-zero initial value is appropriately selected for the LNG inventory, based on the pattern of this variable in subsequent days. Consequently, until there is inventory in the tank, LNG is supplied from it (LNG underproduction in Figure 5.7). Then, when electricity price is sufficiently cheap, natural gas is taken from the pipeline and stored in the LNG tank. As stated before, this is also the time when electricity demand is lower than at peak hours. Thus, LNG inventory in the tank increases (LNG overproduction in Figure 5.7) during off peak times. It is seen in Figure 5.7 that a significant amount of natural gas is imported at hours 24, 72, and 144 and the tank is completely filled up. This is because of the lower average power price at hours 24, 72, 144 than the subsequent 48 hours. After the tank is completely filled up in the early hours of the days starting at hours 24, 72, and 144, LNG is taken from the tank and the level of the tank drops until it reaches the low threshold of the tank. Unlike hours 24, 48, and 144, at the beginning of hour 120 natural gas is imported as much as it can supply LNG for only the next 24

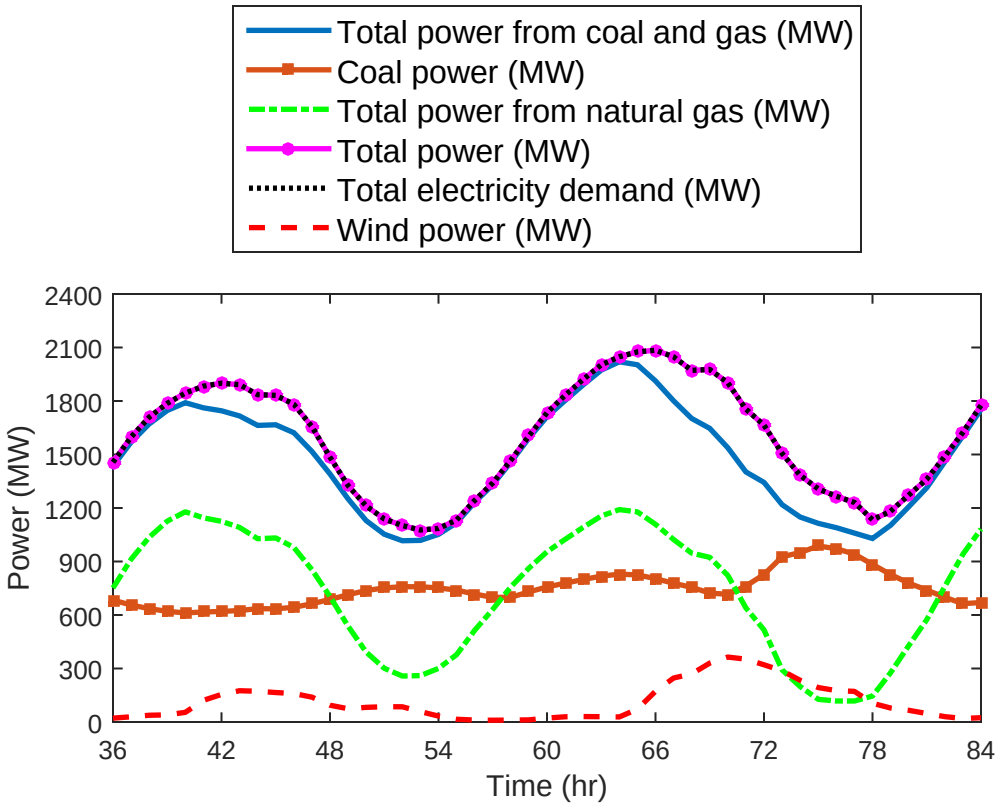

Figure 5.6: Increased value of wind power by using energy storage of the CCC

hours. Integrated wind power during the day starting at hour 120 is more than any other days in the time horizon (with respect to the integrated electricity demand). Because wind will help meet the demand, less LNG is needed in the tank in that day to supply sufficient cooling capacity through the peak. For other days, the LNG tank fills completely because of less available wind and more expensive power price.

Although the maximum power required to increase the pressure of the recirculating natural gas to the pipeline pressure is approximately 3.2 MW, it is still more economical (though not more energy efficient) to export a fraction of the more pure natural gas to the pipeline until the electricity price is comparatively low. In the cases where the export of natural gas is not considered an option, the trend of other variables remain the same but the profit obtained over the entire time horizon decreases by 16.6% when compared to cases where the export of natural gas is considered. Mixed refrigerant compressors should also remain in operation during peak hours to process natural gas that could have otherwise been exported to the pipeline. Therefore, more power should be produced

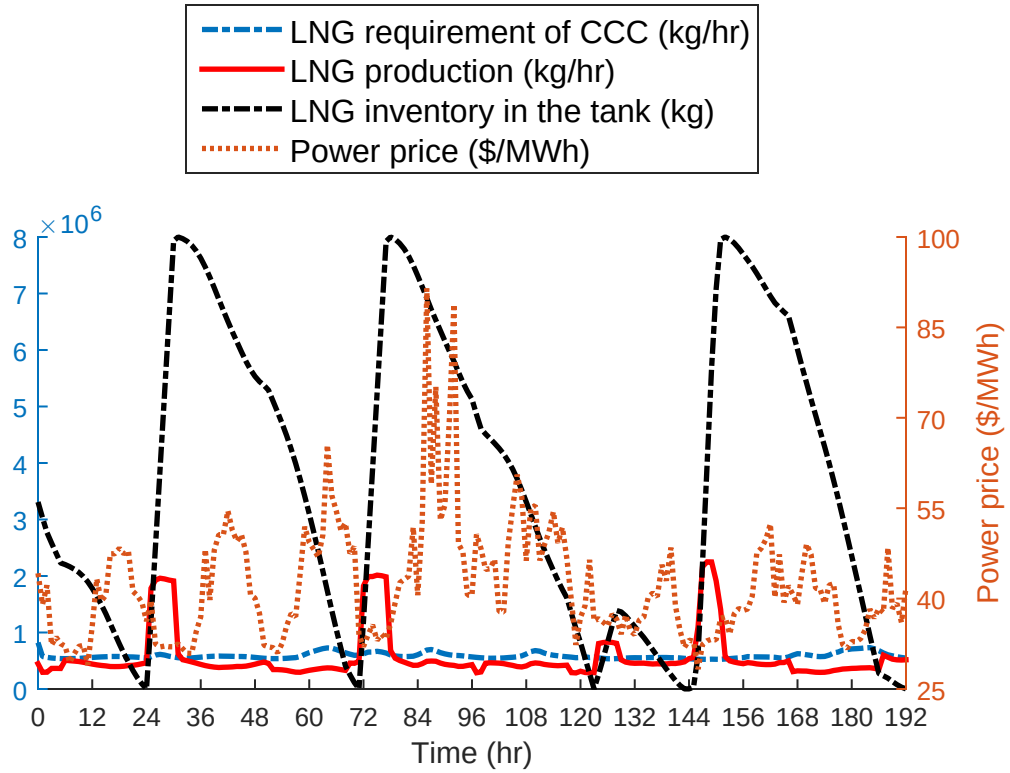

Figure 5.7: LNG inventory, LNG production, and LNG required to run the CCC vs. power price

to meet the loss of the mixed refrigerant compressor. The aforementioned facts also illustrate the advantage of using LNG as a refrigerant in the CCC process as it can be exported to the pipeline when it is vaporized in the CCC process. Vaporized LNG also serves as a fuel when it is needed to produce more power in the gas turbine.

It is also important to mention that the exported natural gas shown in Figure 5.8 starts from a non-zero value at the beginning of the simulations. Similar to the LNG inventory, the initial value of the exported natural gas is selected according to the pattern of this variable in the following days. Because the electricity price is not sufficiently low, a fraction of the vaporized LNG is exported to the pipeline. The export of natural gas continues until the electricity price reaches a low value at hour 6. However, there is still LNG inventory in the tank and the hybrid system is driven by the stored LNG until it reaches the low threshold in early hours of the next day. Depending on the power price, this general trend in LNG inventory (Figure 5.7) and natural gas imported and exported (Figure 5.8) cycles regularly. This is typical for an integrated system with

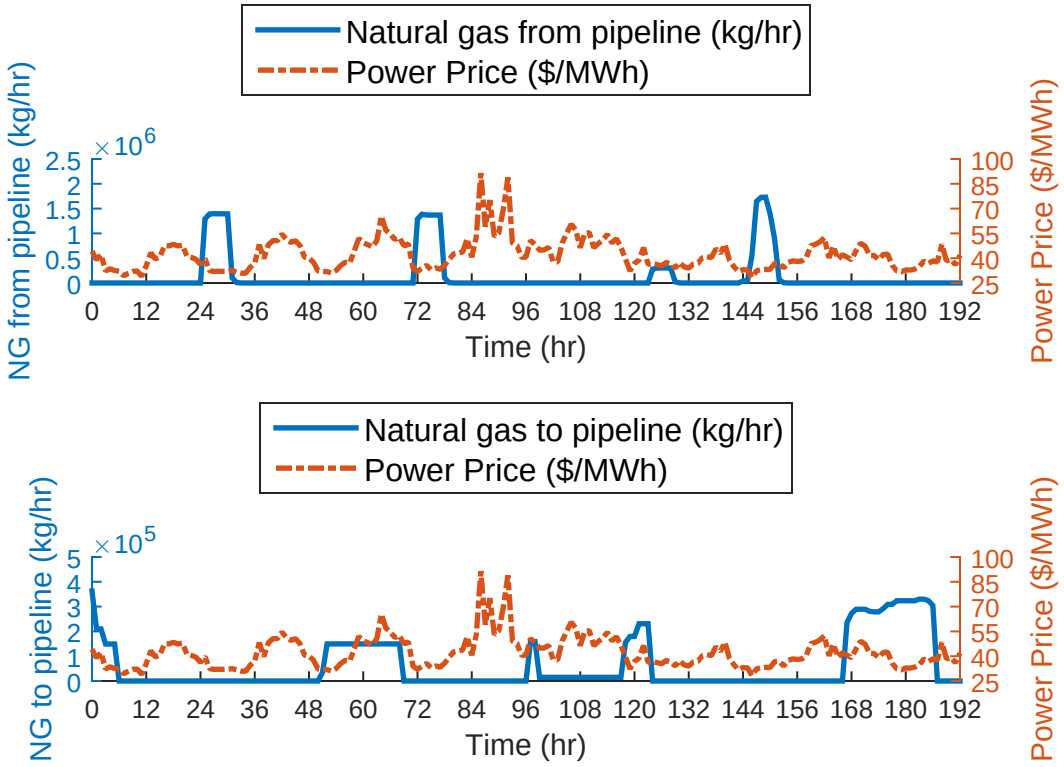

Figure 5.8: Natural gas imported and exported vs. power price

energy storage capability. This cyclical nature is based on the ongoing need for electricity which, in return, requires natural gas and LNG for flue gas treatment in the CCC process.

Electricity on-site demand curves for the main electricity consuming components of the system provide additional insight. The demand curves for the natural gas compressor, mixed refrigerant compressor, and CCC plant (Figure 5.9) illustrate the dynamics of the plant. The natural gas compressor and CCC plant depend on the residential electricity demand because more power should be produced during peak hours, which in turn produces more flue gas. Therefore, the CCC plant demand also increases during peak hours. However, Figure 5.5 shows that more power is produced from natural gas during peak hours. Because natural gas combustion emits less CO_2, less LNG is required when compared to the case where coal is combusted to meet the same amount of electricity demand. Thus, during peak hours, the natural gas compressor has lower electricity demand than in off-peak hours when coal is the main source of power production. On the other hand, the mixed refrigerant compressor demand decreases when electricity is expensive as most

of the required LNG is taken from the tank. This is the main energy storing aspect of CCC; the parasitic load associated with the CCC-based carbon capture can be partially or completely met with stored LNG. An insignificant residual flow remains to maintain spinning turbomachinery and temperature profiles. When LNG is stored in the tank and power demand is high, it is economical to curtail the mixed refrigerant compressor and transfer the saved electricity to meet the peak demand. When there is no storage tank, power should also be supplied to compensate for the loss of the mixed refrigerant compressor and to meet the LNG requirement during peak hours. A comparison between power demand of the mixed refrigerant compressor with and without energy storage is shown in Figure 5.10. The efficiency loss associated with working at a different load than the designed case in the operation of the mixed refrigerant compressor is not considered in this study and should be addressed in future work.

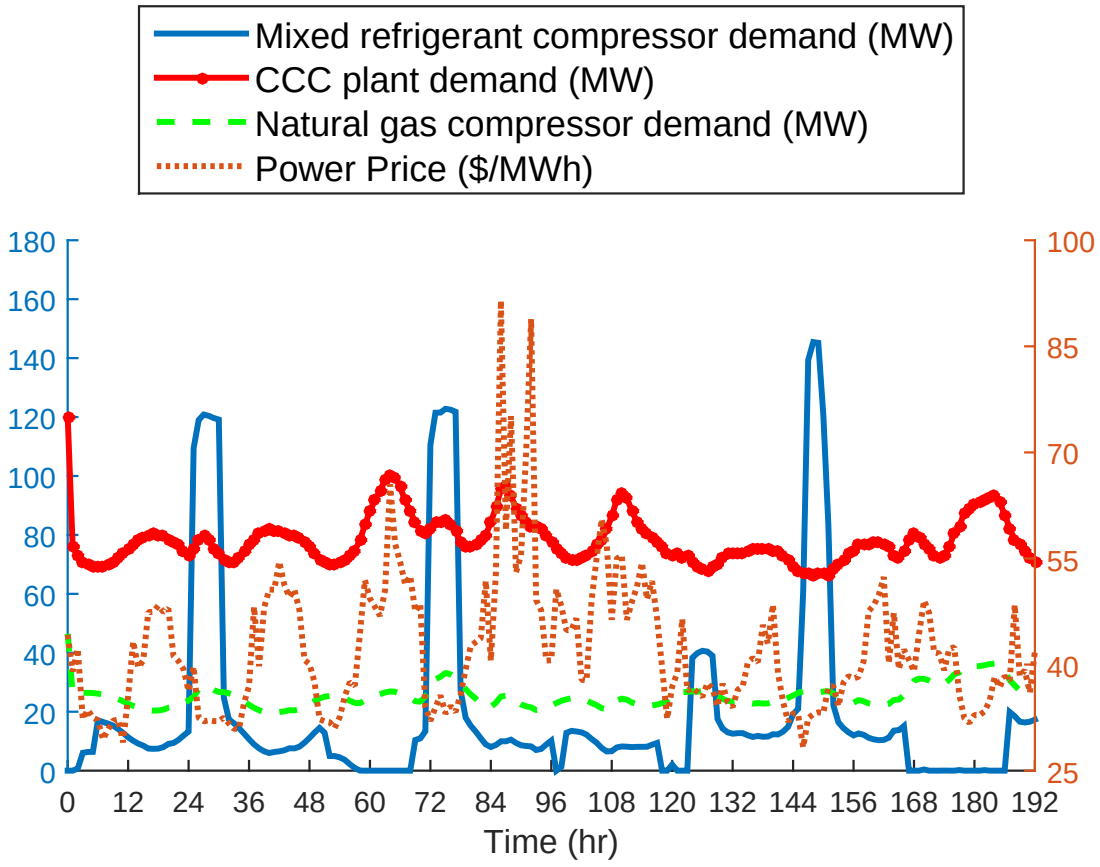

Figure 5.9: Demand curves for natural gas compressor, mixed refrigerant compressor, and CCC plant

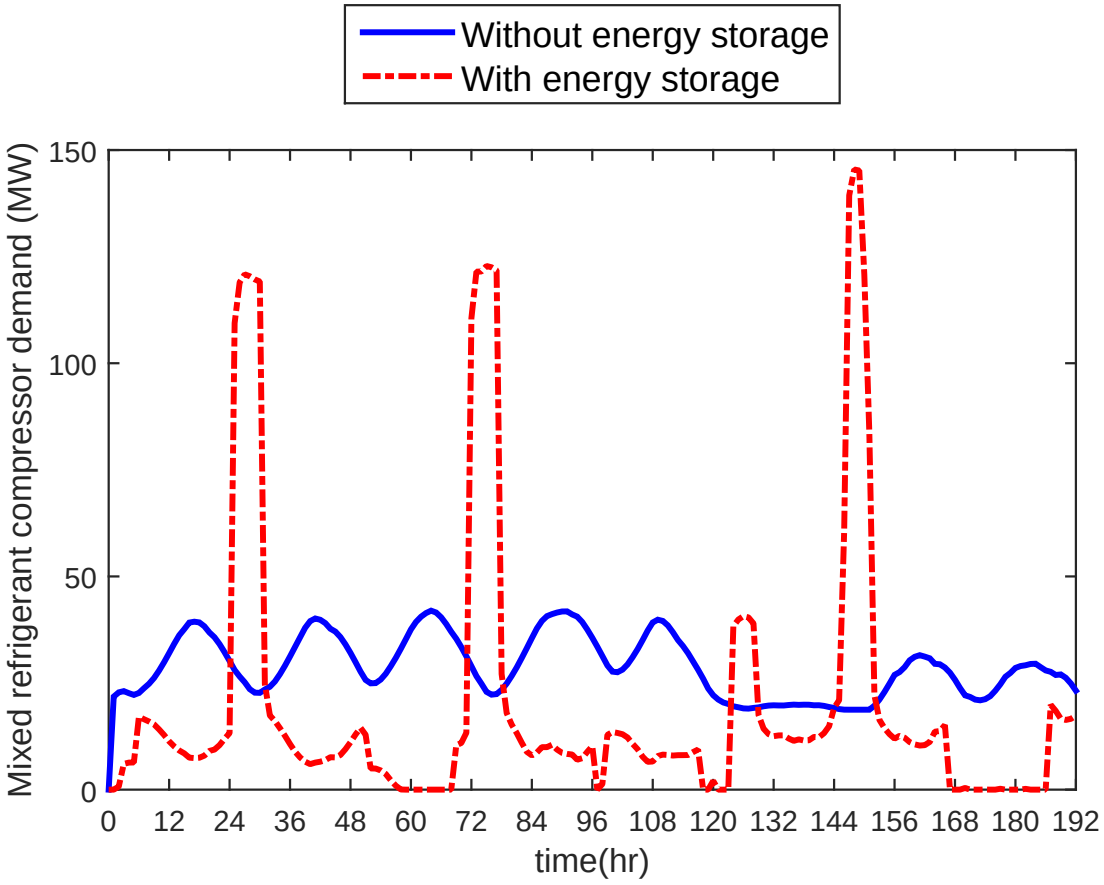

Figure 5.10: Comparison between power demand of mixed refrigerant compressor with and without energy storage

The average profit acquired from the integrated system is approximately $35k/hr. While the annual performance of the hybrid system over a longer time frame is needed, it is expected that the profit obtained from this hybrid system is sufficiently large to pay a significant fraction of the cost of construction of the cryogenic carbon capture plant. Performance of the system over a longer time horizon is the subject of future work.

5.5.1 Sensitivity Analysis

Finally, the effects of the penalization factors applied in this study ($c_{\Delta u}$ in Equation (2.5)) are investigated. Penalization factors influence the optimization outcome and are adjustable parameters to obtain simulation results that are satisfactory based on operator feedback. These factors

serve as tuning factors to the model to smooth the trend of the variation of the simulated operation. If movement penalization is not applied, large and sharp variations in the trends of variables creep into the solution with little additional benefit towards the overall objective. This movement contrasts with the desired stability of the system and highlights the need to include additional terms in the optimization problem to align simulation objectives with operational experience. However, it is important to minimize the use of penalization factors as much as possible because they impose an artificial cost to the objective function. A penalization factor is applied to the flow rate of the imported and exported natural gas. The change in the objective function for applying different penalty factors for these variables is less than 5% for one order of magnitude of variation. In other words, these penalization factors do not change the overall trend of the variables over the time horizon (not shown here), and the main effect the factors have is on the smoothness of the results. These tuning factors are adjusted in each simulation when sharp fluctuations are observed in the trend of the decision variables from initial attempts to solve the problem.

5.6 Conclusion

This chapter reports an optimization framework for the integrated system of fossil and renewable energy sources with the energy-storing version of the cryogenic carbon capture^{TM} (CCC) process. The CCC process has rapid response to the fluctuations in the electricity demand and is able to store excess energy in the form of condensed, cold refrigerant. These features enable the power grid to utilize more renewable energy sources. The objective in this chapter is to meet the total electricity demand of a residential area and the CCC process and to maximize the operating profit of the system.

Results show that a combination of coal, gas, and wind generation can be fully utilized to meet the total electricity demand. Produced CO_2 from the fossil-fueled power plants is captured at a rate of 90% while 100% of the available wind power is utilized. The sporadic wind production is effectively moved from periods of low value to the grid to periods of peak value while significantly stabilizing the grid. Off-peak excess generating capacity also moves to peak periods, increasing capital utilization and decreasing the fluctuation in boiler loads relative to the fluctuation of power demand. While the steam boiler considered in this chapter is assumed to follow the electricity demand curves in a change rate as much as 7% per minute, the maximum rate of load change in

the boiler is observed to be less than 0.1% per minute. The average profit acquired from the hybrid system is approximately $35k/hr. The performance of the integrated system for baseline steam boilers that are not able to follow the electricity demand curves is the focus of Chapter 6.

CHAPTER 6. DYNAMIC OPTIMIZATION OF A HYBRID SYSTEM OF CRYOGENIC CARBON CAPTURE AND A BASELINE POWER GENERATION UNIT

6.1 Introduction

Integration of the CCC capture process with a coal–fired steam boiler that is able to follow the load was considered in Chapters 4 and 5. However, many coal–fired generation units operate in a baseline mode and the power output from those generation units is approximately constant over most of the operational lifetime. This chapter considers the integration of a baseline coal–fired steam boiler with a cryogenic capture process. Considering energy storage, the hybrid system is also able to follow the peak demand with a gas turbine without necessarily cycling the coal–fired steam boiler. This is a distinguishing feature of this chapter from Chapter 5. Minor adjustments to the model developed in Chapters 4 and 5 make boiler output constant or load–following. This chapter quantifies boiler cycling costs and the economic benefit of their mitigation by CCC in systems with and without intermittent sources such as wind.

This chapter is divided into four sections. First, the adjustments required in the model to represent the baseline performance are discussed. Next, the optimization results obtained for an integrated system of a baseline power generation unit and the CCC process are presented. A comparison between power production in the gas turbine through a simple or combined cycle is also made. Finally, the impact of energy storage of cryogenic carbon capture on leveling the power output from a steam turbine and the associated savings are discussed.

6.2 Model Adjustment for Baseline Performance

As mentioned previously, the model developed in Chapters 4 and 5 is slightly adjusted to achieve the performance of a baseline coal–fired power generation unit. This is achieved by dedicating a large penalization factor, $c_{\Delta u}$ in Equation 2.5a, to the variation of the set point of the steam turbine power output, (P^{SP}). In this case, the steam turbine power output does not vary

unless there is an improvement in the overall objective function. In addition, the change in steam turbine power output between subsequent time steps is limited to 100 MW/hr to further restrict the variation of the power output in the steam turbine. This maximum change rate is much less than 1%/min of the nominal load–following capacity of the steam turbine.

To make the objective function more accurate, the variable and fixed operating and maintenance (VOM) costs of the the power generation units are added to the profit function developed in Equation 5.8. The variable operating and maintenance of the coal- and gas-fired power generation units are represented by VOM^{CT} and VOM^{GT} while fixed operating costs (FOM) are presented by FOM^{CT} and FOM^{GT} for the coal– and gas–fired power units, respectively. In this investigation, the same VOM and FOM costs are assumed for both power generation types and are equal to 7.3 and 10.2 dollar per MWh of energy production, respectively [166]. Thus:

$$\begin{aligned} Profit = (D^{Res} - D^{Plant})P^{E} - (NG^{PL} - NG^{EXPT})P^{N} - P^{C}C \\ -(FOM^{CT} + VOM^{CT})P^{CT} - (FOM^{GT} + VOM^{GT})P^{GT} \end{aligned} \tag{6.1}$$

The input data and other assumptions used to evaluate the performance of an integrated system with a baseline coal–fired generation unit are the same as a load–following unit discussed in Chapter 5.

6.3 Results and Discussion

The results for the integration of cryogenic carbon capture with a baseline coal–fired power plant are presented in this section. Figure 6.1 presents the total power generation in the steam turbine. For comparison, the power generation from a load-following steam turbine is also shown in Figure 6.1.

As is observed in Figure 6.1, total power generated in the steam turbine does not vary significantly for most of the simulation time. The minimum output for the steam turbine (820 MW) is close to the selected lower limit (800 MW). Because the steam turbine operates as a baseline unit, the power output from this unit does not cycle during peak hours and gas power is used instead as the peaking unit (shown in Figure 6.2). The small variations observed in the trend

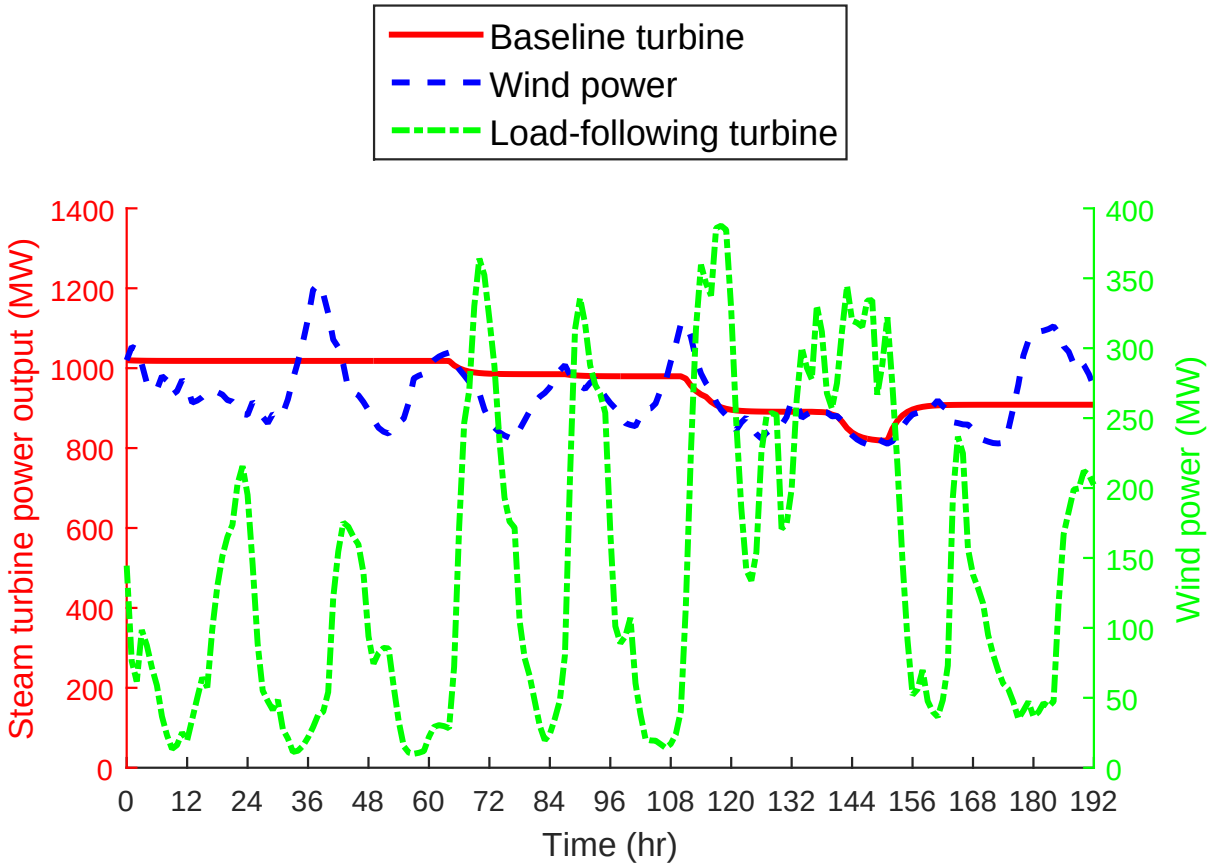

Figure 6.1: Total power generation from the steam turbine vs. wind power

of the steam turbine power output between hours 110 and 160 is because of a high penalization factor, w_{hi}, dedicated to avoid overproduction of power. When wind power is significant (for instance for the period between hours 115 to 150), power output from the steam turbine decreases a few hours before the wind power comes online with the energy storage component of the CCC process making up the difference. Thus, the cost associated with power overproduction is avoided. While this small variation is inevitable to avoid the overproduction penalization cost, the power output remains constant after the change is made as a result of the penalization cost associated with variation of power output of the steam turbine. It is also observed that after hour 156 to the end of the simulation time, wind power has a smaller contribution in meeting the electricity demand and it is found more economical to increase the power output from the steam boiler.

From Figure 6.2, it is also observed that the overall electricity demand is met through a combination of power sources. Whenever wind power is available, it is utilized first to meet the

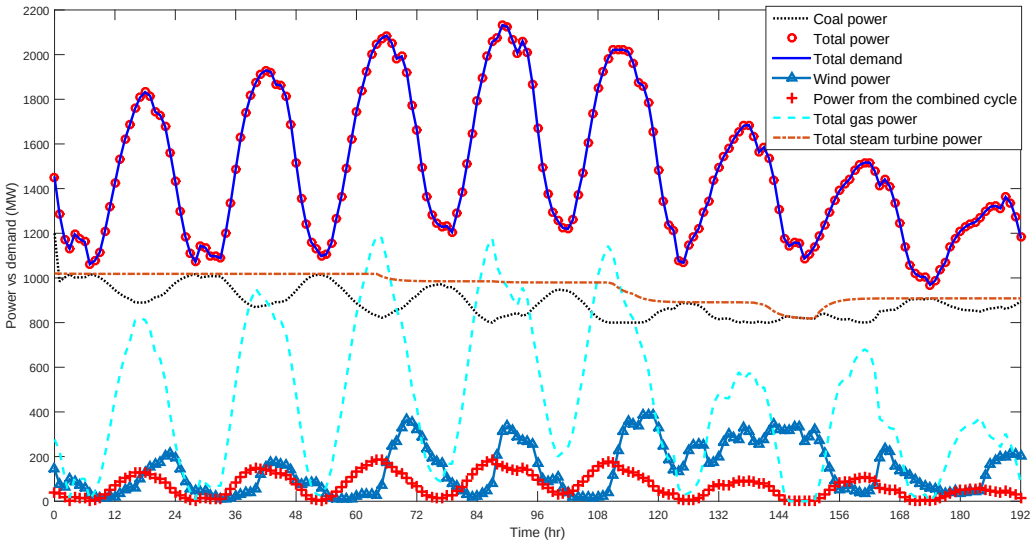

Figure 6.2: Electricity demand and power production from coal, wind, and natural gas

electricity demand while the power output of the steam turbine is mostly at a value close to the minimum residential electricity demand. Gas power is mostly produced during peak hours to meet the increasing electricity demand. This is because more LNG is required in the CCC process to treat the higher amounts of flue gas produced during these hours. As LNG from the tank produces excess natural gas inside the plant (after treating the flue gas), this natural gas could be used for power generation in the gas turbine. This is more economical than combusting coal to meet the peak demand. This finding is also compatible with the baseline nature of the steam turbine and permits the optimization problem to avoid the cycling cost of the steam turbine. Production of gas power is a direct impact of using energy storage; i.e. it permits the system to overproduce LNG refrigerant during low power demand or when wind is readily available and to drive the CCC process from the stored refrigerant. The excess warm refrigerant produced during energy recovery is either sent back into the pipeline or used as a fuel source in a gas turbine.

From Figure 6.2, it seems that a value of 1020 MW, the maximum output from the steam turbine, is reasonable to meet the combined electricity demand of the residential users and CCC plant. However, economical calculations are needed with consideration of the life time of the steam turbine and the growing need in electricity demand to accurately size it. While with the energy storage capability of the CCC process it is expected to benefit wholesale electricity prices

in a power grid, no impact on the energy price is assumed. The output results obtained from such analysis predict the required energy from each source for the following days subject to the constraints for each power source (e.g. baseline steam turbine). The impact of the energy storage on the wholesale electricity prices is outside the scope of this study.

Trends of variables for the natural gas imported and exported to the plant are shown in Figure 6.3a and are similar to the results obtained in Chapter 5. Import of natural gas to the plant is mainly observed when electricity is cheap. Export of natural gas from the plant, on the other hand, occurs when electricity is relatively expensive. This permits the system to avoid liquefying the circulating natural gas (NG^{CCC}) when demand in electricity is high. Trends of LNG inventory in the tank (Figure 6.3b) reflect an excellent transient response of this optimization problem to fluctuations in residential demand, energy price, and wind power availability. LNG inventory in the tank is dependent on the energy price, current inventory in the tank, wind power availability, and the penalization factors used for the natural gas imported to and exported from the plant. Thus, LNG inventory is a cumulative effect of these factors and is less intuitive to accurately attribute its trend to each of these factors. However, it is expected to store LNG when higher electricity price or lower wind availability are foreseen. For instance, between hours 86 and 92 when two peaks in electricity price are anticipated, LNG is stored in the tank before reaching hour 86 to be used during this period. Recovery of the LNG from the tank continues until the tank is emptied at hour 124. LNG storage is started again after hour 125; however, more wind power is available from hour 123 to 144 and the tank is not filled completely. This is because the increased availability of wind power is utilized to meet the power demand and less power is produced from the fossil fuels (consequently less CO_2 is produced). After hour 152, on the other hand, wind power is less available and it is seen that the LNG tank is fully filled before reaching hour 152. A reasonable cycling in the trend of LNG inventory is also observed after hour 152 and in the first 72 hours. These findings are also similar to the performance of the integrated system with a load–following coal–fired power plant.

While the penalization factors are used to smooth the trends of variations in natural gas to and from the plant, the overall trends for these variables and LNG inventory remain the same; i.e. a cyclical trend for the LNG inventory is observed and import and export of natural gas occur during off and on peak hours, respectively.

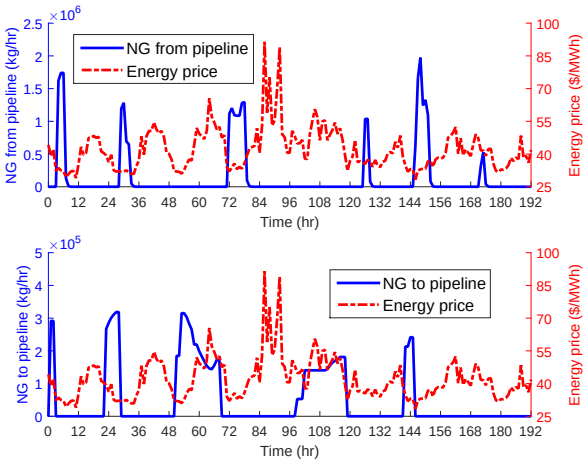

(a) Natural gas imported to and exported from the plant

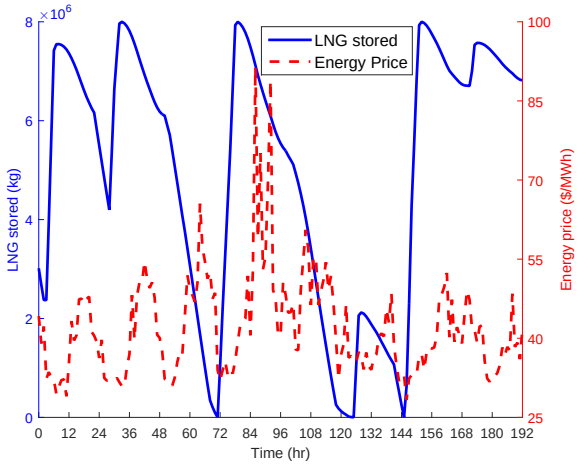

(b) LNG inventory

Figure 6.3: Trend of natural gas and LNG inventory

Trends of electricity demand for the mixed refrigerant (MR) and natural gas (NG) compressors are presented in Figure 6.4. A peak in the electricity demand of the mixed refrigerant is observed during off–peak hours that is associated with the storage case when the LNG tank is filled. The CCC process is then operated with the LNG recovered from the tank and permits the mixed refrigerant compressor to work at a minimum load when electricity is in high demand. Reduction in the electricity demand of the mixed refrigerant compressor can continue for as long as there is LNG inventory in the tank. Decisions on how long either energy storage or recovery should continue are economically-driven. As discussed in Chapter 5, inefficiency associated with working at non–optimal operating points for the compressor is not considered and the compressor is also permitted to turn on and off without any efficiency penalty. While these assumptions are acceptable to convey the energy storage concept, they should be modified when financial decisions are made. This is the focus of future work.

The average profit obtained from Equation 6.1 for a baseline steam turbine over the selected days is \$6.5k/hr. This is compared to \$13.6k/hr obtained when the power output from the steam turbine is allowed to vary without penalization. When the steam turbine is allowed to vary, penalization factor for the variation of power output, $c_{\Delta u}$ in Equation (2.5a), relaxes; thus, the hybrid system obtains a new optimum and results in an average profit of \$13.6k/hr. The ratio of total profit and total energy production from all sources considered over the simulation time is 0.43

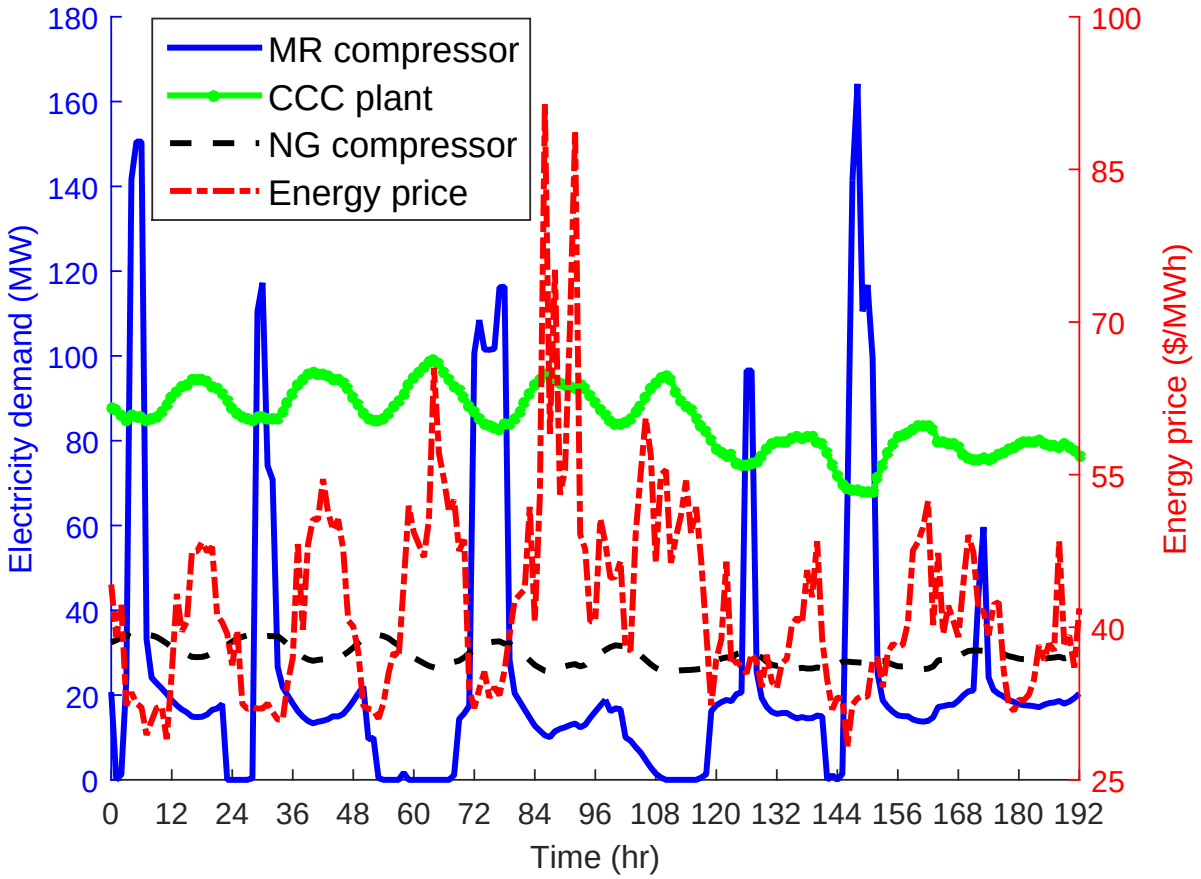

Figure 6.4: Electricity demand for refrigeration compressors and CCC plant in a combined cycle power generation unit with energy storage

¢/kWh for a baseline case while it is 0.91 ¢/kWh for a variable steam turbine. When fixed and variable operating and maintenance costs of the coal– and gas–fired power generation units (VOM and FOM) are ignored in Equation (6.1), the average profit for the baseline case is approximately \$29k/hr which is 20% less than the average profit of a load-following steam turbine (\$35.5k/hr). Similarly, the ratio of the total profit and total energy production when VOM and FOM are ignored in Equation (6.1) is 1.92 ¢/kWh and 2.40 ¢/kWh for baseline and load-following steam turbines, respectively.

6.4 Comparison Between Combined and Simple Cycles

A comparison is also made when power generation from the gas turbine is achieved in a simple cycle (scenario 1); i.e. gas turbine exhaust does not generate power. In addition, natural gas

supply for the gas turbine in scenario 1 is not the vaporized LNG exiting from the CCC process. In this case, the gas turbine serves as an independent peaking unit. However, it is still assumed that the CCC process treats the flue gas generated from the natural gas turbine. Because a simple cycle is assumed, treatment of the gas turbine exhaust is achieved by adding it to the coal exhaust after the coal superheaters and reheaters. The capacity of the gas turbine in scenario 1 is assumed the same as the analysis discussed in Section 6.3 (1000 MW). The analysis discussed in Section 6.3 is referred to as scenario 2 for the remainder of this section. In scenario 2, the baseline performance is achieved through a combination of the steam generated from the coal and natural gas flue gas; i.e. when coal power in Figure 6.2 is at a maximum, power from the combined cycle is at a minimum and the reverse trend is also observed. In scenario 1, however, the baseline performance is achieved merely from the steam generated from coal combustion (coal power). Thus, more coal is combusted in the steam boiler in a simple cycle to achieve the same steam flow rate and power output as a combined cycle. To make a fair comparison, it is assumed that the power output obtained in scenario 2 for the steam turbine, P^{ST} in Equation 4.1, is an input to scenario 1 and it is not varied; i.e. rate of steam production is the same for both scenarios. In addition, it is assumed in scenario 1 that energy storage is not available. This case represents a typical power generation unit that is equipped with a carbon capture technology (without storage capability) and a peaking unit to capture the CO_2 emissions while meeting the electricity demand.

With these assumptions, optimization of the system presented in scenario 1 is implemented and the results are compared with scenario 2. In both scenarios, power production from coal and gas is considered a single generation unit and the power supply is used to meet the electricity demand of residential users and the CCC plant. Figure 6.5a and 6.5b represent the trends of excess power production in each scenario. In scenario 1, power supply equals the electricity demand for most of the simulation time. However, both over production and under production of power occur (Figure 6.5a) despite the penalization factors applied to balance the demand and supply of electricity. For scenario 2, there is no mismatch between electricity demand and power supply over the horizon. The mismatches seen in scenario 1 stem in large part from the increased power demand on the system associated with carbon capture with no compensating increase in capacity. These would become more severe for other carbon capture systems, essentially all of which consume significantly more energy than CCC. The mismatches in scenario 1 are rare, however, when a grid

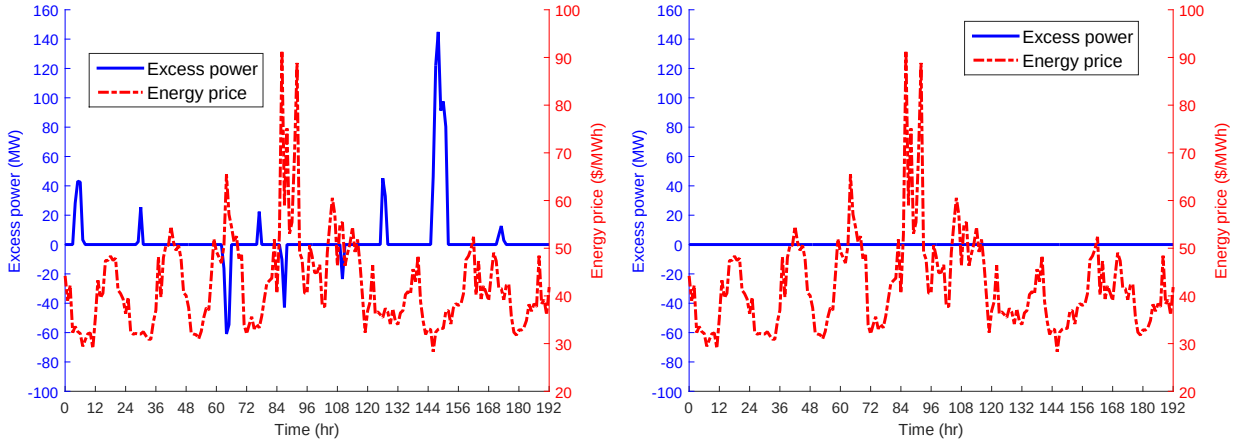

(a) Simple cycle power generation without energy storage (Scenario 1)

(b) Combined cycle power generation with energy storage (Scenario 2)

Figure 6.5: Excess power comparison between combined and simple power generation cycles with and without energy storage, respectively

analysis is implemented (due to the presence of peaking units). This comparison highlights the importance of energy storage of the CCC process. Energy storage adds flexibility to a single coal–fired generation system to operate as a baseline unit and still be able to meet the peak electricity demand without heavily relying on other generation units in the grid. This is because the hybrid system has a higher power production capacity through time–shifting of the compressor demand and the combined cycle, thereby creates less severe peaking problems comparing to other carbon capture processes.

The overall mass flow rate of the coal combusted for steam production in a system that includes natural gas in a simple cycle is 8% more than if natural gas is in a combined cycle, as expected. Total electricity consumption of the plant is also 8% more in scenario 1. This is because scenario 1 produces more flue gas from coal consumption to achieve the same steam flow rate as in scenario 2. Unlike scenario 2, the total flow rate of natural gas imported and exported to the pipeline in scenario 1 is zero because there is no opportunity for arbitrage of electricity without energy storage (Figure 6.6) and time–shifting of the electricity demand of mixed refrigerant compressor is not achievable. Thus, natural gas consumption in the simple cycle power generation unit is merely for the purpose of meeting the peak total electricity demand. In contrast, in the case of a combined cycle with energy storage, natural gas has the dual purposes of serving

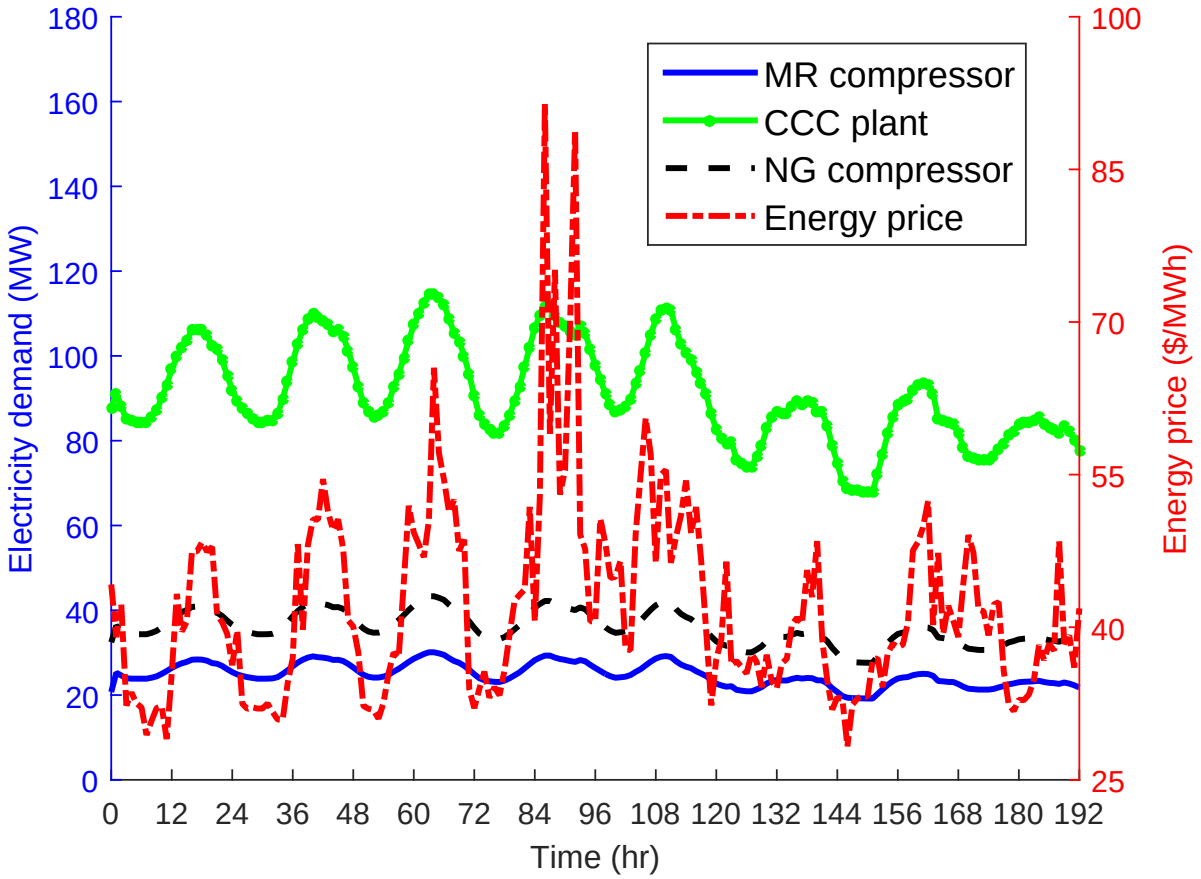

Figure 6.6: Electricity demand for refrigeration compressors and CCC plant in a simple cycle power generation unit without energy storage

as the refrigerant and a fuel. Thus, natural gas is imported and exported from the plant to take advantage of the arbitrage of electricity (Figure 6.4). A comparison between the profitability of these two scenarios is meaningless because the primary goal of meeting the electricity demand at all time steps over the horizon is not achieved in scenario 1.

6.5 Comparison of Cycling Costs

An important aspect of power plant operation is the cost associated with ramping, also known as load following or cycling. The changes in operational levels of the plant result in increased thermal, pressure, and mechanical related stress and fatigue [184, 185]. This leads to increased equipment degradation and associated operation and maintenance costs, as well as decreased thermal efficiency.

In general, research done on ramping in power plants has looked at the most fragile part of the plant, the turbine rotor. Historically unit commitment models with economic dispatch have incorporated fixed ramp-rate constraints with the assumption that ramping between the constraints will not cause damage to the turbine rotor [186, 187]. In 2012, a report published by National Renewable Energy Laboratory [173] investigated the cost of ramping for an entire plant by considering the cycling costs of several power generation types [188]. This report provides a lower bound for the cycling costs of eight types of generation units. The cycling costs are reported for different cycling scenarios including cold start, warm start, hot start, and load-following cases. Between these cycling scenarios, cold start and load-following have the highest and lowest cycling costs, respectively. For instance, the lower bound for the cold start cycling costs of a typical large-scale subcritical coal-fired power plant is \$105/MW capacity per cycle while load-following cycling cost for the same generation type is \$2.45/MW capacity per cycle [188]. While startup scenarios impose the most expensive cycling costs of the power plants, it is not the scope of this dissertation to investigate them. Consideration of such scenarios requires a longer simulation time (e.g. one year) to be taken into consideration. Instead, this analysis considers just the impact of cryogenic carbon capture on the cycling costs due to load-following of the coal- and gas-fired power generation units. According to [188], the cycling cost of a generation unit varies between individual plants and the numbers provided in this report are generic lower bounds. In this study, estimated multiplicative factors are also provided for faster ramp rate. These multiplicative factors, however, are not considered in this dissertation and the cycling costs are the median capital and maintenance costs of typical ramping rates. This investigation considers the load-following cycling costs of large–scale, subcritical coal–fired and natural gas combined cycle (NGCC) power generation units. Accordingly, the cycling cost associated with load-following of a coal–fired generation unit is \$2.45/MW capacity per cycle while it is \$0.64/MW capacity for a NGCC power plant. To calculate the number of cycles for power generation from both coal and gas, a post–processing approach is considered, i.e., power outputs from solving the optimization problem are used as input to the rainflow cycle counting algorithm [189] where the output from the algorithm is the number of cycles. This calculation assumes that power output from the optimization results has a similar trend to overall stresses in the boiler. The rainflow algorithm allows the application of Miner's rule to

assess the fatigue life of a structure subject to complex loading. More details about the rainflow algorithm are available in [190].

With the abovementioned assumptions, the cycling costs of the baseline and load–following steam turbines are considered. The power outputs from the coal– and gas– fired generation units, P^{ST} and P^{GT}, for both scenarios are used in the rainflow cycle counting software developed in [191]. Consequently, the number of cycles for the load–following scenario for the coal– and gas–fired generation units are found to be 20 and 17, respectively, over 8 days of simulation time. For a baseline scenario, there are 1 and 21 cycles in the power output from the coal– and gas–fired generation units, respectively. Optimization of the baseline and load-following coal–fired generation units result in a maximum power output of 1020 MW and 1210 MW, respectively. As mentioned previously, sizing of the generation units is beyond the scope of this dissertation and requires extensive study. However, a capacity of 1800 MW (upper bound for P^{SP}) is a good estimate for both load–following and baseline coal–fired generation unit for the purpose of cycling costs comparison. With this capacity, the cycling costs of the coal–fired unit for the load-following scenario are $1800 \times 2.45 \times 20 = \$88200$ for 8 days of simulation time while they are $1800 \times 2.45 \times 1 = \$4410$ for a baseline case study. In addition, the cycling cost of the load–following scenario for the gas–fired unit is $1000 \times 0.64 \times 17 = \$10880$ compared to a value of $1000 \times 0.64 \times 21 = \$13440$ for a baseline case over 8 days of simulation. In summary, the total costs associated with the cycling of all generation units considered in this investigation are \$99080 and \$17850 for load–following and baseline scenarios, respectively, over 8 days of simulation time. The total costs of cycling for the same power generation units in the absence of wind power are \$94100 and \$14010 for the load–following and baseline coal–fired generation unit, respectively. These costs are based on 1 and 15 cycles for the coal– and gas– fired generation units, respectively, in a baseline case while 18 and 23 cycles are observed for the the same units, respectively, in a load–following case. Table 6.1 summarizes these results.

The saving in the cycling costs of the baseline generation units, in the presence and absence of wind power, is also a direct result of the energy storage of cryogenic carbon capture. It is well–known that coal–fired generation units are mainly designed for baseline operation. Equipping the coal–fired power plant with cryogenic carbon capture enables the power generation unit, as a whole, to follow the load without necessarily varying the steam turbine output. This is achieved by

Table 6.1: Summary of cycling costs

	With wind		Without wind	
	Load-following boiler	Baseline boiler	Load-following boiler	Baseline boiler
No. Cycles in boiler (Cost)	20 ($88200)	1 ($4410)	18 ($79380)	1 ($4410)
No. Cycles in gas turbine (Cost)	17 ($10880)	21 ($13440)	23 ($14720)	15 ($9600)
Total cycling costs	$99080	$17850	$94100	$14010

supplying the natural gas required for the peaking unit from the storage system while the carbon dioxide separation from both generation units remains in operation.

It should be emphasized that these costs are the generic lower bounds for cycling of the power generation units, and they do not consider the more expensive practices of cold, warm, and hot starts. In addition, it is unlikely to have this many cycles in the boiler in 8 days to follow the load in practice (for both baseline and load–following power generation units). This is because supplemental peaking units are used to avoid the variations in power output from the coal–fired generation units. While more accurate analysis of the number of cycles requires longer simulation horizon, this study demonstrates the potential reduction in cycling costs of a coal–fired power generation unit by utilizing the energy storage of the CCC process.

6.6 Conclusion

This chapter considers dynamic integration of a baseline fossil–fueled power generation unit with cryogenic carbon capture. Similar to the integrated system with load–following capability (discussed in Chapter 5), effective time–shifting of the electricity demand of the refrigeration compressors is observed for a baseline case study. The total electricity demand of the residential users and the CCC plant is met through a combination of power sources. Wind power, whenever available, is first used in meeting the demand. This leads to 100% utilization of the wind power. With the energy storage of cryogenic carbon capture, a single coal–fired generation system is able

to operate as a baseline unit and still be able to meet the peak electricity demand. Energy storage also enables a potential 82% and 85% decrease in the costs associated with load–following of power generation units in presence and absence of wind power, respectively.

CHAPTER 7. CONCLUSION AND FUTURE WORK

7.1 Conclusion

Increasing demand of energy has motivated ongoing optimization of the new and existing technologies. In this dissertation, advanced estimation, optimization, and control techniques are applied to representative applications of large–scale and complex systems. The methods enhance the profitability and product quality while minimizing energy consumption. Moving horizon estimation and model predictive control are utilized in this study to optimize mathematical models of a batch distillation column and a hybrid system of power generation and cryogenic carbon capture. The estimation and control frameworks developed for both applications are modular and applicable to optimize complex dynamic systems. These models are nonlinear and non–convex. Several strategies are developed in Chapter 2 to initialize the nonlinear models and find a successful solution with improved computational time and convergence properties. Convergence is improved through a methodology to break a larger problem down into separate parts that can be isolated and diagnosed for convergence issues.

In Chapter 3, shortcut-based and detailed mathematical models are developed for a batch distillation column. This model utilizes a dynamic parameter estimation approach with an ℓ_1-norm objective function to fit the model prediction to experimental data. Data collection from the distillation column is achieved by applying a doublet test on the column reflux ratio and measuring the instantaneous composition and molar quantity of methanol. With dynamic parameter estimation, system non-idealities are included in the model to capture a high fidelity model response and compare it with a reduced–order model. Dynamic parameter estimation with a sensitivity analysis reduces the experimental data requirement from the column by identifying key parameters for identification. The accuracy of the estimated parameters is verified by implementing a nonlinear statistical analysis. The results predicted by the reduced–order model developed in this dissertation match the experimental data and the results obtained from a more rigorous first–principles model.

The solution time of the simplified model is, however, 5-10 times faster than the first-principles model. Faster solution time of the model is desirable in real-time control and online optimization applications. The verified model is then used to optimize the column operation by manipulating the column reflux ratio. Similar to the estimation analysis, an ℓ_1-norm objective function is utilized for column optimization. With dynamic optimization of the column, a 14% increase in methanol production is observed while the product composition meets the final purity requirements. Without measurement feedback, the predictions from the optimization analysis match the experimental data with a maximum error of 10% and 0.8% for overall methanol production and composition, respectively.

In a second application of the methodology for large–scale and complex systems, an optimization framework for a hybrid system of power generation and the CCC process is developed. The CCC process considered in this investigation is a novel technology for CO_2 removal from the flue gases of fossil–fuel power plants. Benefits are lower energy consumption, rapid response to fluctuations in demand, increased adoption of intermittent power supplies, and grid–scale energy storage capability. This study considers the dynamic integration of a simulated coal–fired power plant with cryogenic carbon capture for the first time. In this dissertation, data provided by the Sustainable Energy Solutions for energy demands, response times, and energy storing capabilities is used to analyze the impact of the CCC process on the power grid. The two main goals of this analysis are: (1) meet the total electricity demand and (2) maximize the operational profit of the hybrid system while capturing 99.9% of the CO_2. The modeling framework developed in this dissertation is modular; i.e. different capture processes, energy storage, and power generation units can be considered in this framework to explore several adoption and integration scenarios that lead to increased grid stability and full utilization of renewable sources. Three main case studies are considered for the hybrid system: (1) a load–following boiler without energy storage, (2) a load–following boiler with energy storage, and (3) a baseline boiler with energy storage. The analysis for a baseline boiler with natural gas peaking turbines addresses the operation of older designs of coal–fired power generation units while operation of recently designed coal power plants is highlighted in the load–following boiler analysis.

For the case study without energy storage, it is shown that power demand is always met through a combination of coal, gas, and wind power (for both summer and winter case studies).

For the winter case, wind power is more readily available and it has a stronger contribution to the total electricity demand. However, because of the high fluctuations in wind power availability, gas power is favored relative to the summer case. This is because of the rapid response of the gas power to make up for the intermittent behavior of wind power. Increased production of power from the natural gas in winter case requires more fuel that should be imported from the pipeline. Consequently, 100% increase in the overall intake of natural gas for the winter case, in comparison to the summer case, is observed. The overall production of LNG as stored refrigerant for the CCC process decreases by 80% in the winter case. This is because the higher share of power production from wind and natural gas reduces the total CO_2 production. Thus, less refrigerant is required for flue gas treatment. The average operational profits for the summer and winter case studies are \$21k/hr and \$13k/hr. The higher profit obtained in the summer case is attributed to the larger variation in the electricity price than the winter case. A sensitivity analysis for the impact of wind power adoption in meeting the demand is a novel contribution of this work. With an increase in the adoption rate of wind power, power production from coal decreases while power generation from natural gas increases. The trade-off between a decrease in coal consumption and an increase in natural gas consumption results in a maximum in the trend of profitability with respect to wind adoption rate; i.e. at a value of $\alpha = 0.66$, the profit of the hybrid system without energy storage is at a maximum. This observation remains valid for a range of natural gas and coal prices.

Energy storage significantly improves the performance of a hybrid system. When energy storage is included, import of natural gas shifts to time periods with a low electricity price. This also causes a peak in the LNG production (and electricity demand of the refrigeration compressor) to shift to these time periods. The LNG produced in excess during these times accumulates in an insulated vessel and is utilized when electricity demand and price are high. This curtails the electricity demand of the refrigeration compressor during peak–hours. Export of natural gas to the supply pipeline during peak hours further reduces the demand of the refrigeration compressor. Effective time–shifting of this compressor work (and LNG inventory in the tank) occurs for both load–following and baseline scenarios. This work also demonstrates the enhanced contribution of wind power by utilizing large-scale energy storage of the CCC process. A profit of \$35.5k/hr and \$29k/hr is obtained from optimization of the load–following and baseline power plants, respectively (ignoring the FOM and VOM costs). These profits are equivalent to 2.4 ¢/kWh and 1.92

¢/kWh for the load–following and baseline power plants, respectively. The profit obtained from dynamic optimization of the hybrid system can pay a significant fraction of the cost of construction and operation of the cryogenic carbon capture plant, the latter being estimated at 2.5-3 ¢/kWh.

Similar to the case without energy storage, total power demand is met through a combination of power sources. In all scenarios, wind power is utilized first to meet the electricity demand. Gas power is mainly produced during peak hours or when wind varies significantly. The fuel supply for the gas turbine is either from the pipeline (without energy storage) or when an LNG storage tank is available. Coal remains the main source of power production in this hybrid system.

A comparison is also made between the operation of a combined cycle and a simple cycle power generation unit. In the simple cycle, the gas turbine operates as an independent peaking unit and the fuel supply for the turbine is not from energy storage (unlike the combined cycle). While the rate of steam production is assumed the same for both scenarios, energy storage is not considered in the simple cycle scenario. Thus, the simple cycle represents a typical coal–fired power plant that is equipped with a carbon capture process without energy storage. Optimization results show that when energy storage is not considered, significant mismatches between power production and demand occur throughout 8 days of simulation time. This highlights the importance of energy storage of the CCC process. With energy storage, the hybrid power generation unit is capable of producing more power during peak hours, thereby the CCC process creates less severe peaking problems comparing to other carbon capture processes.

Total cycling costs of all generation units potentially decreases by 82-85% with baseline operation. Equipping the power generation unit with large–scale energy storage of the CCC process stabilizes the baseline production. It enables the hybrid system to follow the load while CO_2 capture remains in operation and the output power of steam turbines do not vary significantly.

7.2 Future Work

Several future contributions are needed to further enhance capabilities to solve large–scale and complex dynamic systems. One important area is the development of mixed–integer nonlinear programming solvers to achieve faster solution times and higher success rates in finding a solution (or to quickly identify infeasible problems). In addition to enhanced algorithm development, sev-

eral innovations are proposed for batch distillation and integrated energy systems in the following two sections.

7.2.1 Batch Distillation Column

The model developed for the batch distillation column is optimized in an offline mode. Application of the model for online optimization of the column would improve performance by utilizing measurement feedback to continually correct model predictions and re–plan the batch reflux ratio profile. A nonlinear confidence interval for ℓ_1-norm objectives has not been fully developed because the F–statistic is based on the ratio of χ^2 distributions. The χ^2 distributions are currently only for squared error objectives. Application of this approach for advanced column designs such as a cyclic distillation column is another potential direction for future work.

7.2.2 Hybrid System of Power Generation and the CCC Process

The effects of equipment capital cost in the economic evaluation of the integrated system are not considered in this investigation. Considering capital costs of the equipment in economic evaluation of the hybrid system requires a longer simulation horizon. This issue should be addressed in future work because sizing of equipment influences the dynamic operation and overall profitability. In addition, operation of the refrigeration compressor at different operating points is assumed to have the same efficiency. The efficiency loss due to operation at non–optimal points is the focus of future work. Additionally, compressors have finite turndown ratios and a minimum flow is typically circulated in the compressor to avoid shutting down the compressor completely. This should be added to the model in future analysis. Moreover, there is a significant cost associated with operating a boiler at a power output less than its designed capacity. For example, cyclic operation of a boiler is an instance that leads to a lower capacity utilization. This results in an increase in the average cost of power generation. Considering the impact of operating the boiler at a reduced power output on the cost of power generation is the focus of future work. Additionally, not all natural gas is suitable for LNG storage. The CO_2 content of natural gas might be higher than the LNG production standards. The CCC process can also be used to reduce the CO_2 content from the pipeline natural gas. The natural gas processing facility is discussed in details

in [192–194]. Integration of the natural gas processing facility with the hybrid system of power plant and the CCC process is another direction for future work. Further future directions include investigating the impact of the recirculation system on the flue gas exhaust from coal and gas–fired power plants, quantifying the impact of the energy storage on the wholesale electricity prices, considering the more expensive start–up scenarios on cycling costs of the power plants, and exploring the uncertainty in prices and wind data.

The impact of cryogenic carbon capture along with the associated energy storage is considered on a single power generation unit. The energy storage of the CCC process can positively impact the stability of the power grid. In current power grid systems, stability and reliability of the grid depend in part on the individual unit availability and in part on spinning reserves. Spinning reserves are typically operated when there is a sudden increase in electricity demand or when some other generation unit unexpectedly goes off line. Because this only occasionally happens, spinning reserves typically have very low capacity factors, which in turn leads to very high average cost of power generation. The cost of power generation as a function of the cumulative grid operating capacity forms a dispatch curve similar to Figure 7.1 with the low capacity-factor systems typically having the highest costs [195]. The cost curve is highly nonlinear with peaking plant sources. What the figure does not illustrate is that some amount of spinning reserve is always online, regardless of the overall grid demand. Therefore, the rapid increase in cost of power for the last increment of capacity will always exist, regardless of the power demand. The systems represented by this section of the curve generally only operate during high or sudden increase in power demand. This gives rise to significant changes in the cost of power generation from low to high demand periods. These differences are an inherent part of any highly reliable grid that integrates several individual power sources. The energy storage portion of CCC, however, can effectively become the grid spinning reserve by adjusting the parasitic load of the compressors in time to accommodate the dispatch schedule of the grid. This energy storage capacity will essentially always have significant economic benefit on a grid. Simulation of a larger power grid with fossil-fueled units equipped with CCC is the scope of future work.

Additionally, the abovementioned optimization framework for the power grid should be implemented in an actual dispatch control center for a grid. This framework is required to consider real-time updating of the model with respect to operational changes or disturbances in the grid.

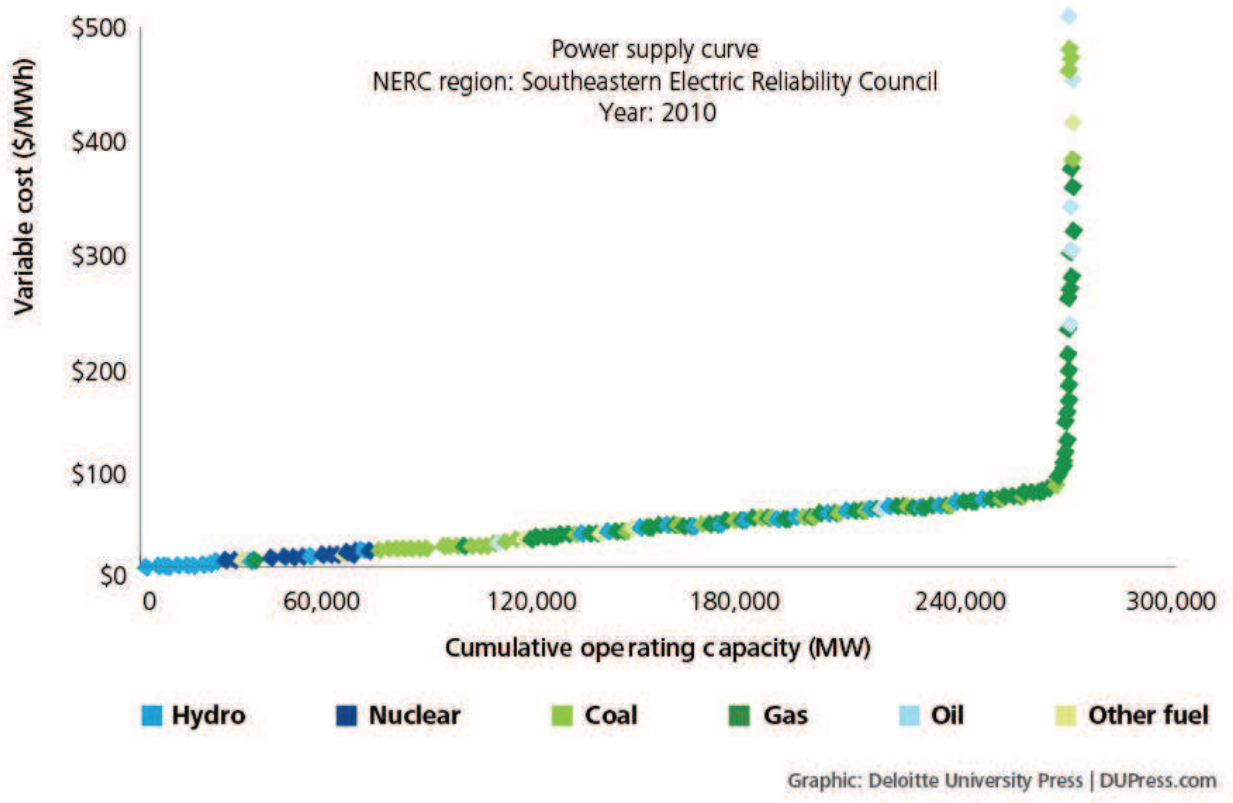

Figure 7.1: Power supply curve for Southeastern Electric Reliability Council region [195]

This is especially important for unpredictable upsets in the grid such as the shut down of a power plant on the grid. This requires addition of more robust optimization algorithms, utilization of warm-start initialization strategies, and usage of more computational resources.

7.3 Publications

The main contributions of this dissertation are presented in several journal papers and conferences and they are listed below:

- **Safdarnejad**, S.M., Hedengren, J.D., Baxter, L.L., Dynamic Optimization of a Hybrid System of Energy–Storing Cryogenic Carbon Capture and a Baseline Power Generation Unit, Applied Energy Journal, Volume 172, Pages 66-79 (Chapters 4 and 6)

- **Safdarnejad**, S.M., Gallacher, J, Hedengren, J.D., Dynamic Parameter Estimation and Optimization for Batch Distillation, Computers and Chemical Engineering Journal, Volume 86, Pages 18-32 (Chapter 3).

- **Safdarnejad**, S.M., Hedengren, J.D., Lewis, N.R., Haseltine, E., Initialization Strategies for Optimization of Dynamic Systems, Computers and Chemical Engineering Journal, Volume 78, Pages 39-50 (Chapter 2).

- **Safdarnejad**, S.M., Hedengren, J.D., Baxter, L.L., Plant-level Dynamic Optimization of Cryogenic Carbon Capture with Conventional and Renewable Power Sources, Applied Energy Journal, Volume 149, Pages 354-366 (Chapter 5).

- **Safdarnejad**, S.M., Kennington, L., Hedengren, J.D., Baxter, L.L., Investigating the Impact of Cryogenic Carbon Capture on the Performance of Power Plants, American Control Conference (ACC), Chicago, IL, July 2015 (Chapter 4).

- **Safdarnejad**, S.M., Richards, J., Griffiths, J., Hedengren, J.D., Baxter, L.L., Increased Stability of a Power Grid by Energy Storage of Cryogenic Carbon Capture, AIChE Spring Meeting, Houston, TX, Apr. 2016 (Chapter 6).

- **Safdarnejad**, S.M., Gallacher, J. R., Hedengren, J.D., A New Framework for Dynamic Parameter Estimation and Optimization of Batch Distillation Columns, AIChE National Meeting, Salt Lake City, UT, Nov. 2015 (Chapter 3).

- **Safdarnejad**, S.M., Hedengren, J.D., Baxter, L.L., Reduction in Cycling of the Boilers by Using Large-Scale Energy Storage of Cryogenic Carbon Capture, AIChE National Meeting, Salt Lake City, UT, Nov. 2015 (Chapter 6).

- **Safdarnejad**, S.M., Hedengren, J.D., Baxter, L.L., Dynamic Optimization of the Hybrid System of a Baseline Power Generation Unit and Cryogenic Carbon Capture, Western States Section of the Combustion Institute, Provo, UT, Oct. 2015 (Chapter 6).

- **Safdarnejad**, S.M., Hedengren, J.D., Baxter, L.L., Effect of Cryogenic Carbon Capture (CCC) on Smart Power Grids, AIChE Spring Meeting, Austin, TX, Apr. 2015 (Chapter 6).

- **Safdarnejad**, S.M., Hall, T., Hedengren, J.D., Baxter, L.L., Dynamic Optimization of Cryogenic Carbon Capture with Large-scale Adoption of Renewable Power, AIChE National Meeting, Atlanta, GA, Nov. 2014 (Chapter 5).

Bibliography

[1] Manenti, F., Lima, N. M., Lian, L. Z., Cuoci, A., and Frassoldati, A., 2010. "Generalized classes for lower levels of supply chain management: Object-oriented approach." In *20th European Symposium on Computer Aided Process Engineering*, S. Pierucci and G. B. Ferraris, eds., Vol. 28 of *Computer Aided Chemical Engineering*. Elsevier, pp. 139 – 144. 9

[2] Buzzi-Ferraris, G., and Manenti, F., 2014. *Differential and Differential-Algebraic Systems for the Chemical Engineer: Solving Numerical Problems*. Wiley, New York. 9

[3] Sun, L., Hedengren, J. D., and Beard, R. W., 2014. "Optimal trajectory generation using model predictive control for aerially towed cable systems." *Journal of Guidance, Control, and Dynamics,* **37**(2), pp. 525–539. 9, 31, 42

[4] Kumar, A., and Daoutidis, P., 1999. *Control of nonlinear differential algebraic equation systems*. Chapman & Hall/CRC, New York. 9

[5] Biegler, L. T., 2007. "An overview of simultaneous strategies for dynamic optimization." *Chemical Engineering and Processing: Process Intensification,* **46**(11), pp. 1043 – 1053. 9

[6] Biegler, L., Campbell, S., and Mehrmann, V., 2012. *Control and Optimization with Differential-Algebraic Constraints*. SIAM - Society for Industrial and Applied Mathematics, Philadelphia. 9

[7] Carey, G., and Finlayson, B., 1975. "Othogonal collocation on finite elements." *Chemical Engineering Science,* **30**, pp. 587–596. 9

[8] Renfro, J., Morshedi, A., and Asbjornsen, O., 1987. "Simultaneous optimization and solution of systems described by differential/algebraic equations." *Computers and Chemical Engineering,* **11**(5), pp. 503 – 517. 9, 42

[9] Liebman, M., Edgar, T., and Lasdon, L., 1992. "Efficient data reconciliation and estimation for dynamic processes using nonlinear programming techniques." *Computers and Chemical Engineering,* **16**, pp. 963–986. 9

[10] Albuquerque, J. S., and Biegler, L. T., 1995. "Decomposition algorithms for on-line estimation with nonlinear models." *Computers and Chemical Engineering,* **19**, pp. 1031–1039. 9

[11] Cervantes, A., and Biegler, L., 1998. "Large scale DAE optimization using simultaneous nonlinear programming formulations." *SIAM Journal on Numerical Analysis,* **44**(5), pp. 1038–1050. 9

[12] Hong, W., Wang, S., Li, P., Wozny, G., and Biegler, L., 2006. "A quasi-sequential approach to large-scale dynamic optimization problems." *AIChE Journal,* **52**, pp. 255–268. 9

[13] Míguez, J., 2010. "Analysis of a sequential monte carlo method for optimization in dynamical systems." *Signal Processing,* **90**(5), May, pp. 1609–1622. 9

[14] Binder, T., Blank, L., Bock, H., Burlisch, R., Dahmen, W., Diehl, M., Kronseder, T., Marquardt, W., Schlöder, J., and Stryk, O., 2001. *Online Optimization of Large Scale Systems*. Springer-Verlag Berlin Heidelberg, ch. Introduction to model based optimization of chemical processes on moving horizons, pp. 295–339. 9

[15] Diehl, M., Bock, H. G., Schlöder, J. P., Findeisen, R., Nagy, Z., and Allgöwer, F., 2002. "Real-time optimization and nonlinear model predictive control of processes governed by differential-algebraic equations." *Journal of Process Control,* **12**, pp. 577–585. 9

[16] Assassa, F., and Marquardt, W., 2014. "Dynamic optimization using adaptive direct multiple shooting." *Computers and Chemical Engineering,* **60**(0), pp. 242 – 259. 9

[17] Leppävuori, J. T., Domach, M. M., and Biegler, L. T., 2011. "Parameter estimation in batch bioreactor simulation using metabolic models: Sequential solution with direct sensitivities." *Industrial and Engineering Chemistry Research,* **50**(21), pp. 12080–12091. 9, 42

[18] Brenan, K. E., Campbell, S. L., and Petzold, L. R., 1996. *Numerical solution of initial-value problems in differential-algebraic equations*., Vol. 14 SIAM. 10

[19] Ascher, U. M., and Petzold, L. R., 1998. *Computer methods for ordinary differential equations and differential-algebraic equations*., Vol. 61 SIAM. 10, 22

[20] Petzold, L. R., 1982. Description of dassl: A differential/algebraic system solver Tech. rep., Sandia National Labs., Livermore, CA (USA). 10

[21] Hindmarsh, A. C., Brown, P. N., Grant, K. E., Lee, S. L., Serban, R., Shumaker, D. E., and Woodward, C. S., 2005. "SUNDIALS: Suite of nonlinear and differential/algebraic equation solvers." *ACM Transactions on Mathematical Software,* **31**(3), pp. 363–396. 10

[22] Cizniar, M., Salhi, D., Fikar, M., and Latifi, M., 2005. "A MATLAB package for orthogonal collocations on finite elements in dynamic optimisation." In *Proceedings of the 15th Int. Conference Process Control '05*. 10

[23] Houska, B., Ferreau, H. J., and Diehl, M., 2011. "ACADO toolkit - An open-source framework for automatic control and dynamic optimization." *Optimal Control Applications and Methods,* **32**, pp. 298–312. 10

[24] Piela, P., Westerberg, A., Westerberg, K., and Epperly, T., 1991. "ASCEND: an object-oriented computer environment for modeling and analysis: The modeling language." *Computers and Chemical Engineering,* **15**, pp. 53–72. 10

[25] Tummescheit, H., Gäfvert, M., Bergdahl, T., Årzén, K.-E., and Åkesson, J., 2010. "Modeling and optimization with Optimica and JModelica.org Languages and tools for solving large-scale dynamic optimization problems." *Computers and Chemical Engineering,* **34**, pp. 1737–1749. 10

[26] Simon, L., Nagy, Z., and Hungerbuehler, K., 2009. *Nonlinear Model Predictive Control*. Lecture Notes in Control and Information Sciences. Springer-Verlag Berlin Heidelberg, ch. Swelling Constrained Control of an Industrial Batch Reactor Using a Dedicated NMPC Environment: OptCon, pp. 531–539. 10

[27] Nagy, Z., Mahn, B., Franke, R., and Allgöwer, F., 2007. "Evaluation study of an efficient output feedback nonlinear model predictive control for temperature tracking in an industrial batch reactor." *Control Engineering Practice,* **15**(7), pp. 839–850. 10

[28] Safdarnejad, S. M., Hedengren, J. D., Lewis, N. R., and Haseltine, E. L., 2015. "Initialization strategies for optimization of dynamic systems." *Computer and Chemical Engineering,* **78**, pp. 39 – 50. 10, 14

[29] Hedengren, J. D., 2015. APMonitor Modeling Language and Optimization Suite URL http://APMonitor.com. 11, 75, 97

[30] Vu, Q. D., and Li, P., 2010. "A reduced-space interior-point quasi-sequential approach to nonlinear optimization of large-scale dynamic systems." In *IEEE RIVF International Conference on Computing and Communication Technologies, Research, Innovation, and Vision for the Future*, pp. 1–6. 11

[31] Bonami, P., Biegler, L., Conn, A., Cornuejols, G., Grossmann, I., Laird, C., Lee, J., Lodi, A., Margot, F., N.Sawaya, and Waechter, A., 2005. An algorithmic framework for convex mixed integer nonlinear programs Tech. rep., IBM Research Report RC23771. 14

[32] Sahinidis, N. V., 1996. "BARON: A general purpose global optimization software package." *Journal of Global Optimization,* **8**(2), pp. 201–205. 14

[33] Hedengren, J. D., Mojica, J., Cole, W., and Edgar, T., 2012. "APOPT: MINLP Solver for Differential Algebraic Systems with Benchmark Testing." In *Proceedings of the INFORMS Annual Meeting (2012)*. 14, 26, 31

[34] Byrd, R. H., Nocedal, J., and Waltz, R. A., 2006. "KNITRO: An integrated package for nonlinear optimization." In *Large Scale Nonlinear Optimization, 35–59, 2006*, Springer Verlag, pp. 35–59. 14

[35] Hedengren, J. D., Asgharzadeh Shishavan, R., Powell, K. M., and Edgar, T. F., 2014. "Nonlinear modeling, estimation and predictive control in APMonitor." *Computers and Chemical Engineering,* **70**, pp. 133 – 148. 15, 16, 17, 29, 51, 76

[36] Safdarnejad, S. M., Hedengren, J. D., and Baxter, L. L., 2015. "Plant-level dynamic optimization of cryogenic carbon capture with conventional and renewable power sources." *Applied Energy,* **149**, pp. 354 – 366. 15, 16, 70, 71, 75, 80, 92

[37] Hedengren, J. D., and Eaton, A. N., 2015. "Overview of estimation methods for industrial dynamic systems." *Optimization and Engineering*, pp. 1 – 24, . 16

[38] Abbott, C. S., Haseltine, E. L., Martin, R. A., and Hedengren, J. D., 2012. "New capabilities for large-scale models in computational biology." In *AIChE National Meeting*. 18

[39] Hedengren, J., 2012. "APMonitor modeling language for mixed-integer differential algebraic systems." In *Computing Society Session on Optimization Modeling Software: Design and Applications, INFORMS National Meeting*. 18

[40] Wang, Y., and Boyd, S., 2010. "Fast Model Predictive Control Using Online Optimization." *IEEE Transactions on Control Systems Technology,* **18**(2), pp. 267–278. 18

[41] Hallac, B., Kayvanloo, K., Hedengren, J., Hecker, W., and Argyle, M., 2015. "An Optimized Simulation Model for Iron-Based Fischer-Tropsch Catalyst Design: Transfer Limitations as Functions of Operating and Design Conditions." *Chemical Engineering Journal,* **263**, pp. 268–279. 19

[42] Domahidi, A., Zeilinger, M. N., Morari, M., and Jones, C. N., 2011. "Learning a feasible and stabilizing explicit model predictive control law by robust optimization." *IEEE Conference on Decision and Control and European Control Conference*, pp. 513–519. 20

[43] Ferreau, H. J., Bock, H. G., and Diehl, M., 2008. "An online active set strategy to overcome the limitations of explicit MPC." *International Journal of Robust and Nonlinear Control,* **18**, pp. 816–830. 20

[44] Bemporad, A., 2003. "Multiparametric nonlinear integer programming and explicit quantized optimal control." In *Proceedings of the 42nd IEEE Conference on Decision and Control*, pp. 3167–3172. 20

[45] Bemporad, A., and Filippi, C., 2003. "Suboptimal explicit RHC via approximate multiparametric quadratic programming." *Journal of Optimization Theory and Applications,* **117**(1), pp. 9–38. 20

[46] Borrelli, F., Baotic, M., Bemporad, A., and Morari, M., 2001. "Efficient on-line computation of explicit model predictive control." In *Proceedings of the 40th IEEE Conference on Decision and Control*, pp. 1187–1192. 20

[47] Grancharova, A., and Johansen, T., 2002. "Approximate explicit model predictive control incorporating heuristics." In *2002 IEEE International Symposium on Computer Aided Control System Design Proceedings*, pp. 92–97. 20

[48] Johansen, T., 2004. "Approximate explicit receding horizon control of constrained nonlinear systems." *Automatica,* **40**, pp. 293–300. 20

[49] Sakizlis, V., Dua, V., Perkins, J., and Pistikopoulos, E., 2004. "Robust model-based tracking control using parametric programming." *Computers and Chemical Engineering,* **28**, pp. 195–207. 20

[50] Tondel, P., Johansen, T., and Bemporad, A., 2003. "An algorithm for multi-parametric quadratic programming and explicit mpc solutions." *Automatica,* **39**, pp. 489–497. 20

[51] Pannocchia, G., Rawlings, J. B., and Wright, S. J., 2007. "Fast, large-scale model predictive control by partial enumeration." *Automatica,* **43**(5), pp. 852–860. 20

[52] Ramamurthi, Y., Sistu, P., and Bequette, B., 1993. "Control-relevant dynamic data reconciliation and parameter estimation." *Computers and Chemical Engineering,* **17**(1), pp. 41–59. 20

[53] Hedengren, J., and Edgar, T., 2006. "Moving horizon estimation - the explicit solution." In *Proceedings of Chemical Process Control (CPC) VII Conference*. 20

[54] Darby, M., and Nikolaou, M., 2007. "A parametric programming approach to moving-horizon state estimation." *Automatica,* **43**(5), pp. 885–891. 20

[55] Lambert, R., Nascu, I., and Pistikopoulos, E., 2013. "Simultaneous reduced order multi-parametric moving horizon estimation and model predictive control." *Dynamics and Control of Process Systems,* **10**(1), pp. 267–278. 20

[56] Haseltine, E. L., and Rawlings, J. B., 2005. "Critical evaluation of extended kalman filtering and moving-horizon estimation." *Industrial and Engineering Chemistry Research,* **44**(8), pp. 2451–2460. 20

[57] Biegler, L., Yang, X., and Fischer, G., 2015. "Advances in sensitivity-based nonlinear model predictive control and dynamic real-time optimization." *Journal of Process Control,* **30**, pp. 104 – 116. 20, 39

[58] Zavala, V., and Biegler, L., 2009. "Nonlinear programming strategies for state estimation and model predictive control." In *Nonlinear Model Predictive Control*, L. Magni, D. Raimondo, and F. Allgöwer, eds., Vol. 384 of *Lecture Notes in Control and Information Sciences*. Springer Berlin Heidelberg, pp. 419–432. 20

[59] Sun, C., and Hahn, J., 2005. "Reduction of stable differential–algebraic equation systems via projections and system identification." *Journal of process control,* **15**(6), pp. 639–650. 20

[60] Hedengren, J., and Edgar, T., 2005. "Order reduction of large scale DAE models." *Computers and Chemical Engineering,* **29**(10), pp. 2069–2077. 20

[61] Hedengren, J., and Edgar, T., 2005. "Order reduction of large scale DAE models." In *IFAC 16th World Congress*. 20

[62] Pothen, A., and Fan, C.-J., 1990. "Computing the block triangular form of a sparse matrix." *ACM Transactions on Mathematical Software,* **16**(4), pp. 303–324. 22

[63] Petzold, L., Li, S., Cao, Y., and Serban, R., 2006. "Sensitivity analysis of differential-algebraic equations and partial differential equations." *Computers and Chemical Engineering,* **30**(10), pp. 1553–1559. 22

[64] Pantelides, C., 1988. "The consistent initialization of differential-algebraic systems." *SIAM Journal on Scientific and Statistical Computing,* **9**(2), pp. 213–231. 23

[65] Moore, P., Petzold, L., and Ren, Y., 1998. "Regularization of index-1 differential-algebraic equations with rank-deficient constraints." *SIAM Journal on Numerical Analysis,* **35**, pp. 43–61. 23

[66] Ascher, U. M., and Lin, P., 1996. "Sequential regularization methods for higher index DAEs with constraint singularities: The linear index-2 case." *SIAM Journal on Numerical Analysis,* **33**, pp. 1921–1940. 23

[67] Lin, P., and Spiteri, R. J., 2002. "A predicted sequential regularization method for index-2 hessenberg DAEs." *SIAM Journal on Numerical Analysis,* **39**, pp. 1889–1913. 23

[68] Bischof, C. H., Bcker, H. M., Hovland, P., Naumann, U., and Utke, J., 2008. *Advances in Automatic Differentiation*. Springer Science & Business Media, Berlin Heidelberg. 23

[69] Baumgarte, J., 1972. "Stabilization of constraints and integrals of motion in dynamical systems." *Computer Methods in Applied Mechanics,* **1**, pp. 1–16. 23

[70] Layton, R. A., 1998. *Principles of Analytical System Dynamics*. Springer. 24

[71] Wächter, A., and Biegler, L. T., 2006. "On the Implementation of a Primal-Dual Interior Point Filter Line Search Algorithm for Large-Scale Nonlinear Programming." *Mathematical Programming,* **106**(1), pp. 25–57. 26, 31, 75

[72] Bonilla, J., Diehl, M., Logist, F., Moor, B. D., and Impe, J. V., 2010. "An automatic initialization procedure in parameter estimation problems with parameter-affine dynamic models." *Computers and Chemical Engineering,* **34**(6), pp. 953–964. 28

[73] Kelly, J., and Hedengren, J., 2013. "A steady-state detection (SSD) algorithm to detect non-stationary drifts in processes." *Journal of Process Control,* **23**(3), March, pp. 326–331. 28

[74] Hedengren, J., and Edgar, T., 2008. "Approximate nonlinear model predictive control with in situ adaptive tabulation." *Computers and Chemical Engineering,* **32**, pp. 706–714. 28

[75] Gill, P. E., Murray, W., and Saunders, M. A., 2002. "SNOPT: An SQP algorithm for large-scale constrained optimization." *SIAM journal on optimization,* **12**(4), pp. 979–1006. 31

[76] Lucia, A., and McCallum, B. R., 2010. "Energy targeting and minimum energy distillation column sequences." *Computers and Chemical Engineering,* **34**(6), pp. 931 – 942. 38

[77] Li, P., Garcia, H. A., Wozny, G., and Reuter, E., 1998. "Optimization of a semibatch distillation process with model validation on the industrial site." *Industrial and Engineering Chemistry Research,* **37**(4), pp. 1341–1350. 38

[78] Ulas, S., Diwekar, U. M., and Stadtherr, M. A., 2005. "Uncertainties in parameter estimation and optimal control in batch distillation." *Computers and Chemical Engineering,* **29**(8), pp. 1805 – 1814. 38, 39

[79] Wang, K., Löhl, T., Stobbe, M., and Engell, S., 2000. "A genetic algorithm for online-scheduling of a multiproduct polymer batch plant." *Computers and Chemical Engineering,* **24**(2), pp. 393–400. 38

[80] Robinson, E., 1969. "The optimisation of batch distillation operations." *Chemical Engineering Science,* **24**(11), pp. 1661 – 1668. 38

[81] Mayur, D., May, R., and Jackson, R., 1970. "The time-optimal problem in binary batch distillation with a recycled waste-cut." *The Chemical Engineering Journal,* **1**(1), pp. 15 – 21 The Chemical Engineering Journal. 38

[82] Robinson, E., 1970. "The optimal control of an industrial batch distillation column." *Chemical Engineering Science,* **25**(6), pp. 921 – 928. 38

[83] Luyben, W. L., 1971. "Some practical aspects of optimal batch distillation design." *Industrial and Engineering Chemistry Process Design and Development,* **10**(1), pp. 54–59. 38

[84] Kim, Y.-S., 1985. "Optimal Control of Time-Dependent Processes (Design, Batch Distillation, Catalyst Deactivation)." PhD thesis, University of Massachusetts–Amherst. 38

[85] Diwekar, U., 1995. *Batch Distillation: Simulation, Optimal Design, and Control*. CRC Press. 38

[86] Safrit, B. T., and Westerberg, A. W., 1997. "Improved operational policies for batch extractive distillation columns." *Industrial and Engineering Chemistry Research,* **36**(2), pp. 436–443. 38

[87] Low, K. H., and Srensen, E., 2005. "Simultaneous optimal configuration, design and operation of batch distillation." *AIChE Journal,* **51**(6), pp. 1700–1713. 38

[88] Bonny, L., 2006. "Multicomponent batch distillations campaign: Control variables and optimal recycling policy." *Industrial and Engineering Chemistry Research,* **45**(26), pp. 8998–9009. 38

[89] Bonny, L., 2013. "Multicomponent batch distillations campaign: Control variables and optimal recycling policy. a further note." *Industrial and Engineering Chemistry Research,* **52**(5), pp. 2190–2193. 38

[90] Kim, J., and Ju, D., 2003. "Multicomponent batch distillation with distillate receiver." *Korean Journal of Chemical Engineering,* **20**(3), pp. 522–527. 38

[91] Jang, S.-S., 1993. "Dynamic optimization of multicomponent batch distillation processes using continuous and discontinuous collocation polynomial policies." *The Chemical Engineering Journal,* **51**(2), pp. 83 – 92. 38

[92] Varma, V. A., Reklaitis, G. V., Blau, G., and Pekny, J. F., 2007. "Enterprise-wide modeling & optimizationan overview of emerging research challenges and opportunities." *Computers and Chemical Engineering,* **31**(5), pp. 692–711. 38

[93] Loeblein, C., Perkins, J., Srinivasan, B., and Bonvin, D., 1997. "Performance analysis of on-line batch optimization systems." *Computers and Chemical Engineering,* **21**, pp. S867–S872. 38

[94] Shi, H., and You, F., 2015. "A novel adaptive surrogate modeling-based algorithm for simultaneous optimization of sequential batch process scheduling and dynamic operations." *AIChE Journal*. 38

[95] Dai, W., Word, D. P., and Hahn, J., 2014. "Modeling and dynamic optimization of fuel-grade ethanol fermentation using fed-batch process." *Control Engineering Practice,* **22**, pp. 231–241. 38

[96] Chu, Y., and You, F., 2013. "Integration of scheduling and dynamic optimization of batch processes under uncertainty: Two-stage stochastic programming approach and enhanced generalized benders decomposition algorithm." *Industrial and Engineering Chemistry Research,* **52**(47), pp. 16851–16869. 38

[97] Srinivasan, B., Palanki, S., and Bonvin, D., 2003. "Dynamic optimization of batch processes: I. characterization of the nominal solution." *Computers and Chemical Engineering,* **27**(1), pp. 1–26. 38

[98] Bhatia, T., and Biegler, L. T., 1996. "Dynamic optimization in the design and scheduling of multiproduct batch plants." *Industrial and Engineering Chemistry Research,* **35**(7), pp. 2234–2246. 38

[99] Terwiesch, P., Agarwal, M., and Rippin, D. W., 1994. "Batch unit optimization with imperfect modelling: a survey." *Journal of Process Control,* **4**(4), pp. 238–258. 38

[100] Kim, K., and Diwekar, U., 2001. "New era in batch distillation: Computer aided analysis, optimal design and control." *Reviews in Chemical Engineering,* **17**(2), pp. 111 – 164. 38

[101] Stichlmair, J., and Fair, J. R., 1998. *Distillation: principles and practices*. Wiley–VCH. 38

[102] Doherty, M. F., and Malone, M. F., 2001. *Conceptual design of distillation systems*. McGraw-Hill Science/Engineering/Math. 38

[103] Diwekar, U., Malik, R., and Madhavan, K., 1987. "Optimal reflux rate policy determination for multicomponent batch distillation columns." *Computers and Chemical Engineering,* **11**(6), pp. 629 – 637. 38, 39

[104] Barolo, M., and Guarise, G., 1996. "Batch distillation of multicomponent systems with constant relative volatilities." *Chemical Engineering Research and Design,* **74**(8), pp. 863 – 871. 39

[105] Kim, Y. H., 1999. "Optimal design and operation of a multi-product batch distillation column using dynamic model." *Chemical Engineering and Processing: Process Intensification,* **38**(1), pp. 61 – 72. 39

[106] Mujtaba, I., and Hussain, M., 1998. "Optimal operation of dynamic processes under process-model mismatches: Application to batch distillation." *Computers and Chemical Engineering,* **22, Supplement 1**, pp. S621 – S624 European Symposium on Computer Aided Process Engineering-8. 39

[107] Gruetzmann, S., and Fieg, G., 2008. "Startup operation of middle-vessel batch distillation column: modeling and simulation." *Industrial and Engineering Chemistry Research,* **47**(3), pp. 813–824. 39

[108] Hanke, M., and Li, P., 2000. "Simulated annealing for the optimization of batch distillation processes." *Computers and Chemical Engineering,* **24**(1), pp. 1 – 8. 39

[109] Diehl, M., Gerhard, J., Marquardt, W., and Mnnigmann, M., 2008. "Numerical solution approaches for robust nonlinear optimal control problems." *Computers and Chemical Engineering,* **32**(6), pp. 1279 – 1292. 39

[110] Prasad, V., and Bequette, B., 2003. "Nonlinear system identification and model reduction using artificial neural networks." *Computers and Chemical Engineering,* **27**(12), pp. 1741 – 1754. 39

[111] Li, P., Hoo, H. P., and Wozny, G., 1998. "Efficient simulation of batch distillation processes by using orthogonal collocation." *Chemical Engineering and Technology,* **21**(11), pp. 853–862. 39

[112] Jain, S., Kim, J.-K., and Smith, R., 2012. "Operational optimization of batch distillation systems." *Industrial and Engineering Chemistry Research,* **51**(16), pp. 5749–5761. 39

[113] Leipold, M., Gruetzmann, S., and Fieg, G., 2009. "An evolutionary approach for multi-objective dynamic optimization applied to middle vessel batch distillation." *Computers and Chemical Engineering,* **33**(4), pp. 857 – 870. 39

[114] Bonsfills, A., and Puigjaner, L., 2004. "Batch distillation: simulation and experimental validation." *Chemical Engineering and Processing: Process Intensification,* **43**(10), pp. 1239 – 1252. 39

[115] Barolo, M., and Botteon, F., 1998. "Calculation of parametric sensitivity in binary batch distillation." *Chemical Engineering Science,* **53**(10), pp. 1819 – 1834. 39

[116] Converse, A. O., and Gross, G. D., 1963. "Optimal distillate-rate policy in batch distillation." *Industrial and Engineering Chemistry Fundamentals,* **2**(3), pp. 217–221. 39

[117] Lopes, M. M., and Song, T. W., 2010. "Batch distillation: Better at constant or variable reflux?." *Chemical Engineering and Processing: Process Intensification,* **49**(12), pp. 1298 – 1304. 39

[118] Beck, J. V., and Arnold, K. J., 1977. *Parameter estimation in engineering and science*. John Wiley & Sons. 40, 41

[119] Wu, S., McLean, K. A., Harris, T. J., and McAuley, K. B., 2011. "Selection of optimal parameter set using estimability analysis and MSE-based model-selection criterion." *International Journal of Advanced Mechatronic Systems,* **3**(3), pp. 188–197. 40, 42

[120] Srinivasan, B., Bonvin, D., Visser, E., and Palanki, S., 2003. "Dynamic optimization of batch processes: II. role of measurements in handling uncertainty." *Computers and Chemical Engineering,* **27**(1), pp. 27–44. 40

[121] Seber, G., and Wild, C. *Nonlinear Regression*. John Wiley & Sons, Hoboken, New Jersey. 41

[122] Lewis, N. R., Hedengren, J. D., and Haseltine, E. L., 2015. "Hybrid dynamic optimization methods for systems biology with efficient sensitivities." *Processes,* **3**(3), pp. 701–729. 42

[123] Nagy, Z. K., and Braatz, R. D., 2003. "Worst-case and distributional robustness analysis of finite-time control trajectories for nonlinear distributed parameter systems." *Control Systems Technology, IEEE Transactions on,* **11**(5), pp. 694–704. 42

[124] Brown, P. N., Hindmarsh, A. C., and Petzold, L. R., 1994. "Using krylov methods in the solution of large-scale differential-algebraic systems." *SIAM Journal on Scientific Computing,* **15**(6), pp. 1467–1488. 42

[125] Cao, Y., Li, S., Petzold, L., and Serban, R., 2003. "Adjoint sensitivity analysis for differential-algebraic equations: The adjoint dae system and its numerical solution." *SIAM Journal on Scientific Computing,* **24**(3), pp. 1076–1089. 42

[126] Tolsma, J., and Barton, P. I., 2000. "DAEPACK: An open modeling environment for legacy models." *Industrial and Engineering Chemistry Research,* **39**(6), pp. 1826–1839. 42

[127] Chemcad version 6.5.0 Owned by Chemstations, Inc. in Houston, TX. Copyright 2015. 45

[128] Rowley, R. L., Wilding, W. V., Oscarson, J. L., Knotts, T. A., and Giles, N. F., 2013. "DIPPR data compilation of pure chemical properties." Design Institute for Physical Properties, AIChE. 47

[129] Seader, J. D., and Henley, E. J., 2006. *Separation Process Principles*. John Wiley & Sons. 47

[130] Hedengren, J. D., and Eaton, A. N., 2015. "Overview of estimation methods for industrial dynamic systems." *Optimization and Engineering*, pp. 1–24. 51

[131] International Energy Agency `http://www.iea.org`. 59

[132] Wang, Y., Ronilaya, F., Chen, X., and Roskilly, A. P., 2013. "Modelling and simulation of a distributed power generation system with energy storage to meet dynamic household electricity demand." *Applied Thermal Engineering,* **50**(1), pp. 523 – 535. 59

[133] International Energy Agency, CO_2 Emissions from Fuel Combustion, Edition 2014 `http://www.iea.org/statistics/onlinedataservice/`. 59

[134] Trends in global CO_2 emissions Tech. rep. `http://edgar.jrc.ec.europa.eu/news_docs/jrc-2014-trends-in-global-co2-emissions-2014-report-93171.pdf`,. 59, 61

[135] Overview of greenhouse gases `http://www.epa.gov/climatechange/ghgemissions/gases/co2.html`. 59

[136] Göransson, L., and Johnsson, F., 2009. "Dispatch modeling of a regional power generation system – Integrating wind power." *Renewable Energy,* **34**, pp. 1040 – 1049. 59

[137] Delarue, E. D., Luickx, P. J., and D'haeseleer, W. D., 2009. "The actual effect of wind power on overall electricity generation costs and CO_2 emissions." *Energy Conversion and Management,* **50**(6), pp. 1450 – 1456. 60

[138] Hu, E., Yang, Y., Nishimura, A., Yilmaz, F., and Kouzani, A., 2010. "Solar thermal aided power generation." *Applied Energy,* **87**(9), pp. 2881 – 2885. 60

[139] Manenti, F., and Ravaghi-Ardebili, Z., 2013. "Dynamic simulation of concentrating solar power plant and two-tanks direct thermal energy storage." *Energy,* **55**, pp. 89 – 97. 60

[140] Powell, K. M., Hedengren, J. D., and Edgar, T. F., 2013. "Dynamic optimization of a solar thermal energy storage system over a 24 hour period using weather forecasts." In *American Control Conference (ACC), 2013*, IEEE, pp. 2946–2951. 60, 75

[141] Powell, K. M., Hedengren, J. D., and Edgar, T. F., 2014. "Dynamic optimization of a hybrid solar thermal and fossil fuel system." *Solar Energy,* **108**(0), pp. 210 – 218. 60, 75

[142] Onar, O., Uzunoglu, M., and Alam, M., 2006. "Dynamic modeling, design and simulation of a wind/fuel cell/ultra-capacitor-based hybrid power generation system." *Journal of Power Sources,* **161**(1), pp. 707 – 722. 60

[143] Carbon pollution emission guidelines for existing stationary sources: Electric utility generating units http://www.gpo.gov/fdsys/pkg/FR-2015-10-23/pdf/2015-22842.pdf. 60

[144] A European Strategic Energy Technology Plan (SET-PLAN) Towards a Low Carbon Future, Document 52007DC0723 `http://eur-lex.europa.eu/legal-content/EN/TXT/PDF/?uri=CELEX:52007DC0723&rid=1`. 60

[145] Climate Summit 2014 `http://www.un.org/climatechange/summit/2014/09/2014-climate-change-summary-chairs-summary/`. 60

[146] Europian Union Legislation, Document 52007DC0019 `http://eur-lex.europa.eu/legal-content/EN/NOT/?uri=CELEX:52007SC0008`. 61

[147] Jensen, M., 2015. "Energy Processes Enabled by Cryogenic Carbon Capture." PhD thesis, Brigham Young University, February. 61, 64, 65, 73, 75, 92

[148] Baxter, L. L., 2011. Carbon dioxide capture from flue gas, Sept. 22 US Patent App. 12/745,193. 61, 65

[149] Baxter, L. L., 2013. Systems and methods for integrated energy storage and cryogenic carbon capture, May 2 WO Patent App. PCT/US2012/061,392. 61, 65

[150] Jensen, M. J., Russell, C. S., Bergeson, D., Hoeger, C. D., Frankman, D. J., Bence, C. S., and Baxter, L. L., 2015. "Prediction and validation of external cooling loop cryogenic carbon capture (CCC-ECL) for full-scale coal-fired power plant retrofit." *International Journal of Greenhouse Gas Control,* **42**, pp. 200 – 212. 61, 63

[151] Kang, C. A., Brandt, A. R., and Durlofsky, L. J., 2011. "Optimal operation of an integrated energy system including fossil fuel power generation, CO_2 capture and wind." *Energy,* **36**(12), pp. 6806 – 6820. 61, 70

[152] Belaissaoui, B., Cabot, G., Cabot, M.-S., Willson, D., and Favre, E., 2013. "CO_2 capture for gas turbines: an integrated energy-efficient process combining combustion in oxygen-enriched air, flue gas recirculation, and membrane separation." *Chemical Engineering Science,* **97**, pp. 256 – 263. 61

[153] Chalmers, H., Leach, M., and Gibbins, J., 2011. "Built-in flexibility at retrofitted power plants: What is it worth and can we afford to ignore it?." *Energy Procedia,* **4**, pp. 2596 – 2603. 62

[154] Cohen, S. M., Rochelle, G. T., and Webber, M. E., 2012. "Optimizing post-combustion CO_2 capture in response to volatile electricity prices." *International Journal of Greenhouse Gas Control,* **8**, May, pp. 180–195. 62

[155] Cohen, S. M., Rochelle, G. T., and Webber, M. E., 2011. "Optimal operation of flexible post-combustion CO_2 capture in response to volatile electricity prices." *Energy Procedia,* **4**, pp. 2604–2611. 62

[156] Cohen, S. M., Rochelle, G. T., and Webber, M. E., 2010. "Turning CO_2 capture on and off in response to electric grid demand: A baseline analysis of emissions and economics." *ASME Journal of Energy Resources Technology,* **132**, p. 021003. 62

[157] Ziaii, S., Cohen, S., Rochelle, G. T., Edgar, T. F., and Webber, M. E., 2009. "Dynamic operation of amine scrubbing in response to electricity demand and pricing." *Energy Procedia,* **1**(1), Feb., pp. 4047–4053. 62

[158] Chalmers, H., and Gibbins, J., 2007. "Initial evaluation of the impact of post-combustion capture of carbon dioxide on supercritical pulverised coal power plant part load performance." *Fuel,* **86**(14), pp. 2109 – 2123. 62

[159] Gerbelová, H., Versteeg, P., Ioakimidis, C. S., and Ferrão, P., 2013. "The effect of retrofitting Portuguese fossil fuel power plants with CCS." *Applied Energy,* **101**, pp. 280 – 287. 62

[160] Cormos, C.-C., 2012. "Integrated assessment of IGCC power generation technology with carbon capture and storage CCS." *Energy,* **42**(1), pp. 434 – 445. 62

[161] Cormos, C.-C., and Agachi, P. S., 2012. "Integrated assessment of carbon capture and storage technologies in coal-based power generation using CAPE tools." *Computer Aided Chemical Engineering,* **30**, pp. 56 – 60. 63

[162] Khorshidi, Z., Ho, M. T., and Wiley, D. E., 2015. "Techno-economic evaluation of using biomass-fired auxiliary units for supplying energy requirements of CO_2 capture in coal-fired power plants." *International Journal of Greenhouse Gas Control,* **32**(0), pp. 24 – 36. 63

[163] Mohan, A. R., Turaga, U., Subbaraman, V., Shembekar, V., Elsworth, D., and Pisupati, S. V., 2015. "Modeling the CO_2-based enhanced geothermal system (EGS) paired with integrated gasification combined cycle (IGCC) for symbiotic integration of carbon dioxide sequestration with geothermal heat utilization." *International Journal of Greenhouse Gas Control,* **32**(0), pp. 197 – 212. 63

[164] Sustainable Energy Solutions Company `http://sesinnovation.com/`. 63, 65, 92

[165] Impact of Load Following on Power Plant Cost and Performance: Literature Review and Industry Interviews, DOE/NETL-2013/1592. 64

[166] Cost and Performance Baseline for Fossil Energy Plants Volume 1: Bituminous Coal and Natural Gas to Electricity, National Energy Technology Laboratory/DOE/2010/1397. 67, 68, 97, 109

[167] Berkenpas, M., Rubin, E., and Zaremsky, C., 2007. "User manual: Integrated Environmental Control Model. Carnegie Mellon University, http://www.cmu.edu/epp/iecm/.". 70

[168] Ebrahimzadeh, E., Wilding, P., Frankman, D., Fazlollahi, F., and Baxter, L. L., 2016. "Theoretical and experimental analysis of dynamic plate heat exchanger: non-retrofit configuration." *Applied Thermal Energy,* **93**, pp. 1006 – 1019. 73

[169] Ebrahimzadeh, E., Wilding, P., Frankman, D., Fazlollahi, F., and Baxter, L. L., 2016. "Theoretical and experimental analysis of dynamic heat exchanger: Retrofit configuration." *Energy,* **96**, pp. 545 – 560. 73

[170] Safdarnejad, S. M., Hedengren, J. D., Baxter, L. L., and Kennington, L., 2015. "Investigating the impact of cryogenic carbon capture on the performance of power plants." In *Proceedings of the American Control Conference (ACC)*, pp. 5016–5021. 75

[171] Lindsay, J., and Dragoon, K., 2010. Summary Report on Coal Plant Dynamic Performance Capability Tech. rep., Renewable Northwest. 76

[172] Western Electricity Coordination Council Company `http://www.wecc.biz`. ix, 76, 77, 78

[173] National Renewable Energy Laboratory (NREL) `http://wind.nrel.gov/Web_nrel/`. 76, 118

[174] Federal Energy Regulatory Commission `http://www.ferc.gov/`. 76

[175] Natural Gas Forecasted Prices `http://knoema.com/ncszerf/natural-gas-prices-long-term-forecast-to-2020-data-and-charts`. 83

[176] EIA annual reports for natural gas `http://www.eia.gov/naturalgas/annual/`. 83

[177] California Independent System Operator (CAISO), CAISO Demand Forecast, Wind and Solar Forecast `http://oasis.caiso.com`. ix, 94, 95, 96

[178] LCG consulting website `http://www.energyonline.com/Data/GenericData.aspx?DataId=20&CAISO___Average_Price`. ix, 94, 95

[179] Utamura, M., Hoizumi, S., Takeda, Y., Sasaki, T., Komatsu, H., Kirikami, and et al., 2001. Gas turbine exhaust recirculation method and apparatus, Mar. 20 US Patent 6,202,400. 95

[180] Liu, F., Smallwood, G. J., and Guo, H., 2003. "The chemical effect of CO_2 replacement of N_2 in air on the burning velocity of CH_4 and H_2 premixed flames." *Combustion and Flame,* **133**, pp. 495–497. 95

[181] Hustad, J. E., and Røkke, P. E., 2005. "Exhaust Gas Recirculation in Gas Turbines for Reduction of CO_2 Emissions; Combustion Testing with Focus on Stability and Emissions." *International Journal of Thermodynamics,* **8**, pp. 167–173. 95

[182] U.S. Energy Information Administration (EIA) Coal News `http://www.eia.gov/coal/news_markets/`. 97

[183] U.S. Energy Information Administration Natural Gas Monthly Report `http://www.eia.gov/naturalgas/monthly/pdf/table_03.pdf`. 97

[184] Manson, S. S., 1954. Behavior of materials under conditions of thermal stress Tech. rep. 117

[185] Coffin, J. L. F., and Wesley, R., 1954. A study of the effects of cyclic thermal stresses on a ductile metal Tech. rep. 117

[186] Cohen, A. I., 1990. "Modeling unit ramp limitations in unit commitment." In *Proceedings of the 10th Power systems and Computing Conference*, pp. 1107–1114. 118

[187] Wang, C., and Shahidehpour, S., 1993. "Effects of ramp-rate limits on unit commitment and economic dispatch." *IEEE Transactions on Power Systems,* **8**(3), pp. 1341–1350. 118

[188] Kumar, N., Besuner, P., Lefton, S., Agan, D., and Hilleman, D. Power Plant Cycling Costs Tech. rep., National Renewable Energy Laboratory. 118

[189] Matsuishi, M., and Endo, T. Fatigue of metals subjected to varying stress Presented to the Japan Society of Mechanical Engineers Fukuoka, Japan, 1968. 118

[190] Mukhopadhyay, N., Dutta, B., and Kushwaha, H., 2001. "On-line fatigue-creep monitoring system for high-temperature components of power plants." *International Journal of Fatigue,* **23**(6), pp. 549 – 560. 119

[191] J-Rain Free Rainflow Counting Software `http://www.jesmondengineering.com/engineering-software/j-rain-free-rainflow-counting-software/`. 119

[192] Fazlollahi, F., Bown, A., Ebrahimzadeh, E., and Baxter, L. L., 2015. "Design and analysis of the natural gas liquefaction optimization process- (CCC-ES) (energy storage of cryogenic carbon capture)." *Energy,* **90, Part 1**, pp. 244 – 257. 127

[193] Fazlollahi, F., Bown, A., Ebrahimzadeh, E., and Baxter, L. L., 2015. "Transient natural gas liquefaction and its application to energy storage with cryogenic carbon capture (CCC-ES)." *Energy*, p. under review. 127

[194] Fazlollahi, F., Bown, A., Ebrahimzadeh, E., and Baxter, L. L., 2015. "Transient natural gas liquefaction process comparison- dynamic heat exchanger under transient changes in flow." *Energy*, p. under review. 127

[195] The economic impact of LNG exports from the United States, Deloitte Center for Energy Solutions Tech. rep. ix, 127, 128

APPENDIX A. RIGOROUS MODEL FOR THE BATCH DISTILLATION COLUMN

Listing A.1: Binary Distillation Column Model in APMonitor Modeling Language

```
% Binary Batch Distillation Column
% Component 1 = methanol
% Component 2 = ethanol
Constants
  n = 40 % stages
  x0 = 0.59 % initial composition
  % Constants for heat of vaporization
  A_m = 3.2615e7
  B_m = -1.0407
  C_m = 1.8695
  D_m = -0.60801
  A_e = 6.5831e7
  B_e = 1.1905
  C_e = -1.7666
  D_e = 1.0012
  % Critical temperatures (K)
  Tc_m = 512.5
  Tc_e = 514
  % Density coefficients
  rho_m_1 = 2.3267
  rho_m_2 = 0.27073
  rho_m_3 = 512.05
  rho_m_4 = 0.24713
  rho_e_1 = 1.6288
  rho_e_2 = 0.27469
  rho_e_3 = 514
  rho_e_4 = 0.23178
  % Heat capacity coefficients
  cp_m_liq_1 = 2.5604E5
  cp_m_liq_2 = -2.7414E3
  cp_m_liq_3 = 1.4777E1
  cp_m_liq_4 = -3.5078E-2
  cp_m_liq_5 = 3.2719E-5
  cp_e_liq_1 = 1.0264E5
  cp_e_liq_2 = -1.3963E2
  cp_e_liq_3 = -3.0341E-2
  cp_e_liq_4 = 2.0386E-3
  cp_e_liq_5 = 0
  % Standard heats of formation (J/kmol)
  h_form_std_m = -2.391E8
  h_form_std_e = -2.7698E8
  % Vapor pressure coefficients
  vpm[1] = 82.718
  vpm[2] = -6904.5
  vpm[3] = -8.8622
```

```
  vpm[4] = 7.4664E-06
  vpm[5] = 2
  vpe[1] = 73.304
  vpe[2] = -7122.3
  vpe[3] = -7.1424
  vpe[4] = 2.8853E-06
  vpe[5] = 2
End Constants

Parameters
  rr = 3.5 % reflux ratio
  hf = 0.8 % fractional heat loss fraction
  vf = 0.45 % tray efficiency
  tray_hol = 0.07 % tray holdup
  condenser_hol = 0.144 % condenser holdup
  heat_rate = 36000 , > 0 % 36000 J/min = 600 W
  gamma = 1.0  % activity coefficient

Variables
  x[1:n] = x0 , >= 0 , <= 1
  y[2:n] = x0 , >= 0 , <= 1
  L[1:n-1] = 0.36 , > 0  % mol/min
  V[2:n] = 0.72 , > 0  % mol/min
  D = 0.36 , > 0  % mol/min
  boil_hol = 28 , >0 % mol
  Q_cond = 0
  np = 0 , >= 0 % mol
  xp = 0.99 , >= 0 , <= 1
  T[1:n] = 320 % tray temperature
  ystar[2:n] = x0 % theoretical vapor composition

Intermediates
  % tray pressures
  P[1] = 101325 * 0.86  % local atmospheric pressure
  P[2:n] = P[1:n-1] + 101325/760  % pressure drop
  % pure component and mixture vapor pressure (Pa)
  vp1[1:n] = exp(vpm[1]+vpm[2]/T[1:n]+vpm[3]*LOG(T[1:n])+vpm[4]*(T[1:n]^vpm[5]))
  vp2[1:n] = exp(vpe[1]+vpe[2]/T[1:n]+vpe[3]*LOG(T[1:n])+vpe[4]*(T[1:n]^vpe[5]))
  vp[1:n] = x[1:n] * vp1[1:n] + (1-x[1:n]) * vp2[1:n]
  % pure component and mixutre density (kmol/m3 or mol/L)
  rho_meth[1:n-1] = rho_m_1 / (rho_m_2^(1+(1-T[1:n-1]/rho_m_3)^rho_m_4))
  rho_etha[1:n-1] = rho_e_1 / (rho_e_2^(1+(1-T[1:n-1]/rho_e_3)^rho_e_4))
  rho_mix[1:n-1]  =  rho_meth[1:n-1] * x[1:n-1] + rho_etha[1:n-1] * (1-x[1:n-1])
  % pure component heat of vaporization (J/mol)
  Hvap_m[1:n] = A_m*(1-T[1:n]/Tc_m)^(B_m+C_m*(T[1:n]/Tc_m)+D_m*(T[1:n]/Tc_m)^2)/1000
  Hvap_e[1:n] = A_e*(1-T[1:n]/Tc_e)^(B_e+C_e*(T[1:n]/Tc_e)+D_e*(T[1:n]/Tc_e)^2)/1000
  % pure component liquid enthalpies (J/mol)
  h_liq_m[1:n] = (cp_m_liq_1 * (T[1:n])     + cp_m_liq_2 * (T[1:n])^2/2 + &
                  cp_m_liq_3 * (T[1:n])^3/3 + cp_m_liq_4 * (T[1:n])^4/4 + &
                  cp_m_liq_5 * (T[1:n])^5/5)/1000
  h_liq_e[1:n] = (cp_e_liq_1 * (T[1:n])     + cp_e_liq_2 * (T[1:n])^2/2 + &
                  cp_e_liq_3 * (T[1:n])^3/3 + cp_e_liq_4 * (T[1:n])^4/4 + &
                  cp_e_liq_5 * (T[1:n])^5/5)/1000
  % pure component vapor enthalpies (J/mol)
  h_gas_m[2:n] = h_liq_m[2:n] + Hvap_m[2:n]
  h_gas_e[1:n] = h_liq_e[1:n] + Hvap_e[1:n]
  % tray vapor and liquid enthalpies (J/mol)
  h_gas[2:n] = y[2:n] * h_gas_m[2:n] + (1-y[2:n])*h_gas_e[2:n]
  h_liq[1:n] = x[1:n] * h_liq_m[1:n] + (1-x[1:n])*h_liq_e[1:n]

Equations
```

```
% tray bubble point temperature
P[1:n] = vp[1:n]
% vapor liquid equilibrium
ystar[2:n] * P[2:n] = gamma * x[2:n] * vp1[2:n]
% non-ideal separation with tray efficiency
y[n] = ystar[n]
y[2:n-1] = y[3:n]-vf*(y[3:n]-ystar[2:n-1])
% reflux ratio = L/D
L[1] = rr * D
% Condenser mole balance (methanol)
condenser_hol * x[1] = - (L[1]+D) * x[1] + V[2] * y[2]
% Tray mole balance (methanol)
tray_hol * $x[2:n-1] = L[1:n-2] * x[1:n-2] - (L[2:n-1]) * x[2:n-1] &
            - V[2:n-1] * y[2:n-1] + y[3:n] * V[3:n]
% Reboiler mole balance (methanol)
boil_hol * $x[n] + $boil_hol * x[n] = L[n-1] * x[n-1] - V[n] * y[n]
% Overall condenser mole balance
V[2] = D * (rr+1)
% Overall tray mole balance
0 = V[3:n] + L[1:n-2] - V[2:n-1] - L[2:n-1]
% Energy balance (no dynamics)
0 = (V[2]* (h_gas[2] - h_liq[1]) - Q_cond)
0 =  V[3:n]   * (h_gas[3:n]   - h_liq[2:n-1]) - V[2:n-1] * (h_gas[2:n-1] - h_liq[2:n-1]) &
   - L[1:n-2] * (h_liq[1:n-2] - h_liq[2:n-1])
0 = heat_rate * hf - V[n]   * (h_gas[n]-h_liq[n]) - L[n-1] * (h_liq[n-1]-h_liq[n])
% Production rate equations
$boil_hol = -D
$np = D
xp * $np + np * $xp = x[1] * D
```

Listing A.2: Python Dynamic Estimation

```
from apm import *
s = 'http://byu.apmonitor.com'
a = 'distill_l1_norm'
apm(s,a,'clear all')
apm_load(s,a,'distill.apm')
csv_load(s,a,'data.csv')
apm_option(s,a,'nlc.imode',5)
apm_option(s,a,'nlc.max_iter',100)
apm_option(s,a,'nlc.nodes',2)
apm_option(s,a,'nlc.time_shift',0)
apm_option(s,a,'nlc.ev_type',1)
apm_info(s,a,'FV','hf')
apm_info(s,a,'FV','vf')
apm_info(s,a,'FV','tray_hol')
apm_info(s,a,'FV','condenser_hol')
apm_info(s,a,'CV','x[1]')
apm_info(s,a,'CV','np')
output = apm(s,a,'solve')
print(output)
apm_option(s,a,'hf.status',1)
apm_option(s,a,'vf.status',1)
apm_option(s,a,'tray_hol.status',1)
apm_option(s,a,'condenser_hol.status',1)
apm_option(s,a,'x[1].fstatus',1)
apm_option(s,a,'np.fstatus',1)
apm_option(s,a,'x[1].wsphi',10000)
```

```
apm_option(s,a,'x[1].wsplo',10000)
apm_option(s,a,'np.wsphi',10)
apm_option(s,a,'np.wsplo',10)
apm_option(s,a,'x[1].meas_gap',1e-4)
apm_option(s,a,'np.meas_gap',0.01)
apm_option(s,a,'hf.lower',0.001);
apm_option(s,a,'hf.upper',1.0);
apm_option(s,a,'vf.lower',0.001);
apm_option(s,a,'vf.upper',0.6);
apm_option(s,a,'tray_hol.lower',0.01);
apm_option(s,a,'tray_hol.upper',0.1);
apm_option(s,a,'condenser_hol.lower',0.1)
apm_option(s,a,'condenser_hol.upper',0.5)
output = apm(s,a,'solve')
print(output)
y = apm_sol(s,a)
print('hf: ' + str(y['hf'][-1]))
print('vf: ' + str(y['vf'][-1]))
print('tray_hol: ' + str(y['tray_hol'][-1]))
print('cond_hol: ' + str(y['condenser_hol'][-1]))
print('np: ' + str(y['np'][-1]))
print('xp: ' + str(y['xp'][-1]))

import matplotlib.pyplot as plt
import pandas as pd
data_file = pd.read_csv('data_for_plotting.csv')

plt.figure(1)
plt.subplot(3,1,1)
plt.plot(y['time'],y['np'],'bx-',linewidth=2.0)
plt.plot(data_file['time'],data_file['np'],'ro')
plt.legend(['Predicted','Measured'])
plt.ylabel('Moles')

ax = plt.subplot(3,1,2)
plt.plot(y['time'],y['x[1]'],'bx-',linewidth=2.0)
plt.plot(data_file['time'],data_file['x[1]'],'ro')
plt.plot(y['time'],y['xp'],'k:',linewidth=2.0)
plt.legend(['Predicted','Measured','Cumulative'])
plt.ylabel('Composition')
ax.set_ylim([0.6, 1.05])

plt.subplot(3,1,3)
plt.plot(y['time'],y['x[1]'],'bx-',linewidth=2.0)
plt.plot(y['time'],y['x[2]'],'k:',linewidth=2.0)
plt.plot(y['time'],y['x[5]'],'r--',linewidth=2.0)
plt.plot(y['time'],y['x[10]'],'m.-',linewidth=2.0)
plt.plot(y['time'],y['x[20]'],'y-',linewidth=2.0)
plt.plot(y['time'],y['x[30]'],'g-.',linewidth=2.0)
plt.plot(y['time'],y['x[40]'],'k-',linewidth=2.0)
plt.legend(['x1','x2','x5','x10','x20','x30','x40'])
plt.ylabel('Composition')

plt.savefig('results_l1.png')
plt.show()
```